Journal of Nanomaterials

Polymer Matrix Nanocomposites and Nanostructured Materials

Guest Editors: Luiz Antonio Ferreira Coelho, Sergio Henrique Pezzin, Marcio Rodrigo Loos, Luis Antonio Sanchez de Almeida Prado, and Alejandro Manzano Ramirez

Polymer Matrix Nanocomposites and Nanostructured Materials

Journal of Nanomaterials

Polymer Matrix Nanocomposites and Nanostructured Materials

Guest Editors: Luiz Antonio Ferreira Coelho, Sergio Henrique Pezzin, Marcio Rodrigo Loos, Luis Antonio Sanchez de Almeida Prado, and Alejandro Manzano Ramirez

Editorial Board

Contents

Hindawi Publishing Corporation
Journal of Nanomaterials
Volume 2012, Article ID 962815, 2 pages
doi:10.1155/2012/962815

Editorial

Polymer Matrix Nanocomposites and Nanostructured Materials

Luiz Antonio Ferreira Coelho,[1] Sergio Henrique Pezzin,[1] Marcio Rodrigo Loos,[2] Luis Antonio Sanchez de Almeida Prado,[3] and Alejandro Manzano Ramirez[4]

[1] *Center for Technological Sciences, State University of Santa Catarina, 89223-100 Joinville, SC, Brazil*
[2] *Department of Macromolecular Science and Engineering, Case Western Reserve University, Cleveland, OH 7202, USA*
[3] *Institut für Kunststoffe und Verbundwerkstoffe, Technical University of Hamburg-Harburg, 21073 Hamburg, Germany*
[4] *CINVESTAV-Querétaro (Materials Science & Technology), Libramiento Norponiente 2000, 76230 Santiago de Querétaro, QRO, Mexico*

Correspondence should be addressed to Luiz Antonio Ferreira Coelho, lcoelho@joinville.udesc.br

Received 3 June 2012; Accepted 3 June 2012

By the end of the 80s, researchers at Toyota Motor Corporation started to study the exfoliation of clay in polymeric matrices via in situ polymerization. They reinforced a polymeric matrix with small amounts of nanosized clays. In the beginning of the 90s with the Iijima's report on carbon nanotubes, an era of global nanomaterials research emerged. Initially the research focus was on the mechanical properties of the new polymer nanocomposites, but afterwards research started to be focused on the multifunctional properties of these materials. In this special issue on, the reader will find 11 selected papers briefly summarized below.

Polyaniline (Pani) and polypyrrole (Ppy) half hollow spheres with different shell thicknesses were synthesized using polystyrene (PS) as the core by Yun et al. The PS core was synthesized by emulsion polymerization. The shell thickness of the Pani and Ppy half hollow spheres can be controlled in the range of 16 to 53 nm.

B. Akbari and R. Bagheri studied polypropylene/montmorillonite systems prepared by melt intercalation method. The effects of compatibilizer, extruder rotor speed, and feeding rate on the properties of the nanocomposites were investigated. The results illustrate that introduction of the compatibilizer and also variations of the processing conditions affect structure and mechanical properties of the nanocomposites.

V. Pistor et al. investigated the influence of polyhedral oligomeric silsesquioxanes (POSS) nanodomains in the crystallization behavior of thermoplastic polyurethanes (TPU), and found that trisilanol isobutyl-POSS reduces crystallite sizes. Moreover, samples with higher concentrations of POSS presented two crystallization stages, forming two distinct types of crystalline structures (disks at first and then moving to spherulites). This class of polymer materials has wide potential applications, including the medical, automotive, and industrial sectors.

POSS was also used as "building blocks" for star-shaped poly(N-isopropylacrylamide) organic-inorganic hybrids, as reported by S-W. Kuo et al. These hybrids exhibited also interesting features such as photoluminescence (not observed for neat poly(N-isopropylacrylamide) homopolymers). Apart from the interesting functional properties, the authors describe a new "variation" of atom-transfer radical polymerization process based on click-chemistry (organic azide-alkyne cyclo-addition reaction), never reported before for such systems.

Sticking into materials for optical applications, researchers reported the preparation of zinc oxide (ZnO) nanocomposites based on poly [2-methoxy-5(2′-ethyl hexyloxy)-phenylene vinylene] (MEH-PPV) using the well-established spin-coating technique. In spite of the presence of ZnO agglomerates, the electron delocalization was not affected. The photoluminescence behavior was higher as the amount of ZnO in the nanocomposites increased.

Looking for antibacterial activity and interesting mechanical properties, composites of polyvinyl alcohol (PVA) reinforced with silver nanoparticles (AgnP) have been investigated by impedance spectroscopy. Combination of dielectric and dynamical-mechanical analyses gave a better

understanding of the molecular dynamics of these materials, showing that a secondary relaxation was erroneously assigned as the glass transition of PVA and composites in former studies. Nevertheless, it has been showed that the inclusion of AgnP decreases the interfacial barrier and increases the transition probability of electron hopping across the barrier and insulator chains, providing a percolation path through the amorphous regions of the polymer matrix and thus an enhanced conductivity.

Composites have been prepared using long multiwalled carbon nanotubes (LMWCNTs, length of 2 mm) and short multiwalled carbon nanotubes (SMWCNTs, length of 1 μm) by M. Zimmer et al. The use of LMWCNTs improved the electrical and mechanical properties of the composites when compared to SMWCNTs. Although the longer networks were expected to allow for more undisturbed phonon transportation, the thermal conductivity of the composites was not affected by the addition of long CNTs. These intriguing results were related to the functioning of the networks made by both the LMWCNTs and shorter MWCNTs.

The application of polystyrene/ZnO nanocomposites as scattering films in lighting application has been studied by G. Nenna et al. The device efficiency was found to increase with thickness and concentration of ZnO nanoparticles. The resulting materials showed properties suitable for OLED lighting applications.

The paper by P. Huh and S-C. Kim presented the preparation of nanostructured composites. The work describes the formation of unique ZnO nanoarrays utilizing a photodynamic polymer and surface relief grating structures, demonstrating that the electrostatic layer-by-layer assembly is a simple and economical methodology.

L. Nana et al. reported how polystyrene (PS) microspheres can be first synthesized by emulsion polymerization and then used to prepare Titanium dioxide (TiO_2)/PS composite microspheres by the modified sol-gel method. It was also showed that Ni/TiO_2/PS composite microspheres can be synthesized by the reduction and adsorption process.

Finally, the preparation of silver nanostructures from bicontinuous microemulsions was described by M. A. Pedroza-Toscano et al.

As Guest Editors for this special issue, we are pleased with diverse and intense research activities in this area. We expect the special issue will be well received by the reader as a small sample of the current research on polymer matrix nanocomposites and nanostructured materials.

Acknowledgments

The guest editors would like to acknowledge and thank authors, reviewers, and staff members of Hindawi Publishing Corporation for their contributions and support to this special issue.

Luiz Antonio Ferreira Coelho
Sergio Henrique Pezzin
Marcio Rodrigo Loos
Luis Antonio Sanchez de Almeida Prado
Alejandro Manzano Ramirez

Hindawi Publishing Corporation
Journal of Nanomaterials
Volume 2012, Article ID 925750, 11 pages
doi:10.1155/2012/925750

Research Article

Molecular Dynamics Analysis of PVA-*AgnP* Composites by Dielectric Spectroscopy

J. Betzabe González-Campos,[1] Evgen Prokhorov,[2] Isaac C. Sanchez,[3] J. Gabriel Luna-Bárcenas,[2] Alejandro Manzano-Ramírez,[2] Jesús González-Hernández,[4] Yliana López-Castro,[1] and Rosa E. del Río[1]

[1] *Department of Chemistry, Institute of Chemical and Biological Researches, Universidad Michoacana de San Nicolás de Hidalgo, Ciudad Universitaria, 58060 Morelia, MICH, Mexico*
[2] *Biomaterials Laboratory, Centro de Investigación y de Estudios avanzados del IPN, Unidad Querétaro, 76230 Querétaro, QRO, Mexico*
[3] *Department of Chemical Engineering, The University of Texas at Austin, Austin, TX 78712, USA*
[4] *Nanostructurated Materials Laboratory, Centro de Investigación en Materiales Avanzados, S.C., 31109 Chihuahua, CHIH, Mexico*

Correspondence should be addressed to J. Gabriel Luna-Bárcenas, gluna@qro.cinvestav.mx

Received 10 February 2012; Revised 20 May 2012; Accepted 20 May 2012

Academic Editor: Sérgio Henrique Pezzin

The molecular dynamics of PVA/AgnP composites were studied by dielectric spectroscopy (DS) in the 20–300°C temperature range. Improper water elimination leads to misinterpretation of thermal relaxations in PVA composites in agreement with the previous report for pristine PVA. The evaporation of water and its plasticizing effect are more evident in pure PVA confirming the existence of strong interaction between OH groups of PVA chains and AgnP. Dry films show a single nonlinear VFT dependence (from 45°C until melting) associated to the α-relaxation and, therefore, to the glass transition phenomenon and from dielectric measurements, the T_g of composites vary from 88°C for pristine PVA to 125°C for PVA/AgnP (5 wt%). Below 45°C, dry films exhibit a single Arrhenius behavior showing a 3D hopping conductivity as explained based on the variable range hopping model. PVA/AgnP composites have higher conductivity compared to pristine PVA, and it increases as AgnP weight percent increases. Finally, DMA measurements support the statement that a secondary relaxation was erroneously assigned as the glass transition of PVA and composites in previous reports.

1. Introduction

Nowadays metal-polymer nanocomposites are the subject of increased interest because they combine the features of polymers with those of metals. Metallic nanoparticles incorporated in or with polymers have attracted much attention due to their distinct optical, electrical, and catalytic properties, which have potential applications in different fields such as bioengineering, photonics, and electronics [1–5]. Among different metals used for nanoparticles preparation, silver is very attractive because it exhibits the highest electrical and thermal conductivities, together with their antibacterial activity and even their interaction with HIV-1 virus [6]. On the other hand, polyvinyl alcohol (PVA) has been widely used as a matrix for preparation of nanocomposites due to its easy processability and high optical clarity. It is considered among the best polymers as host matrix for silver nanoparticles (AgnP), and it is frequently used as a stabilizer due to its optical clarity, which enables investigation of the nanoparticle formation [7, 8]. PVA is a biologically friendly polymer since it is water soluble and has extremely low cytotoxicity, which allows the application of PVA-based composites in the biomedical field.

PVA/AgnP is a very attractive combination since these composites have high mechanical strength, water-solubility, good environmental stability, easy processability, and electrical conductivity [9–11]. Different studies have been carried out about the optimal parameters for the synthesis of nanoparticles, the antibacterial activity of composites, their mechanical properties, and the chemical interaction between

PVA and AgnP [12–15]. However, the molecular dynamics analysis by dielectric relaxation studies and the electrical conductivity behavior of PVA-Ag nanocomposite films have been scarcely studied; there is only one report in this regard [16].

One parameter that can be characterized by means of the molecular dynamics analysis is the glass transition temperature (T_g). In polymers, polymers blends, and composites, an accurate characterization of the T_g plays a crucial role, since it indicates the change from the glassy state into a liquid or a rubbery state, and it can be a measure of compatibility or miscibility in polymer blends [17]. Additionally, physicochemical properties of a material such as dissolution, bioavailability, processing, and handling qualities can be related to the glass transition temperature of the material [18]. Also the optimal application and processing temperatures for polymers base materials are dependent on their glass transition temperature.

On the other hand, in a previous work [19], it was shown by dielectric and dynamic mechanical analysis that the nature of pure PVA thermal relaxations was erroneously assigned, since improper water elimination and the narrow temperature range analyzed in all the previous reports have led to misinterpretation of thermal relaxations in pure PVA. Commonly, the molecular dynamics analysis of PVA composites, and its blends with other polymers and inorganic compounds has been carried out in a narrow temperature range and based on pure PVA thermal relaxations behavior; however, if the molecular dynamics of pure PVA has been misunderstood, it could also be the case of the molecular dynamics of its composites and blends.

Based on these arguments, the aim of this work is twofold: to study the molecular dynamics of PVA/AgnP composites, which have been scarcely reported, and to make a comparison based on the previous studies on pure PVA to probe that previous reports on PVA-inorganic materials composites have also been misunderstanding because they were based in pure PVA results.

2. Experimental Methods

2.1. Films Preparation. Poly(vinyl alcohol), Mw 89,000–98,000 g/mol and hydrolysis degree >99%, was purchased from Sigma-Aldrich and used as received. Carbon-coated silver nanoparticles powder 25 nm average particle size was purchased from nanotechnologies, Inc. PVA films were obtained by dissolving a known amount of PVA in water to obtain a 7.8 wt % solution under stirring at 90°C. The proper quantity of silver nanoparticles powder (0.5, 1, 2, 3 and 5% w/w respect to PVA dry based) was poured into the 7.8 wt % aqueous PVA solution, this solution was mechanically stirrer for 40 min and further sonicated during 30 min to obtain a homogeneous nanoparticle solution. Afterward PVA/AgnP films were prepared by the solvent casting method, by pouring the solutions into plastic Petri dishes and allowing the solvent to evaporate at 37°C during 24 hours. These films had thicknesses of ca. 40 μm measured by a Mitutoyo micrometer. A thin layer of gold was vacuum-deposited onto both film sides to serve as electrodes. Rectangular small pieces (about 4 mm × 3 mm) of these films were prepared for measurements, and the contact areas were measured with a digital calibrator (Mitutoyo).

2.2. Infrared Measurements and Morphology Analysis. Chemical analysis of PVA/AgnP composites was performed by FTIR on a Perkin-Elmer spectrophotometer using an ATR accessory in the range 4000–650 cm^{-1}. Resolution was set to 4 cm^{-1}, and the spectra are an average of 32 scans. PVA/AgnP films morphology was analyzed by JEOM JSM-7401F field emission scanning electron microscope.

2.3. Thermal Measurements. Moisture content was determined by thermogravimetric analysis (TGA). The moisture content was evaluated by the decrease of sample weight during the heating scan. TGA curves were obtained using a Mettler Toledo apparatus, model TGA/SDTA 851e, with a sample mass of ca. 3 mg and an aluminum sample holder under argon atmosphere with a flow rate of 75 mL/min. Heating rate was set to 10°C/min.

2.4. Dielectric Measurements. The dielectric measurements in the frequency range from 0.1 Hz to 1 MHz were carried out using a Solartron 1260 impedance gain-phase analyzer with 1294 Impedance interface and in the frequency range 100 Hz–110 MHz using an Agilent Precision Impedance Analyzer 4294A. The amplitude of the measuring signal was 100 mV. The home-made impedance vacuum cell was used in conjunction with a Watlow's Series 982 microprocessor with ramping temperature controller for all dielectric measurements from 20°C to 300°C, and for some samples with an additional thermal treatment at 120°C to obtain "dry" samples. Each sample was left at each temperature for 3 min to ensure thermal equilibrium.

2.5. Dynamic Mechanical Analysis (DMA). DMA measurements were carried out using an RSAIII, TA Instruments with a heating rate of 5°C/min at a frequency of 0.1 Hz, under dry air atmosphere in the 25–300°C temperature range.

3. Results and Discussion

3.1. Morphological Analysis. The AgnP dispersion on PVA matrix analyzed by SEM is shown in Figure 1. At lower concentration, a homogeneous dispersion of AgnP is observed since they are well distributed within the PVA matrix with particles size of 25 nm. When AgnP concentration increases, the formation of agglomerates cannot be avoided; however, the dispersion of silver nanoparticles is adequate and clusters are not significant. Uniform metal nanoparticles dispersion is required to guarantee the homogeneity on properties. The used methodology gives well dispersed films even at high concentration such as 5% wt.

It could be seen that PVA is an excellent host matrix for encapsulation of silver nanoparticles acting as a good capping agent and providing environmental and chemical stability.

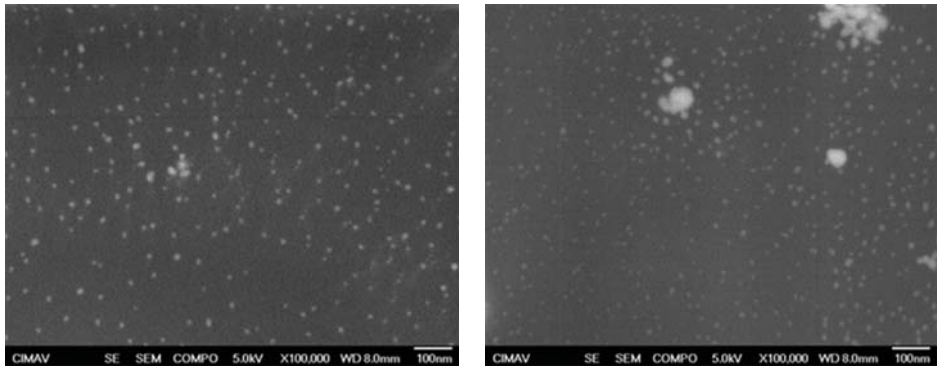

(a) (b)

Figure 1: (a) PVA/AgnP (2%) and (b) PVA/AgnP (5%) films.

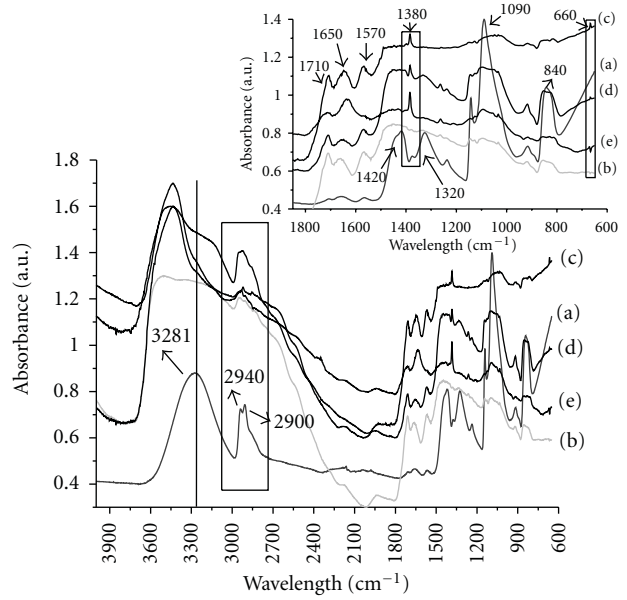

(a) Pristine PVA (gray)
(b) PVAAgnPs 0.5% w/w (LTgray)
(c) PVAAgnPs 1% w/w
(d) PVAAgnPs 3% w/w
(e) PVAAgnPs 5% w/w

Figure 2: IR spectra of pristine PVA and PVA/AgnP composites. Window insert: zoom for the 1800 cm^{-1} to 600 cm^{-1} region.

3.2. FTIR-ATR Analysis. The FTIR spectra for pristine PVA and PV/AgnP composites are shown in Figure 2. The spectrum of pristine PVA shows its characteristic bands at 1040 cm^{-1} (C–O) in acetyl group, 1090 cm^{-1} (C–O), 1140 cm^{-1} (C–O, crystallinity), 1170 cm^{-1} (C–O–C) in ether group, 1245 cm^{-1} (C–O–C) in acetyl group, 1320 cm^{-1} (CH + OH interaction), the 1375 cm^{-1} band due to the coupling of O–H vibrations at 1420 cm^{-1} with the wagging vibrations (CH_2), 1650 cm^{-1} (C=C), 1730 cm^{-1} (C=O), 2850 cm^{-1} (CH), 2900–2950 cm^{-1} (CH_2), and 3000–3500 cm^{-1} (O–H).

Figure 2 also shows clear evidence of chemical interactions bonding between PVA and silver nanoparticles suggesting that these interactions are mainly between –OH groups of PVA and AgnP. This is observed by a general change in the intensity of the absorption bands in the stretching vibrations of OH groups involved in hydrogen bonding (3800–3000 cm^{-1}) and their shifting to 3400 cm^{-1}. The PVA-AgnP's spectrums show a new band at 660 cm^{-1} corroborating the formation of hydrogen bonds in all structures. A change in the intensity of the band at 1380 cm^{-1}, compared with the band at 1420 cm^{-1}, indicates the decoupling between OH and CH vibrations due to bonding interaction between OH and silver nanoparticles.

3.3. Moisture Content. For pristine PVA as well as for PVA/AgnP composites, two different moisture contents according to different sample treatment were evaluated: wet samples (without annealing treatment) and annealed samples at 120°C. Samples annealed at 120°C were obtained by the following fashion: a first scan was performed from 20°C to 120°C holding them at 120°C during 30 minutes and followed by cooling at 20°C, afterward a second heating from 20°C to 250°C was carried out in the same sample. Before annealing, a single scan on wet samples was performed for comparison. In the case of dry films, water content is reduced to the minimum possible by the heat treatment at 120°C during 30 minutes under controlled atmosphere inside the measuring cell.

Thermogravimetric measurements for pristine PVA are shown in Figure 3. The curve labeled as "wet PVA" corresponds to the first scan described above (from 20 to 120°C), while that labeled as "dry PVA" is the second scan of the same film after heat treatment at 120°C during 30 minutes. The water loss is about 4.16% and 0.01% for wet and dry samples, respectively; these results show that an important quantity of water is present before any measurement of PVA films. It is noteworthy that water content in PVA/AgnP composites is very close to that reported for pristine PVA; however, it slightly decreases as AgnP increases (from 4.0% for 0.05% of AgnP to 3.6% for 5% of AgnP). For all samples studied, the second scan after annealing at 120°C (dry samples) reveals water loss about 0.01%; therefore, samples annealed at 120°C do not need further heating treatment since at this water content, it is considered that samples are in the dry state.

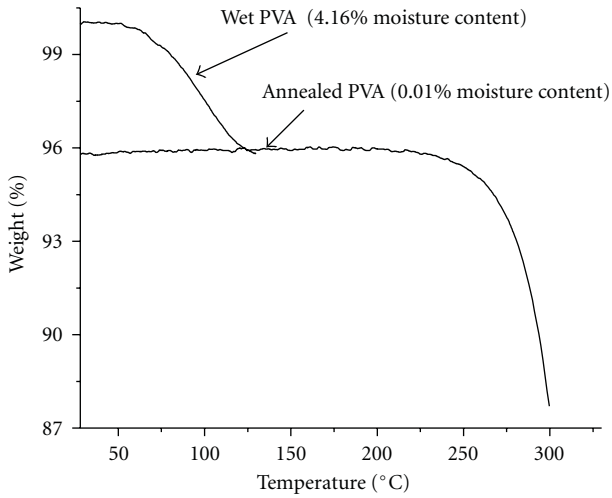

Figure 3: Thermogravimetric measurements in pristine PVA.

These same conditions labeled as wet and dry samples were applied in dielectric and DMA measurements discussed below.

3.4. Conductivity and Dielectric Results. The dc conductivity (σ_{dc}) of PVA and PVA/AgnP films was calculated by dielectric measurements using the methodology previously described elsewhere [20–22]. The dc resistance (R_{dc}) was obtained from the intersection of the semicircle and the real-part axis on the impedance plane (at $Z'' = 0$) as it is pointed out in the window insert of Figure 4, hence σ_{dc} can be calculated by the following relationship: $\sigma_{dc} = d/(R_{dc} \times A)$, where d are the thickness and A the area of the film, respectively. The Cole-Cole plot (real (Z') versus imaginary (Z'') parts of the impedance) shows the high frequency region semicircle, which is related to the bulk effect of PVA composites, while the linear region in the low frequency range is attributed to contacts effect [20].

As showed by TGA analysis, at ambient conditions water content in films is ca. 4.16 wt%, which reduces film resistance and masks the real conductivity behavior of composites. This is a delicate issue that needs to be considered when performing dielectric measurements especially in PVA films [19]. Due to this observation, dielectric measurements were carried out on dry films annealed in vacuum cell.

Figure 4 shows the change in dc conductivity as a function of temperature from 25 to 250°C for PVA and PVA/AgnP (0.5 and 1%) wet films. It can be seen in both films that conductivity increases as temperature increases due to the increased free volume and their respective ionic and segmental mobility [23]. This dependence unveils two well-defined regions at "low" (from 20°C to 80°C) and high (from 100°C to melting) temperatures, with an intermediate discontinuity between 80°C and 100°C associated to moisture evaporation [19]. Both relaxation regions disclose a well-defined non-Arrhenius behavior usually observed in many glass-formers and well described by the well-known Vogel-Fulcher-Tammann (VFT) relationship:

$$\sigma_{dc} = \sigma_0 e^{[-D/(T-T_0)]}, \quad (1)$$

where σ_{dc}, σ_0, and D are the conductivity, the preexponential factor, and a material constant, respectively, and T_0 is the so-called Vogel temperature related to the glass transition temperature [20]. This VFT-behavior is a clear evidence for the glass transition phenomenon; however, at this point this trend is not disclosed in the whole temperature range as in many amorphous polymers such as polypeptides [24]. At this point, it would be ambiguous to assign a T_g value of plasticized PVA and composites even though the plasticization of T_g is evident, the evaporation of water could be interfering.

Previously, these two regions were erroneously described as two Arrhenius-type relaxations in pristine PVA and Gd doped-PVA [25]; however, in those composites, moisture was not properly eliminated and the analysis was performed in a narrow temperature range (from 30°C to 180°C for composites and from 30°C to 160°C for pristine PVA), this do not allow to have a wider panorama of PVA and Gd doped-PVA relaxations giving rise to the erroneous interpretation. It is also important to mention that Hanafy did not discuss the evaporation of water zone (indicated in Figure 4), even when it is clearly observed in the ac conductivity versus the reciprocal temperature plot for PVA and Gd doped-PVA (see [25]).

From Figure 4, it is noteworthy that the evaporation of water (about 80°C–100°C) is more evident in pure PVA. This event confirms the existence of strong interactions between water and pristine PVA chains, and it clearly indicates the existence of strong hydrophilic groups acting as primary hydration sites: OH side groups. In pristine PVA, an overall increase in the molecular mobility with increasing water content occurs. This water evaporation region arises as a consequence of loosely bound water molecules connected to the reorientation of water molecules in water clusters around the primary hydration sites. The hydroxyl groups exert strong effects on the PVA molecular dynamics since the interactions between OH neighbors and absorbed moisture. The evaporation of water is less evident in PVA/AgnP composites; the conductivity slightly changes in the 80°C–100°C region, but it also represents a transition region from the low temperature relaxation to the high temperature relaxation.

As it was pointed out by IR analysis, the Ag nanoparticles directly interact with OH groups in PVA chains. This interaction decreases the number of PVA-water hydrogen bonds, reducing the number of available OH primary hydration sites to attach water molecules and consequently decreasing the moisture content. Since less amount of water is present in PVA/AgnP composites, the evaporation of water region is less evident. An additionally VFT-low temperature relaxation (between 20°C and 80°C) in all PVA/AgnP wet samples shows lesser curvature, thus indicating that the plasticizing effect of water is less effective.

On the other hand, wet PVA/AgnP composites have higher conductivity compared with pristine PVA, and it

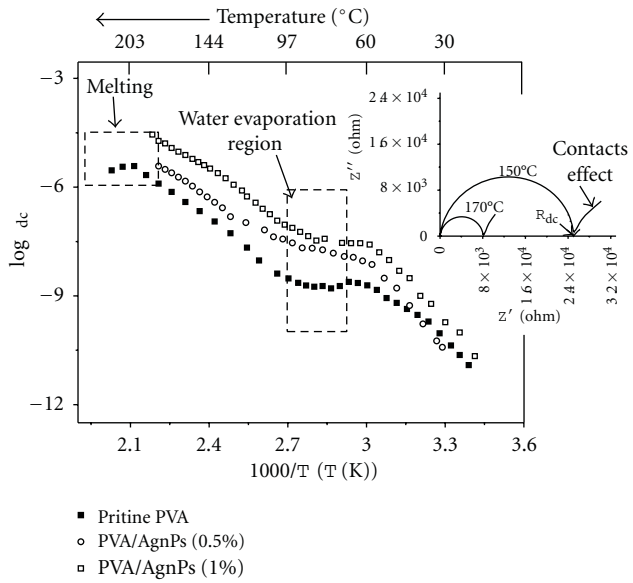

FIGURE 4: Conductivity (σ_{dc}) versus *1000/T*(K) for pure PVA and PVA/AgnP wet composites.

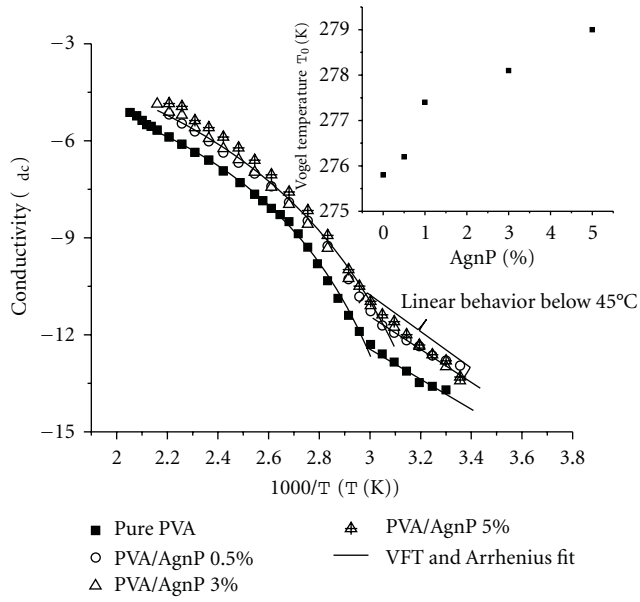

FIGURE 5: DC conductivity versus *1000/T*(K) for dry PVA/AgnP films (water content near zero). Window insert: Vogel Temperature *versus* AgnP % wt.

increases as AgnP weight percent increases as it can be seen in Figure 4. The formation of charge transfer complexes (CTCs) by the inclusion of metal nanoparticles cause reduction of the crystalline-amorphous interface decreasing the interfacial barrier and increasing the transition probability of electron hopping across the barrier and insulator chains, which in turn provides a conducting path through the amorphous regions of the polymer matrix resulting in enhanced conductivity in agreement with Mahendia et al. [16].

At the same time, the melting temperature of PVA is affected by the inclusion of AgnP; in PVA/AgnP composites, the melting temperature shifts to lower values. This can be explained as follows: the crystallinity of PVA results from strong intermolecular and intramolecular hydrogen bonding between PVA chains mainlythrough –OH groups. As it was shown by FTIR measurements, AgnP interactwith –OH groups of PVA; therefore, these AgnP-OH interactions decrease the intermolecular hydrogen bonding in PVA chains affecting its crystallinity, which in turns directly affects the melting temperature. This observation has been previously studied by our group [19].

On the other hand, based on previous studies on pure PVA [19], dry films of PVA/AgnP composites were obtained; in this case, water content is reduced to the minimum possible by a thermal treatment at 120°C during 30 minutes under controlled atmosphere inside the measuring cell (water content ca. 0.01%, determined by TGA analysis). After this thermal treatment, the films are cooled down at room temperature without opening the measuring cell, and a second heating is carried out on the same films. Now the conductivity behavior of PVA/AgnP composites is similar to the results previously reported on pristine dry PVA [19], disclosing a different trend compared with wet films, as it can be seen in Figure 5.

The second conductivity scan of dry films shows a single nonlinear VFT dependence from 45°C until melting, preceded by a linear behavior associated to a secondary relaxation process. This linear behavior will be discussed later.

The nonlinear behavior clearly described the glass transition phenomenon in PVA and PVA composites, thus, a single Vogel temperature can be now calculated from the fitting of the experimental data to the VFT model. This results support the statement about the plasticizing effect of water in the 20°C–80°C region and the evaporating of water region in the 80°C–100°C temperature range previously described.

Figure 5 reveals that when PVA/AgnP composites are analyzed in a broad temperature range, it is possible to observe a wider panorama on the true nature of the relaxation processes in PVA and PVA composites. In general, all reported studies on PVA composites and blends were reported up to 180°C.

As mentioned before, there is only one report on PVA-AgnP dielectric measurements [16]; however, it presents conductivity and dielectric studies as a function of AgnP concentration with no temperature variation; there are no previous reports on conductivity and dielectric measurements temperature dependencies regarding PVA-AgnP composites. Nonetheless, several dielectric studies were performed on PVA and PVA composites; however, most of them were carried out below 110°C [16, 23, 25–29]. In these studies, both VFT and Arrhenius behaviors have been reported in pure PVA and its composites in the same narrow temperature range.

Agrawal and Awadhia [26] and Linares et al. [27] showed the VFT behavior for the temperature dependence of conductivity in pure PVA and PVA-based gel electrolytes

Table 1: Vogel and glass transition temperatures for different AgnP content.

Sample	T_0 (K)	T_g (°C)
Pristine PVA	275.8	72.65
PVA/AgnP (0.5 wt%)	276.8	73.15
PVA/AgnP (1 wt%)	277.5	74.35
PVA/AgnP (3 wt%)	278.1	74.95
PVA/AgnP (5 wt%)	279.0	75.85

in the 20–100°C temperature range, and in pure PVA and in PVDF/PVA blends in the 20–110°C temperature range respectively. On the other hand, Hanafy [25] reported two linear behaviors in the 20°C to 180°C temperature range for PVA and Gd-doped PVA. Bhargav et al. [23] suggest an Arrhenius behavior in pure PVA and PVA:NaI complex in the 20–100°C temperature range, as well as Hema et al. [28] in the 20–70°C temperature range in pure PVA and PVA-NH4Br complexes. Zhang et al. [29] showed the relaxation time temperature dependence of PVA/MWCNT composites with 3 wt% MWCNT suggesting an Arrhenius-type dependence in the 20°C to 145°C temperature range. In the latter case, no results for pure PVA are reported. Finally, Mahendia et al. [16] carried out electrical conductivity and dielectric spectroscopy studies of PVA-Ag nanocomposite films; they observed a strong influence of the concentration of silver nanoparticles on the electrical conductivity and dielectric properties of PVA matrix. However, these results are at room temperature and they do not show temperature dependencies of conductivity and dielectric results. Despite of all the above studies, one cannot conclude the existence of a non-Arrhenius, α-relaxation process.

The nature of the molecular dynamics of Arrhenius-type and VFT-type behaviors is very different; it is very important to establish which of them is truly present in a polymer system. Arrhenius-type relaxation is related to the ions that are decoupled from the polymer host, and activated hopping is required for ionic transport. VFT behavior describes the cooperative motion, which occurs when the system is in the vicinity of a glass-transition.

In the case of PVA and PVA composites, VFT behavior was not observed in a number of previous studies on PVA composites because the effect of water was not properly taken into account [23, 25, 28, 29]. The relaxation analysis on those studies was based on temperature ranges not exceeding 160°C; most of them were done up to 100°C. These two factors, moisture and temperature range, are extremely important to gain a better understanding of PVA composites molecular dynamics.

In this work, it is clearly observed that a wider temperature range (in this case from 20°C to 250°C) and an adequate moisture content elimination allow to disclose the true nature of the molecular dynamics in PVA and PVA composites; in this case, the VFT behavior related to the glass transition.

The Vogel temperature (T_0) calculated from de VFT relationship (1) as a function of AgnP content for PVA/AgnP composites is plotted in the window insert of Figure 5 and

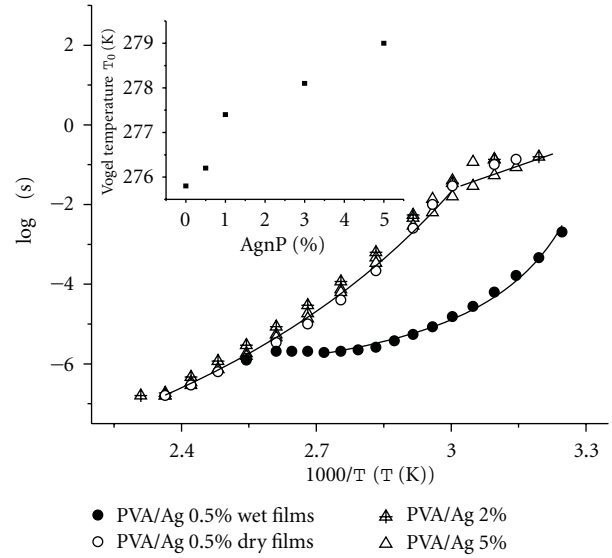

Figure 6: Relaxation time (τ) versus *1000/T (T in* K*)*.

it is shown in Table 1. In general, it can be observed that T_0 increases as AgnP content increases. For most polymers, the relationship between the glass transition temperature T_g and T_0 is $T_g = T_0 + C$, where C is an empirical constant. In many dielectric studies, C is taken as 70 K [30–32]. Table 1 shows the estimated T_g values for pristine PVA and PVA/AgnP composite as a function of AgnP content (C value is taken as 70 K).

Therefore, we can say that the glass transition temperature of PVA composites increases as AgnP weight percent increases in contrast with previous results in Ag-PVA films [33]. Moisture content of PVA composites is lower than that of pristine PVA due to the interaction between OH groups and AgnP; higher glass transition temperature values for PVA composites are expected. AgnP bonds to hydroxyl groups reduce the plasticizer effect and complicate molecular motion in PVA chains resulting in an increase in T_g values.

On the other hand, it has recently been recognized that contact and interfacial polarizations are to account when analyzing dielectric spectra. Indeed, it is well known that dc conductivity strongly affects the loss factor ε'' in the low-frequency range, and a correction must be applied to unmask the polymer dielectric effects [20]. dc Conductivity and contact polarization effect could mask the real dielectric relaxation processes in the low frequency range; therefore, to analyze the dielectric processes in detail, the complex permittivity ε^* is converted to the complex dielectric modulus M^* by the following equation: $M^* = 1/\varepsilon^* = M' + iM'' = [\varepsilon'/(\varepsilon'^2+\varepsilon''^2)+\mathbf{i}\ \varepsilon''/(\varepsilon'^2+\varepsilon''^2)]$, where M' and M'' are the real and imaginary parts of electric modulus and ε' and ε'' are the real and imaginary part of permittivity, respectively. The dielectric modulus is commonly used to analyze dielectric experimental data because interfacial polarization, electrode contribution, and conductivity dc effect do not affect M'' peak. Note that M'' is temperature dependent [34].

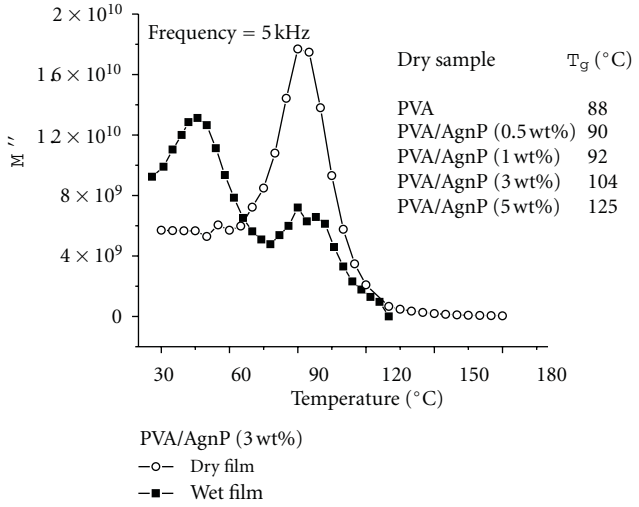

FIGURE 7: Imaginary part (M'') of the dielectric modulus (M^*) versus Temperature (°C) for PVA/AgnP (3%wt) wet and dry films.

The relaxation time dependence on temperature shown in Figure 6 was obtained from the maximum of the imaginary part of the dielectric modulus (M^*), with the M'' peak ($\tau = 1/2\pi f_{\max}$) calculated at each temperature. The wet films display the trend akin to conductivity as temperature increases: two VFT behaviors in the high and low temperature range separated by moisture evaporation effect in the 80°C to 100°C temperature range. The T_0 calculated from the VFT model for relaxation time: $\tau_{dc} = \tau_0 e^{[D/(T-T_0)]}$ (where τ, τ_0, and D are the relaxation time, the preexponential factor, and a material constant, respectively, and T_0 is the so called Vogel temperature) for all composites are shown in window insert of Figure 6. In dry films, once again the Vogel temperature increases as AgnP concentration increases and relaxation times increase as AgnP concentration increases, and these values are in agreement with those calculated above by the conductivity plot. The interaction of AgnP with OH groups hinders the mobility of PVA chains resulting in higher relaxation times for this primary relaxation.

The α-relaxation process is strongly dependent on moisture content since for the conductivity dependence on temperature, the relaxation time dependence for dry films is very different than that for wet films. After annealing, two well-defined behaviors are observed. A nonlinear behavior from 45°C to melting related to the α-relaxation process, and below 45°C an Arrhenius behavior associated to a secondary relaxation process which will be discussed later.

The results suggest a plasticizing effect of water on PVA composites in agreement with the results previously reported for pristine PVA [19]. A plasticized T_g can be observed in wet films through a nonlinear behavior described by the VFT model separated by the water evaporation region from a second nonlinear behavior disclosed at higher temperature. However, once water is eliminated by thermal treatment, this plasticized T_g vanished and only one nonlinear behavior is observed from 45°C to melting. Also the relaxation time for wet films is lower since the segmental motion is favored by water, by increasing the free volume between chains and because the orientation polarization of polar molecules is slowed down. However, this plasticizing effect is less evident in PVA composites when compared to pristine PVAwith their water content being lower.

More information about moisture effect is provided by means of the complex modulus M^*, specifically by the M'' versus *Temperature* plot for wet and dry PVA and PVA composites as it is shown in Figure 7. In wet samples, two relaxations peaks (one below 50°C and another one above 80°C) at 5 kHz were found. As frequency increases, both peaks shift towards higher temperatures. These two relaxation peaks have been previously reported by other authors from M'', ε'', and tan δ plots for pure PVA, PVA blends, and composites [23, 25, 32–34]. These relaxations were previously assigned as the β-relaxation ascribed to side-group dipoles orientation (relaxation below 80°C, T_β = 40°C for pristine PVA [not shown] and 46°C for PVA/AgnP composite) and the glass transition of PVA (ca. T_g = 85°C), respectively [23, 25, 27, 35, 36]. Nonetheless, our results show that for dry samples the lower temperature relaxation peak (below 50°C) vanishes after annealing the films at 120°C, remaining the α-relaxation peak at the same temperature for each frequency. This fact leads to the conclusion that the low temperature relaxation in wet samples can be traced to a moisture effect, and it does not correspond to a local mode β-relaxation. In this study, for pristine PVA dry samples T_g is ca. 88°C in agreement with previous results [19]. From Figure 7, it can also be observed that T_g increases with AgnP content; for PVA with AgnP 3 wt%, T_g is ca. 92°C. T_g values of composites and pristine PVA, calculated from the dielectric modulus plots as a function of AgnP content in dry films, are shown in Figure 7. It could be observed, that these T_g values are very different from those calculated by the empirical rule. Based upon our previous studies on pristine PVA [19] and chitin and chitosan nanocomposites [20–23], we propose to use the T_g analysis based upon the modulus rather than the use of the empirical rule.

PVA and moisture interaction would correspond to the formation of hydrogen bonds between PVA hydroxyl groups and water, and hydrogen bonds are the dominant interaction responsible for the structure as well as its molecular dynamics. It is possible that the interaction between OH groups and moisture is capable to destroy inter- and intrachain bonding in PVA affecting its crystalline regions; therefore, water acts as a plasticizer by an increase of the free volume in the amorphous phase [37]. This OH groups moisture interaction is disturbed by AgnP inclusion, and as a consequence, the molecular dynamics of both relaxation processes is strongly affected. The low temperature relaxation shifts to higher temperature as AgnP content increases resulting from lower moisture content and lower mobility.

On the other hand, regarding the behavior disclosed in dry films below 45°C previously observed in Figures 5 and 6 (conductivity and relaxation time dependences), it could be seen that this relaxation follows a single Arrhenius behavior, which corresponds to a secondary relaxation process. In glassy polymers, the chains are frozen and molecular motions involved in secondary relaxations occur at higher time

scale (i.e., higher relaxation times) as it is observed in Figure 6. This linear dependence can be explained based on the variable range hopping model. For most polymers this dependence of the dc Conductivity on temperature (T) is often represented by the variable range hopping (VRH) model proposed by Mott [38, 39]:

$$\sigma_{\mathrm{dc}}(T) = \sigma_0 \exp\left[-\left(\frac{T_0}{T}\right)^{\gamma}\right], \quad (2)$$

where σ_0 can be considered as the limiting value of conductivity at infinite temperature and $\sigma_0 \sim 1/T^{1/2}$ [40], T_0 depends on the localization and density of the states, and the exponent γ is related to the dimensionality d of the transport process via the equation $\gamma = 1/(1+d)$, where $d = 1, 2, 3$. The applicability of the VRH model is examined by plotting the experimental results in the form of $\log \sigma(T)^{1/2}$ versus $T^{-\gamma}$ [39].

The experimental data in the 0°C to 45°C temperature range plotted according to the VRH model are presented on Figure 8. It is noteworthy that the dependence $\log \sigma(T)^{1/2}$ versus $T^{-\gamma}$ can be linearly fitted with both $\gamma = 1/4$ and 1/3. However, the best least-square fitting is obtained for $\gamma = 1/4$ (with $R^2 = 0.994$). This value corresponds to a three-dimensional transport process as explained before.

Furthermore, Linares et al. [28] reported the same linear behavior below 21°C for PVDF/PVA blends with different weight percent ratios. They ascribed this low temperature relaxation to a subglass relaxation process occurring in the amorphous phase and associated it to the polar groups attached to the polymeric chain. However, in our case, the application of the variable range hopping model is more appropriate to describe the AgnP-PVA system, since the inclusion of metal nanoparticles give rise to the formation of charge transfer complexes (CTCs) causing the reduction of the crystalline-amorphous interface, decreasing the interfacial barrier and increasing the transition probability of electron hopping across the barrier and insulator chains, which in turn provides a conducting path through the amorphous regions of the polymer matrix resulting in enhanced conductivity [16].

3.5. Dynamic Mechanical Analysis (DMA). Gautam and Ram [33] report the preparation and thermomechanical properties of Ag-PVA nanocomposites; however, they do not discuss the strong influence of water content on the composite's relaxation processes. In the mentioned study, it is evident that authors assigned the glass transition temperature of PVA/AgnP composites dismissing the effect of water on the relaxation process of composites since the reported values are below 40°C which correspond to the plasticized T_g.

DMA analysis performed at 1 Hz in pristine PVA, and its composites wet and dry films are shown in Figure 9. All samples showed similar behaviors before and after being annealed. It can be observed that the tan δ peak in wet films shows a relaxation process near 40°C. This low temperature DMA peak was previously assigned several times as the glass transition temperature of pristine PVA and several PVA composites. Gautam and Ram [33] assigned T_g

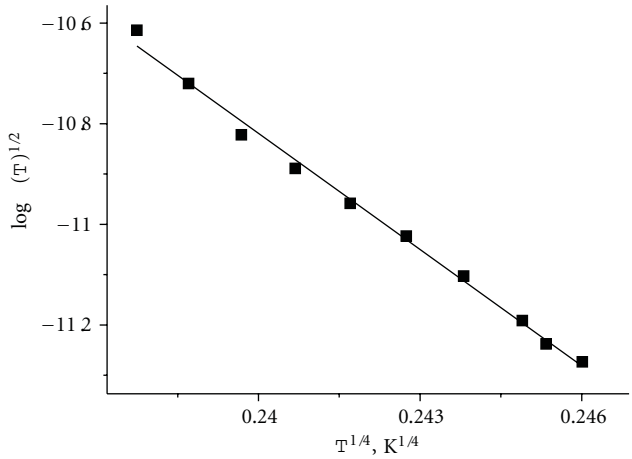

Figure 8: $\log \sigma T^{1/2}$ versus $T^{1/4}$ for pure PVA.

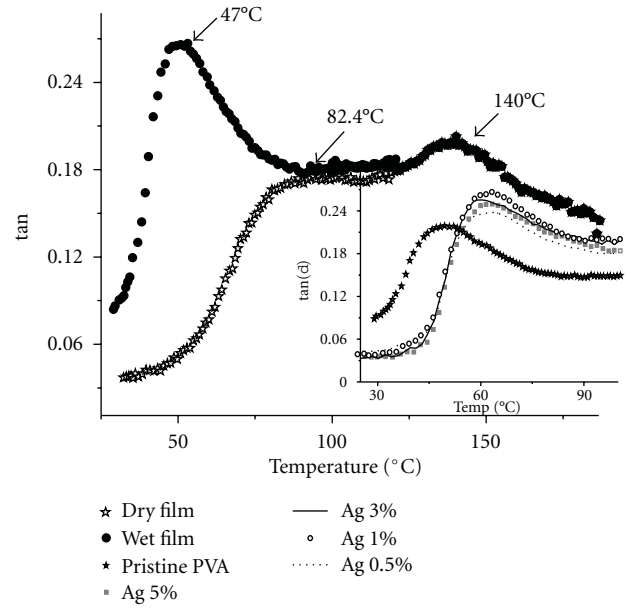

Figure 9: tan δ versus temperature for dry and wet pristine PVA film. Window insert: tan δ versus temperature for wet pristine PVA and wet PVA/AgnP composites.

values between 40°C and 36°C in Ag-PVA nanocomposites depending upon Ag content. Tian and Tagaya [41] observed this peak around 50°C and described it as the glass transition of pristine PVA. They also show peaks for perlite/PVA and OMMT/PVA nanocomposites without taking into account water content. Yang et al. [42] assigned 44°C and 45°C values for the glass transition temperatures of pristine PVA and PVA/10 wt% montmorillonite (MMT) composites, respectively. They discussed that the T_g values from the DMA analyses for polymer membranes were lower than those from the DSC analyses (71–82°C) because the sensitivity for the measurement of a glass transition temperature by DMA is more sensitive than that by DSC.

However, it is noteworthy that this tan δ peak vanishes in dry films after annealing at 120°C; consequently, this peak

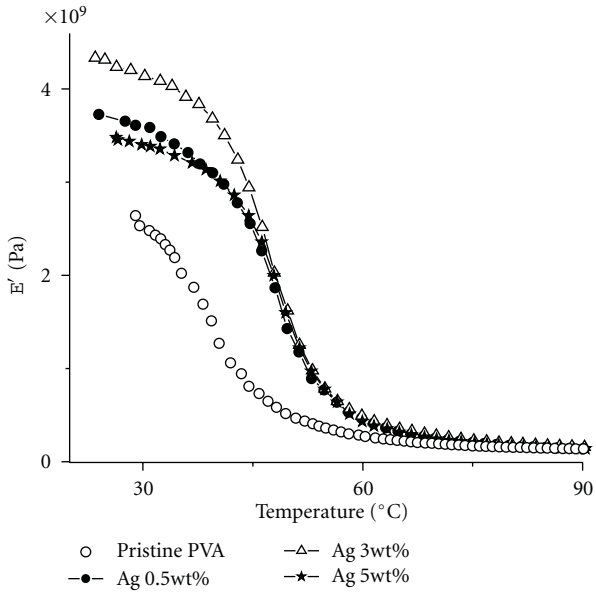

Figure 10: DMA storage modulus (E') versus temperature for wet pristine PVA and wet PVA/AgnP composites.

is related to water-polymer motions which mask the glass transition in wet films. After water evaporation, dry films disclose the glass transition event above 80°C.

Window insert of Figure 9 shows the variation of tan δ peak in wet PVA and PVA/AgnP composites films (water content around 4.1% calculated by TGA). Once again the influence of AgnP on PVA moisture absorption capacity is observed, that is, water-polymer motion is restricted by the presence of silver nanoparticles, which reduces moisture content in composites shifting the relaxation process from 47°C for pristine PVA to 63.8°C for the higher concentration of AgnP (5 wt%).

The storage modulus is shown in Figure 10, it can be seen that it increases as AgnP content in films increases up to 3 wt% suggesting significant reinforcement effect of Ag nanoparticles. Nanoparticles restrict the polymer's chain mobility due to their large surface area and their van der Waals attraction to the polymer matrix, causing the strengthening of mechanical properties of nanocomposite films [33]. However, at 5 wt% of AgnP, the storage modulus decreases compared to lower concentrations, but it remains higher than pristine PVA.

Gautam and Ram [33] showed this reinforcement up to 0.2 wt% of AgnP and then decreases for higher concentrations, being even lower than that of pristine PVA at concentration above 1 wt%. This decrease in the storage modulus is ascribed to the formation of large agglomerates, which in turns affects moisture content of PVA. The interaction between OH groups of PVA and moisture affects the crystalline regions. This OH groups moisture interaction is disturbed by AgnP inclusion resulting in lower moisture content and lower mobility; thus the strengthening of AgnP is less effective at higher concentrations of nanoparticles.

4. Concluding Remarks

The molecular dynamics of PVA/AgnP composites was studied by impedance spectroscopy in the 0.1 Hz to 110 MHz and 20°C to 300°C frequency and temperature ranges, respectively. As well as for pristine PVA, improper water elimination analysis in PVA composites could lead to misinterpretation of thermal relaxations in PVA composites such that a plasticized T_g for wet films has been assigned as a secondary β-relaxation in a number of previous studies in the literature.

Two well-defined nonlinear regions at low and high temperatures, with an intermediate discontinuity between 80°C and 100°C associated to moisture evaporation, were observed in wet PVA/AgnP composites films in agreement with pristine PVA behavior. Previously, these two regions were erroneously assigned to two Arrhenius-type relaxations in pristine and doped PVA. The evaporation of water and its plasticizing effect are more evident in pure PVA confirming the existence of strong interaction between OH groups of PVA chains and AgnP, as shown by FTIR analysis. Dry films show a single nonlinear VFT dependence (from 45°C until melting) associated to the α-relaxation and, therefore, to the glass transition phenomenon. T_g of composites increases as AgnP content increases from 88°C for pristine PVA to 125°C for PVA/AgnP (5 wt%). Below 45°C, dry films exhibit a single Arrhenius behavior showing a 3D hopping conductivity as explained based on the variable range hopping model.

PVA/AgnP composites have higher conductivity compared to pristine PVA, and it increases as AgnP weight percent increases. The inclusion of metal nanoparticles decreases the interfacial barrier and increases the transition probability of electron hopping across the barrier and insulator chains, which in turn provides a conducting path through the amorphous regions of the polymer matrix resulting in enhanced conductivity.

Finally, DMA measurements support the statement that a secondary relaxation was erroneously assigned as the glass transition of PVA and composites in previous reports.

Acknowledgments

The authors thank José Alfredo Muñoz, Araceli Mauricio, and María del Carmen Díaz for their help provided. They also thank CONACYT (Mexican Government) for partial financial support. The authors are not partially or fully associated with Nanotechnologies nor do they endorse the use of their products.

References

[1] A. Henglein, "Small-particle research: physicochemical properties of extremely small colloidal metal and semiconductor particles," *Chemical Reviews*, vol. 89, no. 8, pp. 1861–1873, 1989.

[2] R. Chapman and P. Mulvaney, "Electro-optical shifts in silver nanoparticle films," *Chemical Physics Letters*, vol. 349, no. 5-6, pp. 358–362, 2001.

[3] L. N. Lewis, "Chemical catalysis by colloids and clusters," *Chemical Reviews*, vol. 93, no. 8, pp. 2693–2730, 1993.

[4] A. Kiesow, J. E. Morris, C. Radehaus, and A. Heilmann, "Switching behavior of plasma polymer films containing silver nanoparticles," *Journal of Applied Physics*, vol. 94, no. 10, pp. 6988–6990, 2003.

[5] Y. Min, M. Akbulut, K. Kristiansen, Y. Golan, and J. Israelachvili, "The role of interparticle and external forces in nanoparticle assembly," *Nature Materials*, vol. 7, no. 7, pp. 527–538, 2008.

[6] J. L. Elechiguerra, J. L. Burt, J. R. Morones et al., "Interaction of silver nanoparticles with HIV-1," *Journal of Nanobiotechnology*, vol. 3, article 6, 2005.

[7] A. L. Stepanov, V. N. Popok, I. B. Khaibullin, and U. Kreibig, "Optical properties of polymethylmethacrilate with implanted silver nanoparticles," *Nuclear Instruments and Methods in Physics Research, Section B*, vol. 191, no. 1–4, pp. 473–477, 2002.

[8] Y. Badr and M. A. Mahmoud, "Enhancement of the optical properties of poly vinyl alcohol by doping with Silver nanoparticles," *Journal of Applied Polymer Science*, vol. 99, no. 6, pp. 3608–3614, 2006.

[9] P. C. Lebaron, Z. Wang, and T. J. Pinnavaia, "Polymer-layered silicate nanocomposites: an overview," *Applied Clay Science*, vol. 15, no. 1-2, pp. 11–29, 1999.

[10] J. M. Yeh, S. J. Liou, C. Y. Lin, C. Y. Cheng, Y. W. Chang, and K. R. Lee, "Anticorrosively enhanced PMMA-clay nanocomposite materials with quaternary alkylphosphonium salt as an intercalating agent," *Chemistry of Materials*, vol. 14, no. 1, pp. 154–161, 2002.

[11] T. H. Kim, L. W. Jang, D. C. Lee, H. J. Choi, and M. S. John, "Synthesis and rheology of intercalated polystyrene/Na^+-Montmorillonite nanocomposites," *Macromolecular Rapid Communications*, vol. 23, no. 3, pp. 191–195, 2002.

[12] Y. J. Lee and W. S. Lyoo, "Preparation of Atactic poly(vinyl alcohol)/silver composite nanofibers by electrospinning and their characterization," *Journal of Applied Polymer Science*, vol. 115, no. 5, pp. 2883–2891, 2010.

[13] V. K. Sharma, R. A. Yngard, and Y. Lin, "Silver nanoparticles: green synthesis and their antimicrobial activities," *Advances in Colloid and Interface Science*, vol. 145, no. 1-2, pp. 83–96, 2009.

[14] K. H. Hong, J. L. Park, I. N. Hwan Sul, J. H. Youk, and T. J. Kang, "Preparation of antimicrobial poly(vinyl alcohol) nanofibers containing silver nanoparticles," *Journal of Polymer Science, Part B*, vol. 44, no. 17, pp. 2468–2474, 2006.

[15] Z. H. Mbhele, M. G. Salemane, C. G. C. E. van Sittert, J. M. Nedeljković, V. Djoković, and A. S. Luyt, "Fabrication and characterization of silver-polyvinyl alcohol nanocomposites," *Chemistry of Materials*, vol. 15, no. 26, pp. 5019–5024, 2003.

[16] S. Mahendia, A. K. Tomar, and S. Kumar, "Electrical conductivity and dielectric spectroscopic studies of PVA-Ag nanocomposite films," *Journal of Alloys and Compounds*, vol. 508, no. 2, pp. 406–411, 2010.

[17] W. Brostow, R. Chiu, I. M. Kalogeras, and A. Vassilikou-Dova, "Prediction of glass transition temperatures: binary blends and copolymers," *Materials Letters*, vol. 62, no. 17-18, pp. 3152–3155, 2008.

[18] N. R. Jadhav, V. L. Gaikwad, K. J. Nair, and H. M. Kadam, "Glass transition temperature: basics and application in pharmaceutical sector," *Asian Journal of Pharmaceutics*, vol. 3, no. 2, pp. 82–89, 2009.

[19] J. B. González-Campos, Z. Y. García-Carvajal, E. Prokhorov et al., "Revisiting thermal relaxations of poly(vinyl alcohol)," *Journal of Applied Polymer Science*, vol. 125, pp. 4082–4090, 2012.

[20] J. B. Gonzalez-Campos, E. Prokhorov, G. Luna-Bárcenas et al., "Relaxations in chitin: evidence for a glass transition," *Journal of Polymer Science, Part B*, vol. 47, no. 9, pp. 932–943, 2009.

[21] J. B. Gonzalez-Campos, E. Prokhorov, G. Luna-Bárcenas, A. Fonseca-García, and I. C. Sanchez, "Dielectric relaxations of chitosan: the effect of water on the α-relaxation and the glass transition temperature," *Journal of Polymer Science, Part B*, vol. 47, no. 22, pp. 2259–2271, 2009.

[22] J. B. Gonzalez-Campos, E. Prokhorov, G. Luna-Bárcenas et al., "Chitosan/silver nanoparticles composite: molecular relaxations investigation by dynamic mechanical analysis and impedance spectroscopy," *Journal of Polymer Science, Part B*, vol. 48, no. 7, pp. 739–748, 2010.

[23] P. B. Bhargav, B. A. Sarada, A. K. Sharma, and V. V. R. N. Rao, "Electrical conduction and dielectric relaxation phenomena of PVA based polymer electrolyte films," *Journal of Macromolecular Science, Part A*, vol. 47, no. 2, pp. 131–137, 2010.

[24] A. L. Lee and A. J. Wand, "Microscopic origins of entropy, heat capacity and the glass transition in proteins," *Nature*, vol. 411, no. 6836, pp. 501–504, 2001.

[25] T. A. Hanafy, "Dielectric relaxation and alternating-current conductivity of gadolinium-doped poly(vinyl alcohol)," *Journal of Applied Polymer Science*, vol. 108, no. 4, pp. 2540–2549, 2008.

[26] S. L. Agrawal and A. Awadhia, "DSC and conductivity studies on PVA based proton conducting gel electrolytes," *Bulletin of Material Science*, vol. 27, no. 6, pp. 523–527, 2004.

[27] A. Linares, A. Nogales, D. R. Rueda, and T. A. Ezquerra, "Molecular dynamics in PVDF/PVA blends as revealed by dielectric loss spectroscopy," *Journal of Polymer Science, Part B*, vol. 45, no. 13, pp. 1653–1661, 2007.

[28] M. Hema, S. Selvasekerapandian, and G. Hirankumar, "Vibrational and impedance spectroscopic analysis of poly(vinyl alcohol)-based solid polymer electrolytes," *Ionics*, vol. 13, no. 6, pp. 483–487, 2007.

[29] J. Zhang, M. Mine, D. Zhu, and M. Matsuo, "Electrical and dielectric behaviors and their origins in the three-dimensional polyvinyl alcohol/MWCNT composites with low percolation threshold," *Carbon*, vol. 47, no. 5, pp. 1311–1320, 2009.

[30] F. Garcia, A. Garcia-Bernabe, V. Compan, R. Diaz-Calleja, J. Guzman, and E. Riande, "Relaxation behavior of acrylate and methacrylate polymers containing dioxacyclopentane rings in the side chains," *Journal of Polymer Science B*, vol. 39, no. 3, pp. 286–299, 2001.

[31] V. Compan, J. Guzman, R. Diaz-Calleja, and E. Riande, *Relxation behavior of methacrylic polymers with bulky hydrophilic groups in their structuresJournal of Polymer Science B*, vol. 37, pp. 3027–3037, 1999.

[32] G. G. Raju, *Dielectrics in Electrical Fields*, Marcel Dekker, New York, NY, USA, 2003.

[33] A. Gautam and S. Ram, "Preparation and thermomechanicalproperties of Ag-PVA nanocomposite films," *Materials Chemistry and Physics*, vol. 119, no. 1-2, pp. 266–271, 2010.

[34] M. Köhler, P. Lunkenheimer, and A. Loidl, "Dielectric and conductivity relaxation in mixtures of glycerol with LiCl," *European Physical Journal E*, vol. 27, no. 2, pp. 115–122, 2008.

[35] M. D. Migahed, N. A. Bakr, M. I. Abdel-Hamid, O. El-Hanafy, and M. El-Nimr, "Dielectric relaxation and electric modulus behavior in poly(vinyl alcohol)-based composite systems," *Journal of Applied Polymer Science*, vol. 59, no. 4, pp. 655–662, 1996.

[36] K. P. Singh and P. N. Gupta, "Study of dielectric relaxation in polymer electrolytes," *European Polymer Journal*, vol. 34, no. 7, pp. 1023–1029, 1998.

[37] M. C. Hernández, N. Suárez, L. A. Martínez, J. L. Feijoo, S. Lo Mónaco, and N. Salazar, "Effects of nanoscale dispersion in the dielectric properties of poly(vinyl alcohol)-bentonite nanocomposites," *Physical Review E*, vol. 77, no. 5, Article ID 051801, 2008.

[38] N. F. Mott, *Metal-Insulator Transitions*, Taylor & Francis, London, UK, 1990.

[39] G. C. Psarras, "Hopping conductivity in polymer matrix-metal particles composites," *Composites Part A*, vol. 37, no. 10, pp. 1545–1553, 2006.

[40] S. Capaccioli, M. Lucchesi, P. A. Rolla, and G. Ruggeri, "Dielectric response analysis of a conducting polymer dominated by the hopping charge transport," *Journal of Physics Condensed Matter*, vol. 10, no. 25, pp. 5595–5617, 1998.

[41] H. Tian and H. Tagaya, "Dynamic mechanical property and photochemical stability of perlite/PVA and OMMT/PVA nanocomposites," *Journal of Materials Science*, vol. 43, no. 2, pp. 766–770, 2008.

[42] C. C. Yang, Y. J. Lee, and J. M. Yang, "Direct methanol fuel cell (DMFC) based on PVA/MMT composite polymer membranes," *Journal of Power Sources*, vol. 188, no. 1, pp. 30–37, 2009.

Hindawi Publishing Corporation
Journal of Nanomaterials
Volume 2012, Article ID 894539, 9 pages
doi:10.1155/2012/894539

Research Article

Synthesis and Control of the Shell Thickness of Polyaniline and Polypyrrole Half Hollow Spheres Using the Polystyrene Cores

Su-Ryeon Yun,[1] Gyeong-Ok Kim,[1] Chan Woo Lee,[2] Nam-Ju Jo,[3] Yongku Kang,[4] and Kwang-Sun Ryu[1]

[1] *Department of Chemistry, University of Ulsan, Daehak-ro 93, Nam-gu, Ulsan 680-749, Republic of Korea*
[2] *Department of Chemical Engineering, Hanyang University, Seoul 133-791, Republic of Korea*
[3] *Department of Polymer Science & Technology, Pusan National University, Busan 609-735, Republic of Korea*
[4] *Korea Research Institute of Chemical Technology, Daejeon 305-600, Republic of Korea*

Correspondence should be addressed to Kwang-Sun Ryu, ryuks@ulsan.ac.kr

Received 17 February 2012; Revised 11 May 2012; Accepted 21 May 2012

Academic Editor: Luiz Antonio Ferreira Coelho

Polyaniline (Pani) and polypyrrole (Ppy) half hollow spheres with different shell thicknesses were successfully synthesized by three steps process using polystyrene (PS) as the core. The PS core was synthesized by emulsion polymerization. Aniline and pyrrole monomers were polymerized on the surface of the PS core. The shells of Pani and Ppy were fabricated by adding different amounts of aniline and pyrrole monomers. PS cores were dissolved and removed from the core shell structure by solvent extraction. The thicknesses of the Pani and Ppy half hollow spheres were observed by FE-SEM and FE-TEM. The chemical structures of the Pani and Ppy half hollow spheres were characterized by FT-IR spectroscopy and UV-Vis spectroscopy. The shell thicknesses of the Pani half hollow spheres were 30.2, 38.0, 42.2, 48.2, and 52.4 nm, while the shell thicknesses of the Ppy half hollow spheres were 16.0, 22.0, 27.0, and 34.0 nm. The shell thicknesses of Pani and Ppy half hollow spheres linearly increased as the amount of the monomer increased. Therefore, the shell thickness of the Pani and Ppy half hollow spheres can be controlled in these ranges.

1. Introduction

Conducting polymers have recently received much attention due to their long conjugation lengths, metallic conductivity, and their promise for applications in molecular wires, nanoelectronics, optoelectronic devices, and biomedical devices [1–3]. Among the conjugated conducting polymers, Pani and Ppy have drawn the most attention due to their superior electroactivity, good electrical conductivity, and chemical stability. Owing to their physical, chemical, and electrochemical properties, Pani and Ppy have been applied in many different fields including sensors, electronics, semitransistors, flat-panel displays, cable shielding, ion-selective membranes, electrocatalysis, and as the cathode material in rechargeable batteries [4–6].

Pani and Ppy are known as an inherent electrically conductive polymer due to the conjugation of the single and double bonds alternating within the macromolecular architecture. The extra electrons of a double bond in a conjugated system are free to wander or move through the polymer chain, which induces electrical conductivity [7–10]. The conductivity of Pani and Ppy can be significantly improved by doping with oxidizing agents. During the oxidation process, an adequate amount of anions from the solutions with HCl and $FeCl_3 \cdot 6H_2O$ is usually incorporated to compensate the electrogenerated positive charges (polaronic or bipolaronic species) in Scheme 1. The electrical conductivity of Pani and Ppy can be effectively increased to the level of a few tenths of S/cm through p-doping [11–13].

Recently, there has been immense interest in the fabrication of core-shell particles with unique and tailored properties for various applications in material sciences [14–16]. Among the core-shell particles, inorganic coated polymer (core-shell) capsules and hollow spheres have increasingly attracted interest because of their potential applications in catalysis, controlled delivery, artificial cells, light fillers, low dielectric constant materials, acoustic insulation, the paint industry, and photonic crystals.

The latex sphere approach uses polystyrene spheres as a template, assisted by a template pretreatment process or layer-by-layer technique [14, 15]. However, the hollow spheres that are obtained have smooth surfaces. Recently, Wan et al. developed an "emulsion template" approach to prepare hollow Pani spheres in an aqueous media using spherical micelles composed of a dopant and monomer as a template [16, 17]. Otherwise, template spheres have been prepared by simple sulfonation of PS spheres or have been purchased for use. Pani and Ppy were polymerized by an electrochemical method. Moreover, the sizes of Pani and Ppy hollow spheres are generally widely dispersed, and the control of the morphology of Pani and Ppy is difficult. The PS cores are then removed by solvents, which are usually expensive and toxic organic solvents such as DMF, THF, chloroform, and toluene [15, 18–20].

In most of paper, hollow sphere structures were formatted by the layer-by-layer method. But in this paper, layer-by-layer method was partly changed for surface modification of PS. This method was progressed with three steps. The PS templates were polymerized by micelle of anionic surfactant for using core. The surface of PS was directly modified by anion surfactant and formatted negative charge. The Pani and Ppy were evenly coated on surface-modified PS because doped Pani and Ppy have positive charge, respectively. And then, the PS cores were dissolved using organic solvent to produce Pani hollow sphere. This method is described in Scheme 1. We report an approach to make PS templates with the same size by polymerization using a chemical method. We prepared Pani and Ppy with a half hollow sphere structure and controlled the shell thickness. Since Pani and Ppy are well viscously aggregated, the thickness control of Pani and Ppy with a core-shell structure is not easy. Thus, we aimed to control the shell thickness in the core-shell or half hollow sphere structure. A specific amount of monomer was added to control the shell thickness of Pani and Ppy in the core-shell or half hollow sphere structure. We demonstrated the ability to obtain a desired shell thickness of Pani and Ppy half hollow spheres.

2. Experimental

Styrene (>99%, Aldrich), aniline (>99.5%, Aldrich), and pyrrole (98%, Aldrich) monomers were purified by passing through aluminum oxide (~150 mesh, 58 Å) and distillation before being stored in a refrigerator. Potassium peroxodisulfate ($K_2S_2O_8$, KPS, 99%), ammonium persulfate ($(NH_4)_2S_2O_8$, APS, 98%) as initiator, dodecyl sulfate, sodium dodecyl sulfate ($C_{12}H_{25}O_4Sna$, SDS, 99%) as surfactant, divinylbenzene (DVB, 55% mixture of isomers) as a cross-linking agent, hydrochloric acid (HCl, 37%), and iron(III) chloride hexahydrate ($FeCl_3 \cdot 6H_2O$, 97%) were used as received from Aldrich. Acetone was used as received from SK Chemical.

The PS was synthesized by emulsion polymerization. The styrene was refined by Al_2O_3 to remove the polymerization inhibitors. The 20 g (0.2 mol) of styrene monomer and 0.04 g (1.4×10^{-4} mol) of SDS were dispersed in 180 g of deionized water, and, then, 0.2 g (7.3×10^{-4} mol) of KPS was added under constant stirring and a N_2 atmosphere at 80°C for 4 h.

The 80 mL of the PS templates were diluted in 320 mL of deionized water to disperse the aniline monomer on the surface of the PS templates. Then, 1.2 mL (1.3×10^{-2} mol) of aniline and 0.12 mL (4.6×10^{-4} mol) of DVB were added into the PS emulsion and dispersed for 30 min in order to arrange the aniline monomer on the surfaces of the PS cores and to improve the stability of the resulting Pani shell. 1 M HCl and APS were added to the solution mixture, and the polymerization of Pani proceeded at room temperature for 24 h (aniline : APS = 1 : 1 (mol)). The thickness of the Pani shell was adjusted by varying the amount of added aniline monomer among volumes of 1.2, 2.4, 3.6, 4.8, and 6.0 mL, while 0.12, 0.24, 0.36, 0.48, and 0.60 mL of DVB was added, respectively. Therefore, the aniline monomer was added at ratios of 1, 2, 3, 4, and 5 times the base volume of 1.2 mL in the different experiments. Green PS/Pani composite spheres with a core-shell structure were produced and purified by centrifugation and dried in a vacuum oven at 60°C.

PS/Ppy with a core-shell structure was prepared similarly to the PS/Pani with a core-shell structure. 0.6 mL (8.47×10^{-3} mol) of pyrrole and 0.06 mL (2.3×10^{-4} mol) of DVB were added into the PS emulsion and dispersed for 30 min. Then, 4.5 g (1.6×10^{-2} mol) of $FeCl_3 \cdot 6H_2O$ was dispersed in 25 mL of deionized water. The $FeCl_3 \cdot 6H_2O$ solution and 1.97 g (8.5×10^{-3} mol) of APS were added to the solution mixture, and the polymerization of Ppy proceeded at room temperature for 24 h (pyrrole : APS = 1 : 1 (mol)). The thickness of the Ppy shell was varied by adjusting the amount of added pyrrole monomer among volumes of 0.6, 1.2, 1.8, and 2.4 mL, while 0.06, 0.12, 0.18, and 0.24 mL of DVB was added, respectively. Therefore, the pyrrole monomer was added at ratios of 1, 2, 3, and 4 times the base volume of 0.6 mL. Black PS/Ppy composite spheres were produced and purified by centrifugation and dried in a vacuum oven at 60°C.

To prepare the Pani and Ppy half hollow spheres, excess acetone was added to the dried PS/Pani and PS/Ppy core shells with different thicknesses at room temperature. The PS cores were dissolved in acetone to produce Pani and Ppy half hollow spheres over 48 h. The Pani and Ppy half hollow spheres were washed several times with deionized water to remove the initiator, unreacted monomer, and oligomer. Finally, Pani and Ppy half hollow spheres with different thicknesses were dried in a vacuum oven at 60°C. The full preparation processes of the Pani and Ppy half hollow spheres are schematically illustrated in Scheme 1.

The Pani and Ppy core shell and half hollow spheres with different shell thicknesses were analyzed by Fourier transform infrared spectroscopy (FT-IR) recorded on Varian 2000 in the range from 400 to 3,250 cm^{-1}. We used the pellet type using KBr powder for measuring. And the optical properties of prepared samples characterized through ultraviolet visible spectroscopy (UV-Vis, Varian Karry) in the range of 250–900 nm. The NMP (*N*-methyl pyrrolidinone) was used as solvent for Pani. The surface morphologies and shell thicknesses were observed by field emission scanning electron microscopy (FE-SEM, Zeiss Supra-40) with an

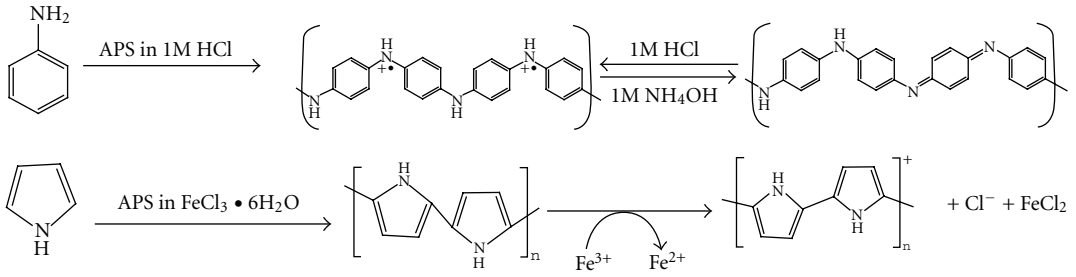

Scheme 1: The oxidation of aniline and pyrrole with ammonium persulfate in dopant solution for doping and dedoping.

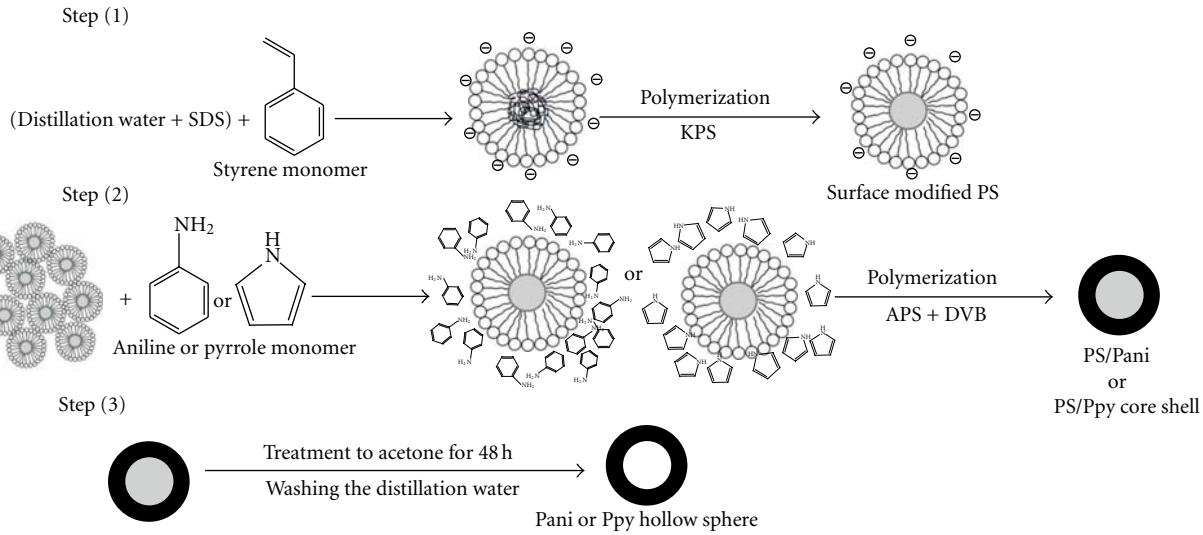

Scheme 2: Schematic illustration of the three-steps procedure used to produce Pani or Ppy half hollow spheres with different shell thicknesses.

accelerating voltage of 15 kV and field emission transmission electron microscopy (FE-TEM, JEM 2100F, JEOL operated at 200 kV).

3. Results and Discussion

The FT-IR spectra of the overall process materials are shown in Figure 1. Figure 1(a) shows the FT-IR spectra of PS, bulk Pani, and Pani half hollow spheres. The characteristic absorption bands due to the PS component are at around 1496, 1449, 754, and 696 cm^{-1}. The bands at 1,496 and 1,449 cm^{-1} are indicative of the C=C ring stretching and C–H stretching of PS, respectively [21]. The peaks of C=N and C=C stretching of quinoid and benzenoid rings are specific peaks of the bulk Pani. Similar FT-IR spectra to those shown in Figure 1(a) were observed for the bulk Pani and Pani half hollow spheres. The Pani half hollow spheres exhibited peaks at 1,580, 1,494, 1,302, 1,142, and 692 cm^{-1}. The peaks at 1,580 and 1,494 cm^{-1} indicated the C=N and C=C stretching mode of the quinoid and benzenoid rings of the Pani half hollow spheres, respectively. The peaks of at 1,302 and 1,142 cm^{-1} corresponded to C-N stretching (–N-benzenoid-N–) and C=N stretching (–N=quinoid=N–), respectively [22].

Figure 1(b) shows the FT-IR spectra of PS, bulk Ppy, and Ppy half hollow spheres with different thicknesses. Similar FT-IR spectra were observed for the bulk Ppy and Ppy half hollow spheres. The Ppy half hollow spheres shown in Figure 1(b) demonstrated peaks at 1,710, 1,157, 1,449, 1,371, 1,192, 1,046, 978, 753, and 698 cm^{-1}. The peak corresponding to oxygen dopant ($FeCl_3 \cdot 6H_2O$) occurred at 1,710 cm^{-1}, and the two peaks of 1,449 and 1,192 cm^{-1} corresponded to the C–N stretching. The peak observed at 1,557 cm^{-1} corresponded to the C–C stretching peak observed from the pyrrole ring. The peaks at 1,371 and 1,046 cm^{-1} correspond to the =C–H bond. The 918 cm^{-1} peak indicated the C–H bending. The regions of the C–H out-of-plane deformation vibration of the ring and the C–C out-of-plane ring deformation are indicated at 753 and 698 cm^{-1}, respectively [23]. However, the characteristic absorption peaks of PS still existed in Pani and Ppy half hollow spheres at 760–700 cm^{-1}. Therefore, we could guess that PS still remained in Pani and Ppy half hollow spheres.

Figures 2(a) and 2(b) show the UV-Vis spectra of the Pani half hollow spheres and Ppy half hollow spheres, respectively. The Pani half hollow spheres in Figure 2(a) show

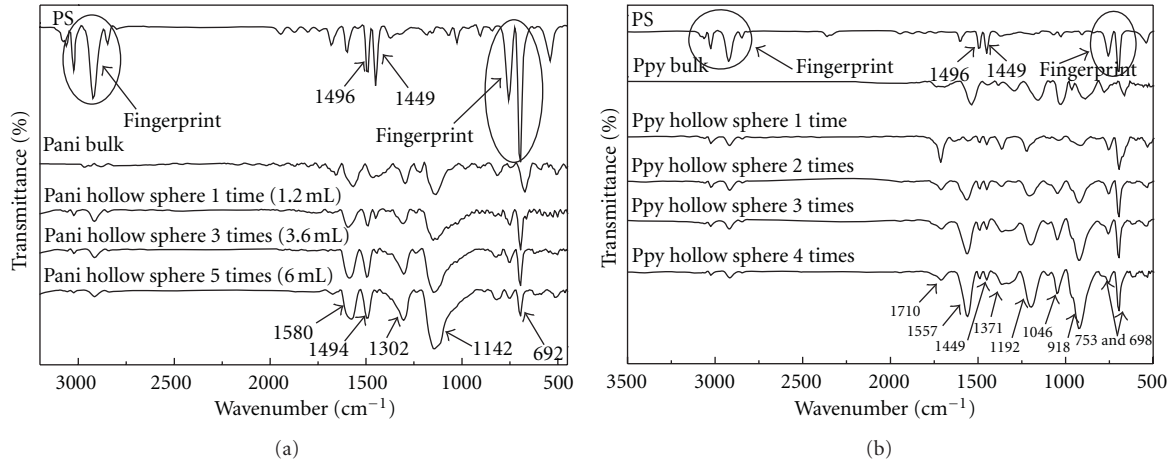

Figure 1: FT-IR spectra of (a) Pani half hollow spheres and (b) Ppy half hollow spheres with different thicknesses.

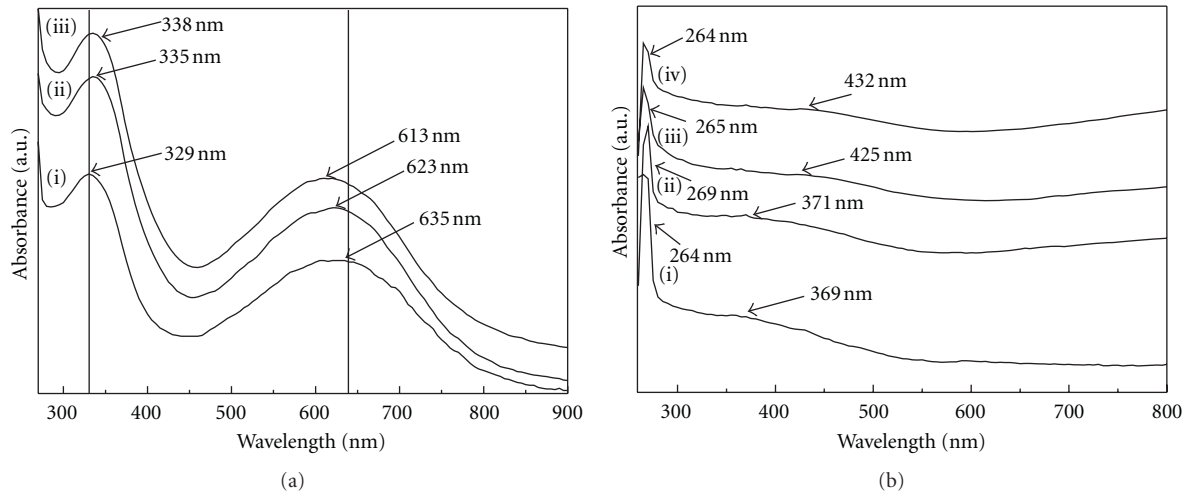

Figure 2: UV-Vis spectra of (a) Pani half hollow spheres produced with (i) 1.2, (ii) 3.6, and (iii) 6.0 mL of aniline and (b) Ppy half hollow spheres made with (i) 0.6, (ii) 1.2, (iii) 1.8, and (iv) 2.4 mL of pyrrole.

two characteristic absorption broad band peaks at around 330 and 620 nm. The peaks at 329, 335, and 338 nm can be ascribed to the π-π^* transition in the benzenoid rings, and the peaks at 635, 623, and 613 nm can be attributed to the polaron-polaron transition. As the amount of the aniline monomer was increased, the π-π^* transition red shifted and the polaron-polaron transition blue shifted.

The π-π^* transitions shown in Figure 2(a) were red shifted to longer wavelengths. Thus, the thicknesses of the Pani half hollow spheres were larger, and the π-π^* transition peaks appeared at 329, 335, and 338 nm. The red-shift is indicative of small changes of the chain geometry interring the torsion angle along the Pani backbone leading to mixing of the π and n orbital of the Pani chain and dopant. The red shifted transition of the π-π^* band gap indicates a reduction of the band gap, allowing the phenylene rings to adopt a more twisted geometry. As the thickness of the Pani hollow spheres increased, the polaron-polaron peaks were shifted to shorter wavelengths. The position of the shifted polaron-polaron peaks varied depending on the experimental conditions employed. The blue shifting was normally accompanied by the appearance and growth of a shoulder on the short wavelength side of the absorption band in the UV-Vis spectra (Figure 2(a)). The absorption of the polaron-polaron transition was observed at 635, 623, and 613 nm. This blue shift was dependent on the thickness. It has been proposed that direct interaction of planar benzenoid and quinoid chromophore groups rather than oxidation of the polymer chains is responsible for the blue-shifted exciton transition in Pani half hollow spheres with different thicknesses.

The Ppy half hollow spheres in Figure 2(b) show absorption peaks at 264, 269, 265, and 264 nm can be ascribed to the π-π^* transition in the aromatic ring, and the peaks at 369, 371, 425, and 432 nm can be attributed to the π-π^* transition.

The structures, morphologies, and diameter of particles were investigated by FE-SEM and FE-TEM. The FE-SEM images in Figure 3 show the successful formation of uniform

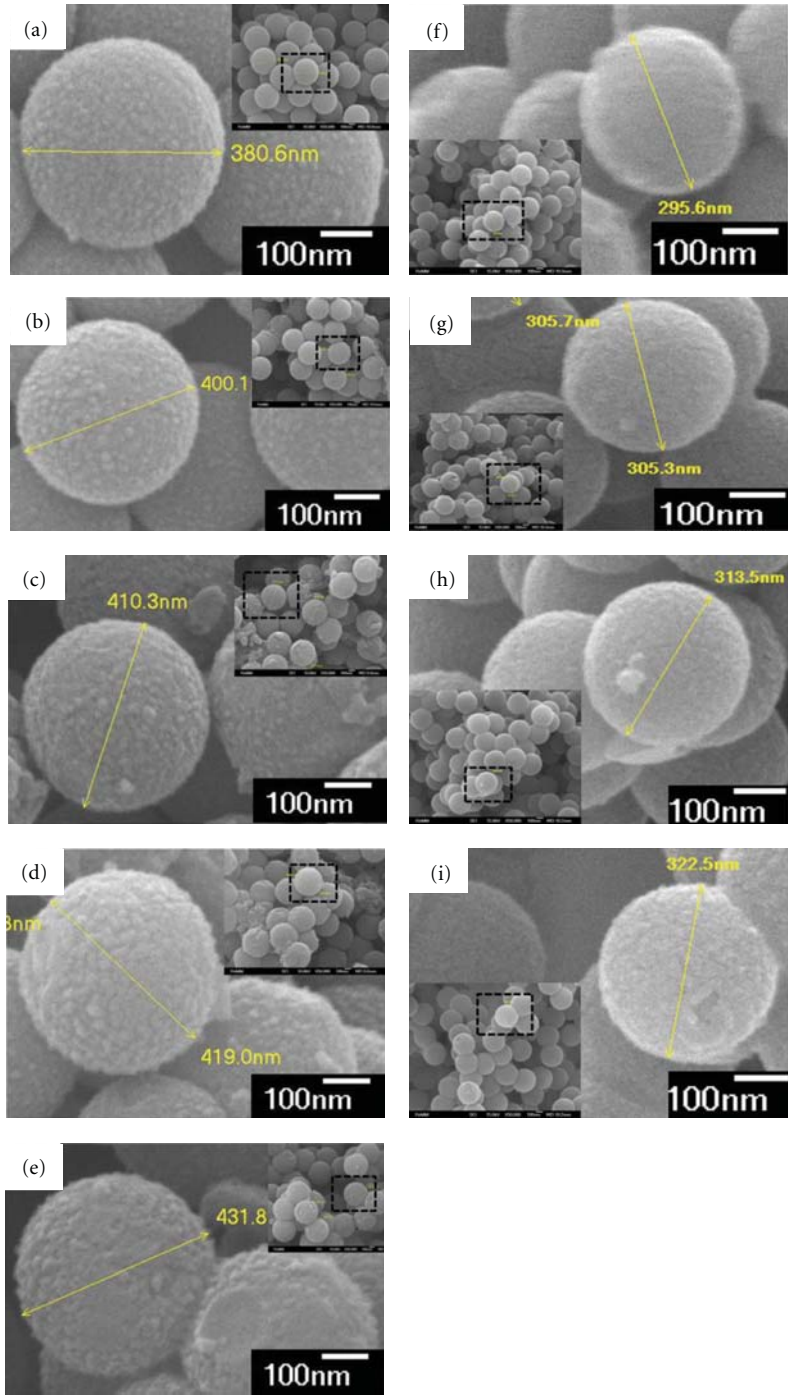

Figure 3: FE-SEM images of the PS/Pani core shell produced with (a) 1.2, (b) 2.4, (c) 3.6, (d) 4.8, and (e) 6.0 mL of aniline and the PS/Ppy core shell made with (f) 0.6, (g) 1.2, (h) 1.8, and (i) 2.4 mL of pyrrole.

Pani shells on PS cores (Figures 3(a), 3(b), 3(c), 3(d), and 3(e)) and Ppy shells on PS cores (Figures 3(f), 3(g), 3(h), and 3(i)). In the experiments, we used PS cores with the same diameter. These images reveal that the PS/Pani and PS/Ppy core shells have a rough surface. The diameters of the PS/Pani core shell in Figures 3(a), 3(b), 3(c), 3(d), and 3(e) were measured to be 380.6, 400.1, 410.3, 419.0, and 431.8 nm, respectively. The diameters of the PS/Ppy core shell in Figures 3(f), 3(g), 3(h), and 3(i) were 295.6, 305.3, 313.5, and 322.5 nm, respectively. As the amount of the monomer increased, the shell diameters of PS/Pani and PS/Ppy also increased.

The structure and thickness of the Pani half hollow spheres were investigated by FE-SEM and FE-TEM. FE-SEM and FE-TEM images of the Pani half hollow spheres and Ppy half hollow spheres after removal of the PS core are

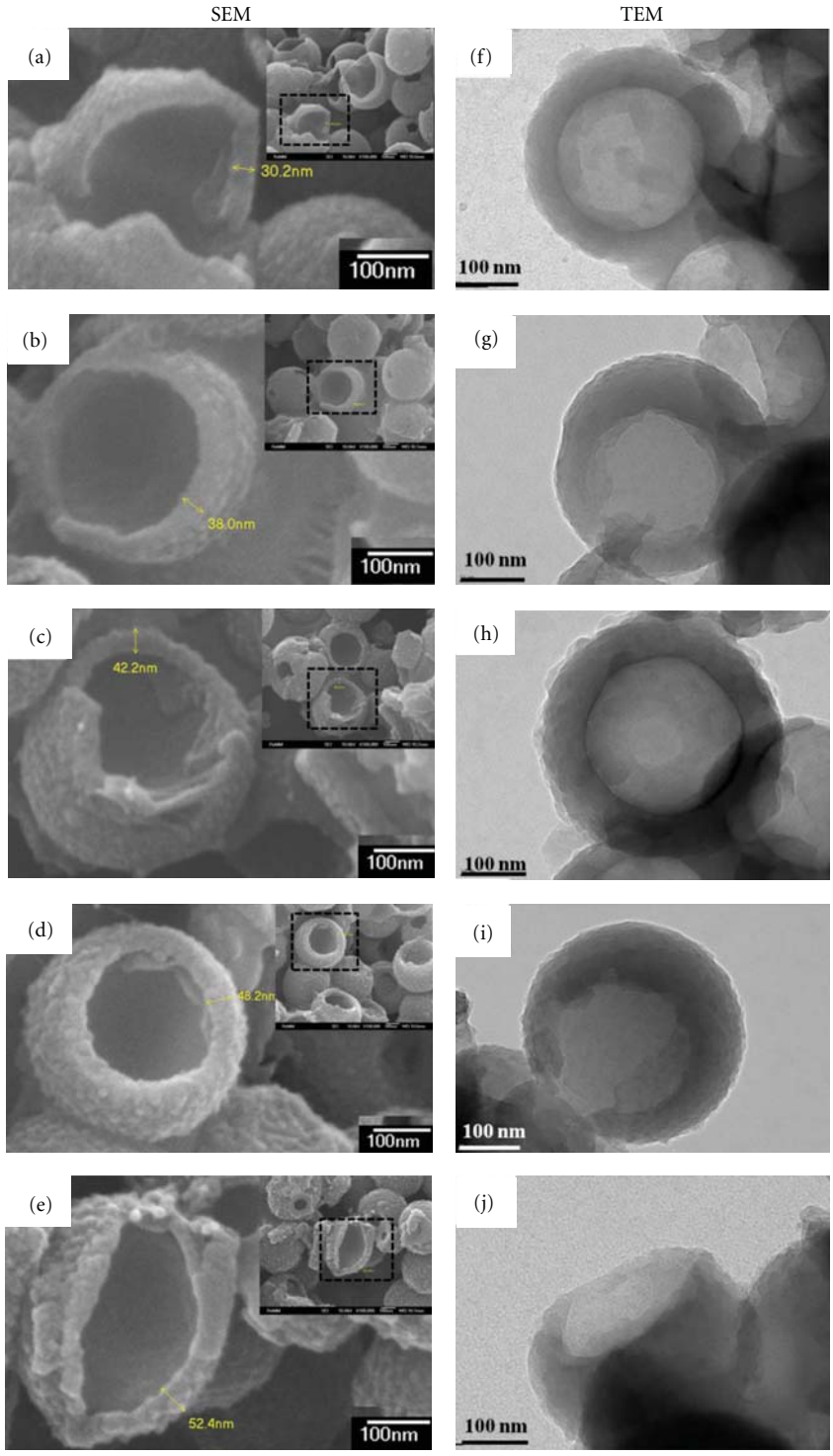

Figure 4: FE-SEM and FE-TEM images of Pani half hollow spheres made with (a, f) 1.2, (b, g) 2.4, (c, h) 3.6, (d, i) 4.8, and (e, j) 6.0 mL of aniline.

shown in Figures 4 and 5, respectively. Therefore, the half hollow spheres had vacancies, as observed in the FE-TEM image. When the PS was treated with acetone, the acetone permeated the shell (Pani or Ppy) and melted the PS. Next, the melted PS got out of the shell. At this time, the melted PS got out from the part of weak or thin shell. After enough time had passed, the entrance was enlarged.

The thickness of the half hollow spheres was investigated by FE-SEM. The FE-SEM images of the Pani half hollow spheres (Figures 4(a), 4(b), 4(c), 4(d), and 4(e)) and Ppy

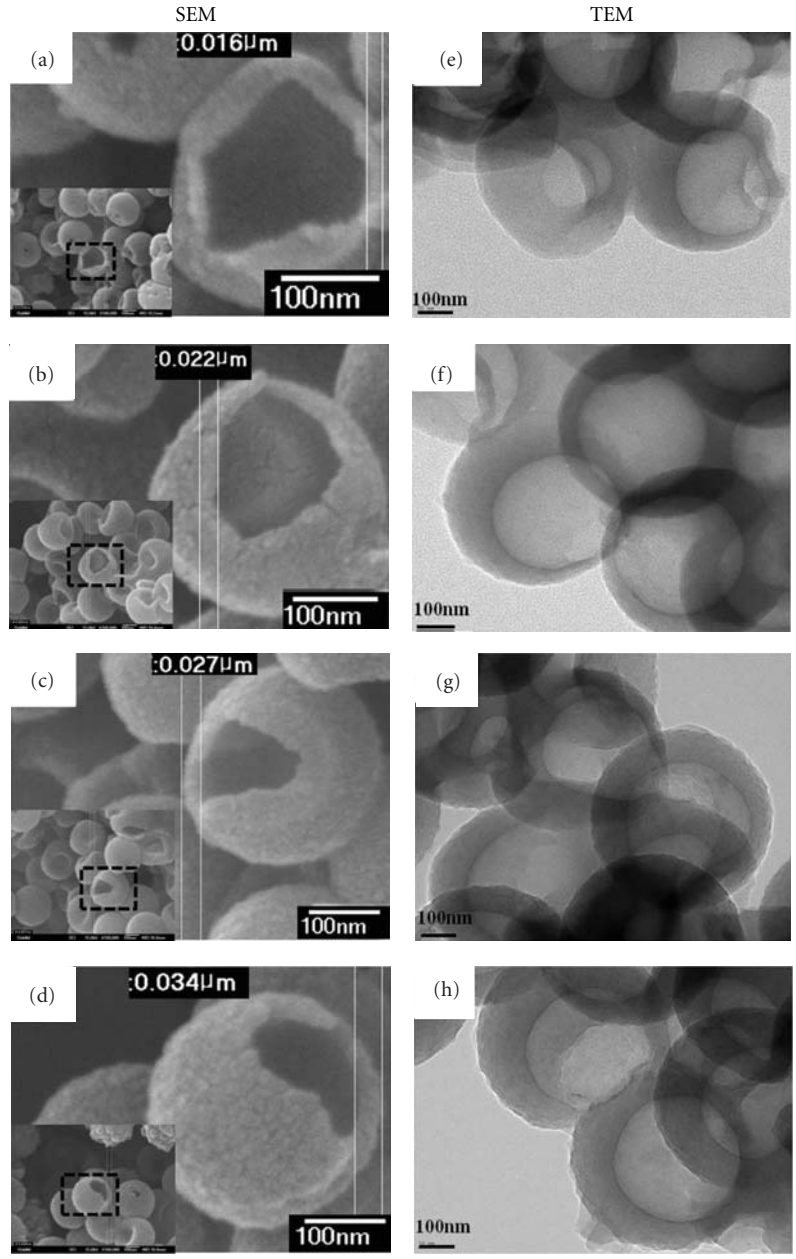

Figure 5: FE-SEM and FE-TEM images of Ppy half hollow spheres produced with (a, e) 0.6, (b, f) 1.2, (c, g) 1.8, and (d, h) 2.4 mL of pyrrole.

half hollow spheres (Figures 5(a), 5(b), 5(c), and 5(d)) demonstrated different thicknesses. The thicknesses of the Pani half hollow spheres (Figures 4(a), 4(b), 4(c), 4(d), and 4(e)) were 30.2, 38.0, 42.2, 48.2, and 52.4 nm, respectively. The thicknesses of the Ppy half hollow spheres (Figures 5(a), 5(b), 5(c), and 5(d)) were 16.0, 22.0, 27.0, and 34.0 nm, respectively.

Figures 6(a) and 6(b) show the shell thicknesses of the Pani half hollow spheres and Ppy half hollow spheres as a function of the amount of monomer. The shell thickness linearly increased with increasing amount of monomer. From these results, it is possible to control the shell thickness of the Pani and Ppy half hollow spheres by adjusting the amount of aniline or pyrrole monomer. Therefore, it is able to control the desired shell thickness of the Pani and Ppy half hollow sphere in these ranges. As demonstrated in the results shown in Figures 6(a) and 6(b), it is simple to obtain Pani and Ppy half hollow spheres with specific shell thicknesses.

4. Conclusions

Pani and Ppy half hollow spheres with a controlled thickness were successfully synthesized by three steps using the PS core with micelle assistance. The PS was polymerized by emulsion polymerization using an anionic surfactant with

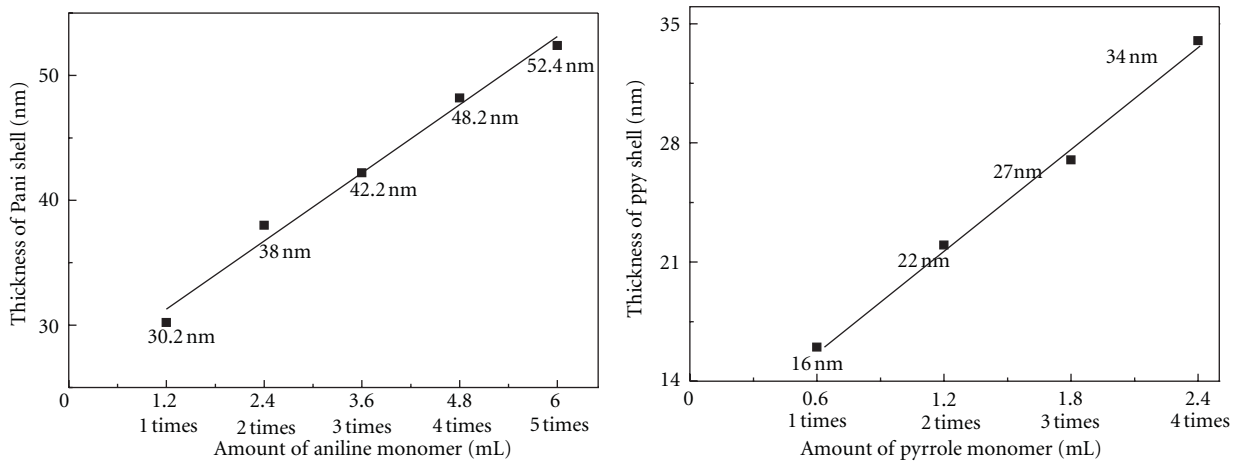

Figure 6: The shell thicknesses of the (a) Pani half hollow spheres and (b) Ppy half hollow spheres as a function of the amount of added monomer.

SDS for surface modification. Aniline and pyrrole were polymerized by an oxidizing agent on the PS core surfaces. The shell thickness of the Pani and Ppy was controlled by adjusting the amount of aniline and pyrrole monomer, respectively. In separate experiments, aniline monomer was added at volumes of 1.2, 2.4, 3.6, 4.8, and 6.0 mL, and pyrrole monomer was added at volumes of 0.6, 1.2, 1.8, and 2.4 mL. Finally, the PS was dissolved in acetone to create Pani and Ppy half hollow spheres. The shell thicknesses of the Pani and Ppy in the half hollow sphere structure were 30.2, 38.0, 42.2, 48.2, and 52.4 nm and 16.0, 22.0, 27.0, and 34.0 nm, respectively. The shell thickness of the Pani and Ppy was proportional to the amount of aniline and pyrrole monomer. Therefore, it is possible to control the desired shell thickness of the Pani and Ppy half hollow spheres in these ranges.

Acknowledgments

This research was supported by a grant from the Fundamental R&D Program for Core Technology of Materials funded by the Ministry of Knowledge Economy, Republic of Korea.

References

[1] J. Lei, V. P. Menon, and C. R. Martin, "Chemical preparation of conductive polypyrrole–polytetrafluoroethene composites," *Polymers for Advanced Technologies*, vol. 4, no. 2-3, pp. 124–132, 1994.

[2] Y. Yang and M. Wan, "Chiral nanotubes of polyaniline synthesized by a template-free method," *Journal of Materials Chemistry*, vol. 12, no. 4, pp. 897–901, 2002.

[3] Z. Chen, Y. Takei, B. A. Deore, and T. Nagaoka, "Enantioselective uptake of amino acid with overoxidized polypyrrole colloid templated with L-lactate," *Analyst*, vol. 125, no. 12, pp. 2249–2254, 2000.

[4] J. Chen, A. K. Burrell, G. E. Collis et al., "Preparation, characterisation and biosensor application of conducting polymers based on ferrocene substituted thiophene and terthiophene," *Electrochimica Acta*, vol. 47, no. 17, pp. 2715–2724, 2002.

[5] J. Chen, C. O. Too, G. G. Wallace, G. F. Swiegers, B. W. Skelton, and A. H. White, "Redox-active conducting polymers incorporating ferrocenes. Preparation, characterization and bio-sensing properties of ferrocenylpropyl and butyl polypyrroles," *Electrochimica Acta*, vol. 47, no. 26, pp. 4227–4238, 2002.

[6] J. Chen, J. Huang, G. F. Swiegers, C. O. Too, and G. G. Wallace, "A readily-prepared electrocatalytic coating that is more active than platinum for hydrogen generation in 1 M strong acid," *Chemical Communications*, vol. 10, no. 3, pp. 308–309, 2004.

[7] O. D. Velev, T. A. Jede, R. F. Lobo, and A. M. Lenhoff, "Porous silica via colloidal crystallization," *Nature*, vol. 389, no. 6650, pp. 447–448, 1997.

[8] B. T. Holland, C. F. Blanford, and A. Stein, "Synthesis of macroporous minerals with highly ordered three-dimensional arrays of spheroidal voids," *Science*, vol. 281, no. 5376, pp. 538–540, 1998.

[9] F. Caruso, R. A. Caruso, and H. Möhwald, "Nanoengineering of inorganic and hybrid hollow spheres by colloidal templating," *Science*, vol. 282, no. 5391, pp. 1111–1114, 1998.

[10] W. Schärtl, "Crosslinked spherical nanoparticles with core–shell topology," *Advanced Materials*, vol. 12, no. 24, pp. 1899–1908, 2000.

[11] F. Caruso, "Nanoengineering of particle surfaces," *Advanced Materials*, vol. 13, no. 1, pp. 11–22, 2001.

[12] Y. Zhang, Z. Huang, F. Tang, and J. Ren, "Ferrite hollow spheres with tunable magnetic properties," *Thin Solid Films*, vol. 515, no. 4, pp. 2555–2561, 2006.

[13] W. Zhao, H. Chen, Y. Li, A. Li, M. Lang, and J. Shi, "Uniform rattle-type hollow magnetic mesoporous spheres as drug delivery carriers and their sustained-release property," *Advanced Functional Materials*, vol. 18, no. 18, pp. 2780–2788, 2008.

[14] M. K. Park, K. Onishi, J. Locklin, F. Caruso, and R. C. Advincula, "Self-assembly and characterization of polyaniline and sulfonated polystyrene multilayer-coated colloidal particles and hollow shells," *Langmuir*, vol. 19, no. 20, pp. 8550–8554, 2003.

[15] Z. Niu, Z. Yang, Z. Hu, Y. Lu, and C. C. Han, "Polyaniline-silica composite conductive capsules and hollow spheres," *Advanced Functional Materials*, vol. 13, no. 12, pp. 949–954, 2003.

[16] Z. Wei and M. Wan, "Hollow microspheres of polyaniline synthesized with an aniline emulsion template," *Advanced Materials*, vol. 14, no. 18, pp. 1314–1317, 2002.

[17] L. Zhang and M. Wan, "Self-assembly of polyaniline from nanotubes to hollow microspheres," *Advanced Functional Materials*, vol. 13, no. 10, pp. 815–820, 2003.

[18] K. Huang, X. H. Meng, and M. Wan, "Polyaniline hollow microspheres constructed with their own self-assembled nanofibers," *Journal of Applied Polymer Science*, vol. 100, no. 4, pp. 3050–3054, 2006.

[19] Z. Yang, Z. Niu, Y. Lu, Z. Hu, and C. C. Han, "Templated synthesis of inorganic hollow spheres with a tunable cavity size onto core-shell gel particles," *Angewandte Chemie*, vol. 42, no. 17, pp. 1943–1945, 2003.

[20] X. Wang, J. Liu, X. Feng, M. Guo, and D. Sun, "Fabrication of hollow Fe_3O_4-polyaniline spheres with sulfonated polystyrene templates," *Materials Chemistry and Physics*, vol. 112, no. 2, pp. 319–321, 2008.

[21] X. Zhu, M. Elomaa, F. Sundholm, and C. H. Lochmüller, "Infrared and thermogravimetric studies of thermal degradation of polystyrene in the presence of ammonium sulfate," *Polymer Degradation and Stability*, vol. 62, no. 3, pp. 487–494, 1998.

[22] N. S. Sariciftci, H. Kuzmany, H. Neugebauer, and A. Neckel, "Structural and electronic transitions in polyaniline: a Fourier transform infrared spectroscopic study," *The Journal of Chemical Physics*, vol. 92, no. 7, pp. 4530–4539, 1990.

[23] R. G. Davidson and T. G. Turner, "An IR spectroscopic study of the electrochemical reduction of polypyrrole doped with dodecylsulfate anion," *Synthetic Metals*, vol. 72, no. 2, pp. 121–128, 1995.

Hindawi Publishing Corporation
Journal of Nanomaterials
Volume 2012, Article ID 319398, 7 pages
doi:10.1155/2012/319398

Research Article

Optical Properties of Polystyrene-ZnO Nanocomposite Scattering Layer to Improve Light Extraction in Organic Light-Emitting Diode

G. Nenna, A. De Girolamo Del Mauro, E. Massera, A. Bruno, T. Fasolino, and C. Minarini

Italian National Agency for New Technologies, Energy and Sustainable Economic Development (ENEA), Portici Research Centre, Piazzale E. Fermi 1, 80055 Portici, Italy

Correspondence should be addressed to A. De Girolamo Del Mauro, anna.degirolamo@enea.it

Received 10 March 2012; Accepted 11 May 2012

Academic Editor: Marcio Rodrigo Loos

In this work, experimental measurements on polystyrene-ZnO nanocomposite scattering films and on organic light-emitting device with and without the scattering layers are presented. The results are also compared with Henyey-Greenstein radiative-transfer model to narrow down the parameters that can be important in the identification of more suitable scattering layers. As a result, an increase of efficiency of about 30% has been obtained that it can be translated in 60% of outcoupled light in respect to the total generated amount.

1. Introduction

Brightness and efficiency are extremely important factors for the employment of organic light-emitting diodes (OLEDs) in lighting and displays application in the competition against more standard technologies. For this reason, extracting the wave-guided light trapped within OLED and more in general within electroluminescent flat multilayer device structure is one of the main driving forces to improve the device efficiency. Several strategies were developed concerning the surface modification to increase the efficiency factor by using ordered microlenses, Bragg reflectors, 2D photonic crystal, or modifying the cavity effects [1–4]. In all these high-tech applications, there is not only an improvement in the light extraction but also a substantial modification in angular device light intensity and/or spectrum [2–4]. Another approach can be played by a more unsophisticated structure simply performing polymer matrix by spin coating or casting processes introducing scattering centres consisting of nanoparticles that locally change the refractive index [5–11]. Following the last approach, in many papers [5, 6, 11], the analysis of volumetric scattering layers has been addressed to determine the right optical parameters (reflectance, transmittance, and scattering properties) and make them suitable for the employment in OLED light out-coupling purposes. In this paper, we will depict the advantages of polystyrene-zinc oxide (PS/ZnO) nanocomposites as volumetric light scattering layers in OLED lighting applications. We tried to obtain the out-coupling enhancements already reported in the literature by means of thinner scattering films. In our approach, we focused on high concentrations of nanoparticles in polymeric films to increase the probability of the scattering event between small refracting index differences in mediums. To accomplish this task, we adopted ZnO dispersions in PS films which are already reported in some works where several PS/ZnO nanocomposites have been investigated considering other kinds of effects of nanoscale ZnO on the electrical and physical characteristics of PS nanocomposites [12, 13].

2. Layers and Device Preparation

PS (average Mw ~192,000) and ZnO nanopowders (average size <100 nm) are commercially available products from Aldrich. Chlorobenzene (Cl-benz) was selected as a cosolvent of PS and ZnO. PS/ZnO nanocomposite layers with varying concentrations of ZnO were prepared by solution-mixing

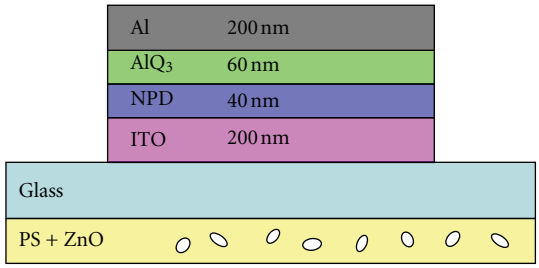

Figure 1: (Colour online) The device structure considered in this work.

technique. PS was dissolved in Cl-benz at 90°C for 30min with vigorous stirring at concentration of 15 wt%. ZnO was dispersed in this solution by ultrasonic vibration for 10 min. ZnO contents were 10 and 20% based on the polymer matrix. To obtain a nanocomposite layer, the suspensions PS/ZnO were spin coated (with 500 rpm for 30 sec) onto glass side of the indium-doped-tin-oxide- (ITO-) coated "float glass" substrates, purchased from Delta Technology. These substrates are provided with a passivation layer of about 300 Å of SiO_2 between the glass and a 120 nm to 160 nm thick ITO layer having a sheet resistance (R_s) from 8 to 12 Ohm/square. The optical parameters for the substrates and the ITO layer were specified by supplier [14]. Nominal refractive index was 1.517 for the float glass substrate and $n = 1.775$ and $k = 0.012$ for ITO. Substrate thickness was 1.1 mm and declared optical transmittance greater than 83%. The substrates were cleaned by sonication in deionised water and detergent and dried in oven at 115°C for 2 hours. In this study, a basic double-layer OLED configuration was fabricated with a 40 nm thick N,N′-di-1-naphthaleyl-N,N′-diphenyl-1,1′-biphenyl-4,4′-diamine (NPD) film as HTL (hole transport layer) and a 60 nm thick tris-8-hydroxyquinoline aluminium salt (Alq_3) film as ETL (electron transport layer), see Figure 1. Active layers of our OLEDs were deposited on ITO-patterned anodes.

In this configuration, Alq_3 is both ETL and emissive layer (EML). An Aluminium (Al) cathode was finally evaporated to complete the device structure. The anodic structures were patterned through inverse photolithography and HCl-based solution etching. From the ITO side, the organic layers were thermally evaporated sequentially with no vacuum breaking between their depositions. The pressure in deposition chamber was kept always between 10^{-6} and 10^{-7} mbar, and the growth rate for the organic layers was between $1 \div 2$ A/s. The Al cathode was evaporated through shadow mask, with growth rate of about $2 \div 3$ A/s determining a circular active area having a diameter of 4 mm.

For this work, we have fabricated six different series of devices as reported in Table 1. PS/ZnO films at different thickness are obtained by depositing several layers of dispersion.

2.1. Measurements. The films thicknesses have been evaluated by a KLA Tencor P-10 Surface Profiler. We realized two scattering films on quartz substrate with similar thickness and different ZnO concentration to evaluate their optical performances. These are the same conditions as the devices C and F (see Table 1).

Table 1: Thickness and ZnO concentrations in the PS/ZnO nanocomposite layers.

Device	Thickness of scattering layer (μm)	ZnO (wt%)
A	No layer	0
B	4.6	0
C	5.1	10
D	8.3	10
E	12.1	10
F	5.3	20

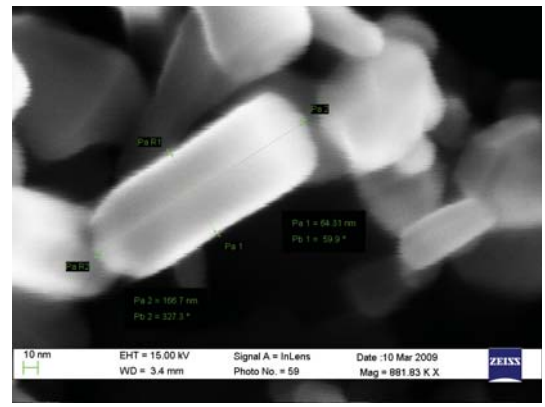

Figure 2: SEM image of ZnO nanoparticles deposited on a silicon substrate.

Transmittance spectra have been measured with a Perkin_Elmer lambda 900 spectrophotometer.

The scanning electron microscopy (SEM) images were performed by means of an LEO 1530 microscope at a magnification rate of 883 KX. The current-voltage (I–V) measurements on OLED devices were performed by a Keithley 2400 Power Supply Source-Meter in voltage mode, with constant increment steps and delay time of 1 s before each measurement point. For the electroluminescence (EL) analysis, a calibrated integrating sphere, with a circular open window of about 1 cm diameter where the devices are accommodate, and a photodiode (Newport 810UV) connected to a Keithley 6517A Electrometer were employed. The Newport 810UV photodiode was used also to perform angular measurements.

3. Experimental Results

Different optical measurements were performed on scattering films with different nanoparticles concentrations before testing them coupled with OLEDs. These measurements were very important in order to investigate the effects of light scattering before the realization of a complete device.

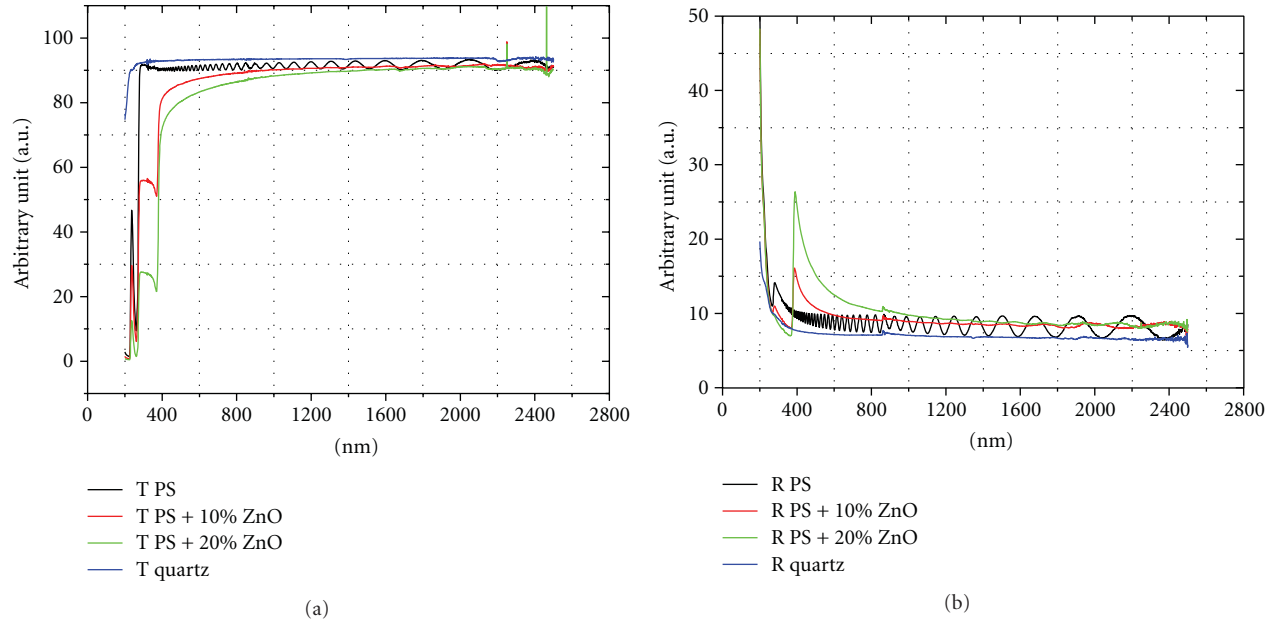

FIGURE 3: (Colour online) Transmittance (T) (a) and reflectance (R) (b) spectra related to the free standing quartz substrate, to the PS film, and to two nanocomposites with 10 wt% and 20 wt% of ZnO.

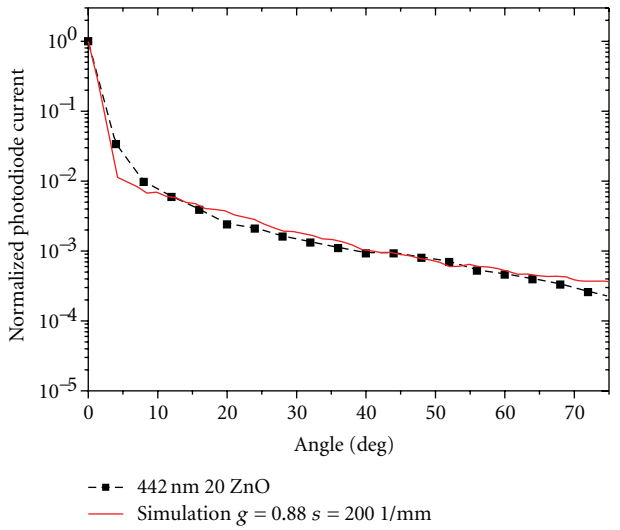

FIGURE 4: (Colour online) The angularly resolved normalized intensity versus angle for the scattering film performed on a quartz substrate with the presence of 20% of nanoparticles (black square). The simulated data were obtained with $g \sim 0.88$ and $s \sim 200$ 1/mm (red line).

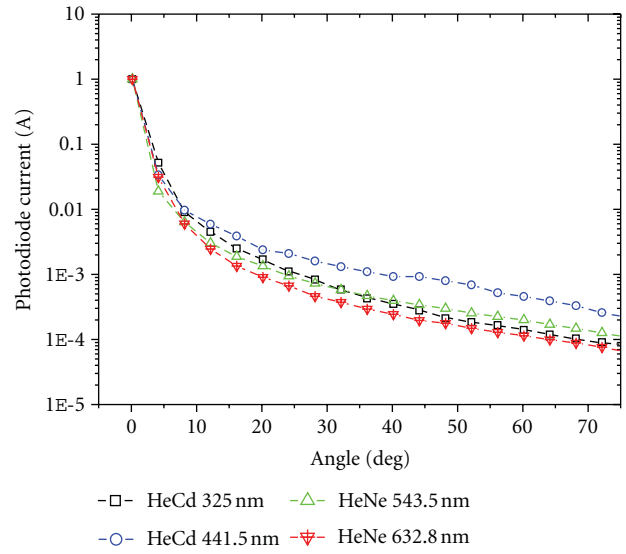

FIGURE 5: (Colour online) The angularly resolved normalized intensity versus angle for the scattering film performed on a quartz substrate with the presence of 20% of nanoparticles at different wavelengths.

3.1. Scattering Film Characterization. ZnO nanoparticles were characterized by SEM imaging to analyze shapes and sizes (Figure 2). From those images, we can see that the nanoparticles are not spherical, and they are much more similar to nanorods with the long axis around 200 nm or smaller.

Figure 3 reports transmittance and reflection spectra of the scattering films. From these measurements is possible to observe that these films show no appreciable absorption in the visible range. Furthermore, the two ZnO dispersion percentages (namely 10 wt% and 20 wt%) are easy to resolve and discriminate.

For both PS/ZnO films, a decrease in transmittance and a relative increase in the reflectance in the wavelength range 400 nm–800 nm are observed, following the refractive index variation in the same spectral range for the ZnO nanoparticles [15, 16]. The pure PS layer without

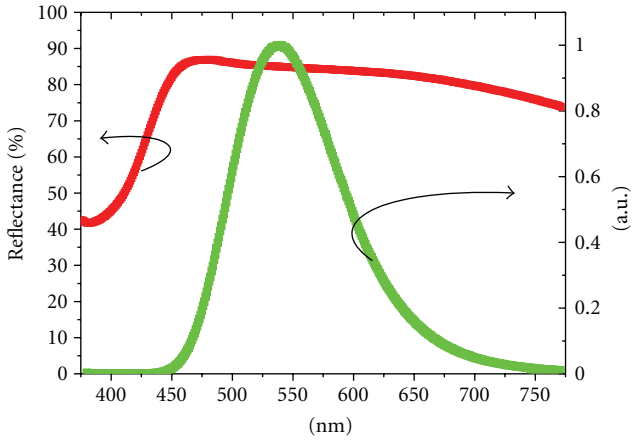

Figure 6: (Colour online) Measured cathode reflectivity from the glass side through the OLED device (red line) and the normalized spectra measured from our devices (green line).

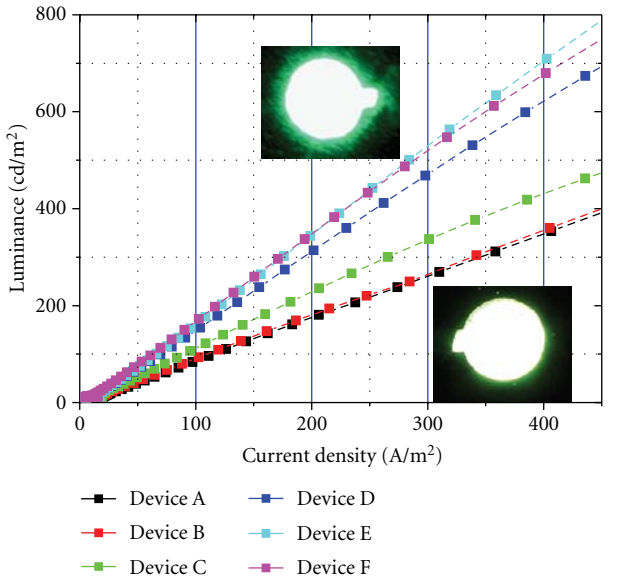

Figure 7: (Colour online) Luminance versus current density of all the OLED devices realized reported in a log-log plot. In the inset, two devices are reported drove with the same current (1 mA) with (up) and without (down) ZnO nanoparticles inside the PS polymer matrix.

nanoparticles shows a very high transmission (higher than 90%) almost over the all investigated range from 2500 nm to 250 nm. From Figure 3, we can also observe the interference effects inside the film. We utilized these effects to evaluate the refractive index [17–19] that we have estimated to be approximately around $n = 1,58$ for the PS. The interference effect is broken by the presence of nanoparticles and the consequent scattering mechanism for the PS/ZnO layers. The interference observed for the pure PS is broken in the films where ZnO nanoparticles have been dispersed, and on these films, the main process is scattering inside the films.

We have realized angularly resolved scattering measurements with the aim to describe the ellipsoidal profile determined by the light coming out from the sample when perpendicularly irradiated by a laser light (HeCd λ = 442 nm).

These kinds of measurements are particularly interesting for the determination of scattering parameters as previously reported in the diagnostic of different materials (e.g., roughness surfaces, biological tissues). In Figure 4, the results from the angularly resolved intensity for the PS/ZnO nanocomposites with 20 wt% of ZnO are shown.

Figure 4 reports together with the experimental data also the results of a simulation that has been performed. Using Mie theory approach [20], the intensity of the scattered light as function of the angle is a quite complex function, so we have simplified our analysis by using two parameters functions: one angular and another spatial. The total intensity in presence of scattered light can be written as function of the detection angle (θ) and the optical pathway inside the film (x) with total thickness L:

$$I_t(\theta, x) = I_0 \int_0^{180} p(\theta) d(\vartheta) * \int_0^L P(x) dx, \tag{1}$$

where I_0 and I_t are, respectively, the incident light intensity and the transmitted light intensity. The first function is the Henyey and Greenstein function [21] due to the difference in the refractive index between matrix and particles, and the second is the scatterance due to the mean free path from a scattering event to another.

The Henyey-Greenstein scattering distribution function can be written as:

$$p(\theta) = \frac{1 - g^2}{4\pi (1 + g^2 - 2g \cos\theta)^{3/2}}, \tag{2}$$

where g parameter is the anisotropy factor of the scattering layer and gives rise to the shape of the output profile as a response to an incident light beam.

Furthermore, when a ray enters in the scattering film, it will be propagated with a random distance x and with a distribution of probability

$$P(x) = e^{-sx} dx, \tag{3}$$

where the s parameter is the scattering coefficient [5, 6]. Or on other words, s is the average distance between two centres of scattering. The value $P(x)$ needs to be integrated trough all the film thickness to take into account the contribution of all the scattering centers.

The data have been fitted using g and s as free parameters. As a result, the g parameter (0.88) results to be slightly higher than literature results [5, 6], but this can be easily explained considering the little refractive index difference between the polymer matrix ($n \sim 1.58$) and the particles (from 1.9 to 2.1) [20]. Furthermore, nanoparticle shape can induce an increase in the g parameter [22] if compared to the one obtained by perfectly spherical nanoparticles.

With an anisotropy factor around 0.9 as discussed in paper [11], we obtained a very broad optimum zone leading to an enhancement of OLED light output as a function of scatterance with a consequent easier way to reach the optimum of behaviour.

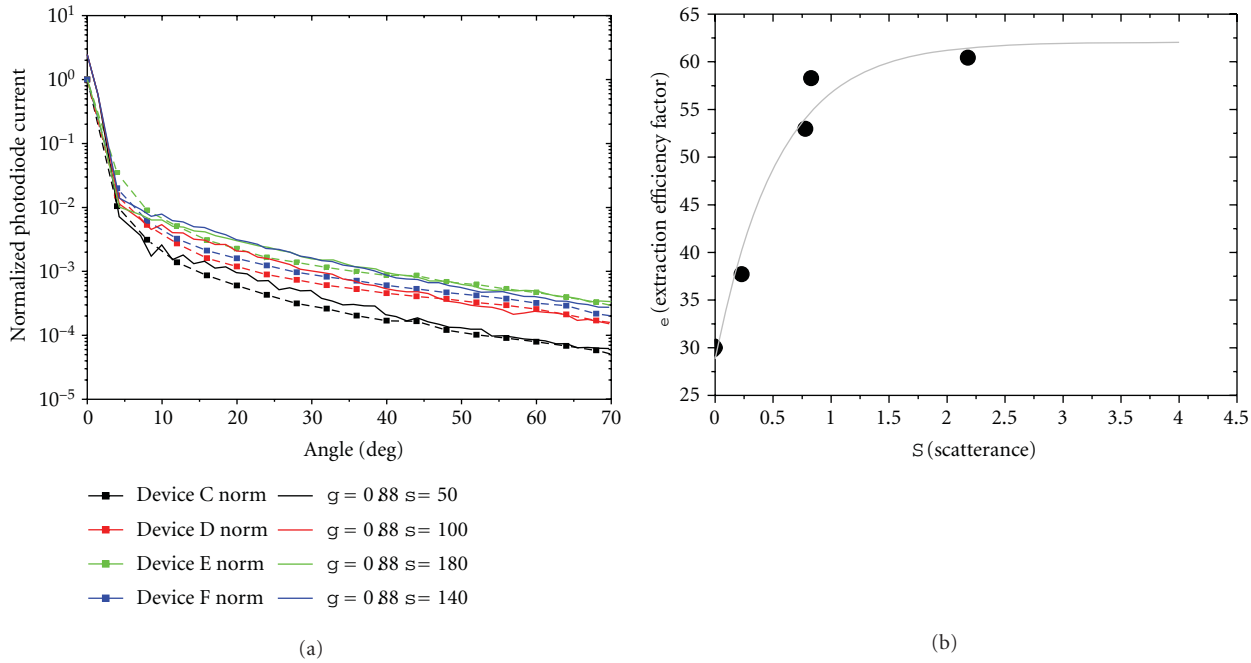

Figure 8: (Colour online) The angularly resolved normalized intensity versus angle for the scattering film performed on glass substrates and the related simulation (a). Extraction coefficient factor versus scatterance (black circle) and asymptotic simulated data (grey line) (b).

The higher value of the refractive index of the matrix ($n \sim 1.58$) in respect to the glass substrate ($n \sim 1.52$) induces a good compromise between the light confinement effect of light and the outcoupling of light [23]. These results suggest the possibility that the light could easily pass from the glass to the scattering layer.

Figure 5 shows the angular distribution of the scattering intensity for different excitation wavelengths from the UV to the red. It is clear that the scattering intensity at wider angles decreases going from the visible to the red due to the variation of the ZnO refractive index.

For the UV region, the behaviour is completely different; in fact the dynamic is faster as function of the angle, because the matrix has a higher absorption (see Figure 3).

3.2. Device Characterization. In presence of light-scattering form, a layer of the device one of the most critical parameters in the determination of light extraction is the effective cathode reflectivity. In Figure 6, the cathode reflectivity related to our stacked device in the same range of wavelength of the OLED spectra is showed. In the chosen spectral range, the reflectivity values are always higher than 80%, this is a good compromise for the aims of our investigation [5, 11].

As reported in Table 1, scattering films were realized with different particles concentrations and different thickness, and their effect on light outcoupling on the associated OLED efficiency was evaluated realizing six different devices.

The total internal reflection and the relative trapped light on device A was performed introducing the device inside to an integrating sphere and then mounting the same device outside in front of the optical window as previously described. As expected, only the 30% of light is able to go through the glass substrate [24]; thus, the trapped light amount is around 70%, and it is completely loss. Now we are able to evaluate correctly the efficiency improvement of our devices simply performing the measurement on the other devices taking into account the reflectivity of Figure 6 where it is shown the luminance behaviour versus the devices current density.

Figure 7 reports the luminance as function of the current density for the six devices realized. It is possible to note an improvement of efficiency both increasing the ZnO wt% and the thickness of scattering layer. In particular, a maximum enhancement of luminance of about 2 times is observed for devices E and F that can be translated in a 30% of luminance improvement in respect to the outcoupled light and in a 60% improvement for the in light that can be utilized respect to the totally generated.

From the inset of Figure 7, we can observe two images related to two devices drove at the same current (1 mA) with and without ZnO nanoparticles inside the PS polymer matrix. The active area of the device with the scattering layer seems to optically increase, because the light is not only scattered but also guided, but it is clear that we have an increase in the OLED efficiency too.

These results indicate also a saturation behaviour for the device efficiency in respect to the scattering layer thickness as expected. In fact, it is due to the optical parameters of our PS/ZnO nanocomposite blends and in particular to the g parameter value. In particular, in agreement with previous studies, we found a peak of efficiency at scatterance value of around 2.5 and a shift of the peak itself to high scatterance values due to high g values [5].

To this regard, in Figure 8(a), the angularly resolved normalized intensity versus angle for the scattering film is presented. These results demonstrate, once again, that our films have no relevant absorption (see Figures 3 and 5 for comparison), and so it is not critical if the peak for the outcoupling efficiency is achieved by changing the nanoparticle concentration, or through adjusting the free mean path in the film by increasing the thickness as it is possible to observe in Figure 8(b). In particular, in Figure 8(b), it is reported the total scatterance (S), calculated from the scattering coefficient reported in the legend of Figure 8(a) and the layer thicknesses reported in Table 1, versus the extraction efficiency factor (η_e), found keeping in mind that without scattering layer, it is nearly 0.3 [24, 25] using the Lambertian distribution and evaluating the difference in the devices luminance fixing the current density at 400 (A/m^2).

4. Conclusions

Optical permanents of different kinds of polystyrene-ZnO nanocomposites have been studied. The application of such composites as scattering film in lighting application has been also evaluated. The optical parameters have been investigated, and an anisotropy factor around 0.88 was found.

As expected, we have found that increasing the thickness or the percentage in weight of ZnO nanoparticles leads to an improvement of device efficiency. In particular, with a thickness of around 12 μm and 10 wt% of ZnO nanoparticles, it is possible to reach an extraction efficiency factor around 0.6 with a considerable improvement in the light emission.

In conclusion, we have utilized a radiative-transport analysis to develop a simple light extraction system that can be suitable in OLED lighting applications, while it must be carefully used for displays application because the device active area seems to increase.

References

[1] S. Möller and S. R. Forrest, "Improved light out-coupling in organic light emitting diodes employing ordered microlens arrays," *Journal of Applied Physics*, vol. 91, no. 5, pp. 3324–3327, 2002.

[2] J. M. Lupton, B. J. Matterson, I. D. W. Samuel, M. J. Jory, and W. L. Barnes, "Bragg scattering from periodically microstructured light emitting diodes," *Applied Physics Letters*, vol. 77, no. 21, pp. 3340–3342, 2000.

[3] Y. J. Lee, S. H. Kim, J. Huh et al., "A high-extraction-efficiency nanopatterned organic light-emitting diode," *Applied Physics Letters*, vol. 82, no. 21, pp. 3779–3781, 2003.

[4] W. Li, R. A. Jones, S. C. Allen, J. C. Heikenfeld, and A. J. Steck, "Maximizing Alq/sub 3/OLED internal and external efficiencies: charge balanced device structure and color conversion outcoupling lenses," *Journal of Display Thecnology*, vol. 2, no. 2, pp. 143–152, 2006.

[5] J. J. Shiang, T. J. Faircloth, and A. R. Duggal, "Experimental demonstration of increased organic light emitting device output via volumetric light scattering," *Journal of Applied Physics*, vol. 95, no. 5, pp. 2889–2895, 2004.

[6] R. Bathelt, D. Buchhauser, C. Gärditz, R. Paetzold, and P. Wellmann, "Light extraction from OLEDs for lighting applications through light scattering," *Organic Electronics*, vol. 8, no. 4, pp. 293–299, 2007.

[7] T. Nakamura, H. Fujii, N. Juni, S. Nakanishi, M. Miyatake, and N. Tsutsumi, "Extraction of waveguided light by anisotropic scattering polarizer in organic electroluminescent devices," *Optical Review*, vol. 11, no. 6, pp. 370–377, 2004.

[8] K. Neyts and A. U. Nieto, "Importance of scattering and absorption for the outcoupling efficiency in organic light-emitting devices," *Journal of the Optical Society of America A*, vol. 23, no. 5, pp. 1201–1206, 2006.

[9] B. R. Yang, K. H. Liu, S. N. Lee, J. C. Hsieh, H. P. D. Shieh, and C. H. Chen, "Volumetric scattering layer for flexible transflective display," *Japanese Journal of Applied Physics*, vol. 47, no. 2, pp. 1016–1018, 2008.

[10] Y. Izumi, S. Okamoto, K. Takizawa, and K. Tanaka, "Improving the light out-coupling properties of inorganic thin-film electroluminescent devices," *Japanese Journal of Applied Physics Part 1*, vol. 41, no. 3, pp. 1284–1287, 2002.

[11] J. J. Shiang and A. R. Duggal, "Application of radiative transport theory to light extraction from organic light emitting diodes," *Journal of Applied Physics*, vol. 95, no. 5, pp. 2880–2888, 2004.

[12] C. C. M. Ma, Y. J. Chen, and H. C. Kuan, "Polystyrene nanocomposite materials: preparation, morphology, and mechanical, electrical, and thermal properties," *Journal of Applied Polymer Science*, vol. 98, no. 5, pp. 2266–2273, 2005.

[13] D. W. Chae and B. C. Kim, "Characterization on polystyrene/zinc oxide nanocomposites prepared from solution mixing," *Polymers for Advanced Technologies*, vol. 16, no. 11-12, pp. 846–850, 2006.

[14] Delta Tech., http://www.delta-technologies.com/Products.asp?C=13.

[15] C. Gümüş, O. M. Ozkendir, H. Kavak, and Y. Ufuktepe, "Structural and optical properties of zinc oxide thin films prepared by spray pyrolysis method," *Journal of Optoelectronics and Advanced Materials*, vol. 8, no. 1, pp. 299–303, 2006.

[16] X. W. Sun and H. S. Kwok, "Optical properties of epitaxially grown zinc oxide films on sapphire by pulsed laser deposition," *Journal of Applied Physics*, vol. 86, no. 1, pp. 408–411, 1999.

[17] J. C. Manifacier, J. Gasiot, and J. P. Fillard, "A simple method for the determination of the optical constants n, k and the thickness of a weakly absorbing thin film," *Journal of Physics E*, vol. 9, no. 11, pp. 1002–1004, 1976.

[18] R. Swanepoel, "Determination of the thickness and optical constants of amorphous silicon," *Journal of Physics E*, vol. 16, no. 12, pp. 1214–1222, 1983.

[19] R. Swanepoel, "Determination of surface roughness and optical constants of inhomogeneous amorphous silicon films," *Journal of Physics E*, vol. 17, no. 10, pp. 896–903, 1984.

[20] G. Mie, "Beiträge zur Optik trüber Medien, speziell kolloidaler Metallösungen," *Annalen der Physik*, vol. 25, no. 3, pp. 377–445, 1908.

[21] L. G. Henyey and J. L. Greenstein, "Diffuse radiation in the galaxy," *The Astrophysical Journal*, vol. 93, pp. 70–83, 1941.

[22] M. I. Mischchenko, *Scattering, Absorption, and Emission of Light by Small Particles*, Cambridge University press, New York, NY, USA, 2002, NASA 299-318.

[23] S. W. Cheong and K. L. Woon, "Modeling of light extraction efficiency of scattering thin film using Mie scattering," *Optica Applicata*, vol. 41, no. 1, pp. 217–223, 2011.

[24] N. K. Patel, S. Cinà, and J. H. Burroughes, "High-efficiency organic light-emitting diodes," *IEEE Journal on Selected Topics in Quantum Electronics*, vol. 8, no. 2, pp. 346–361, 2002.

[25] V. Bulović, V. B. Khalfin, G. Gu, P. E. Burrows, D. Z. Garbuzov, and S. R. Forrest, "Weak microcavity effects in organic light-emitting devices," *Physical Review B*, vol. 58, no. 7, pp. 3730–3740, 1998.

Hindawi Publishing Corporation
Journal of Nanomaterials
Volume 2012, Article ID 793679, 4 pages
doi:10.1155/2012/793679

Research Article

Investigation on the Optical and Surface Morphology of Conjugated Polymer MEH-PPV:ZnO Nanocomposite Thin Films

Nurul Zayana Yahya[1] and Mohamad Rusop[1,2]

[1] *NANO-SciTech Center (NST), Institute of Science, Universiti Teknologi MARA, 40450 Shah Alam, Malaysia*
[2] *NANO-ElecTronic Centre (NET), Faculty of Electrical Engineering, Universiti Teknologi MARA, 40450 Shah Alam, Malaysia*

Correspondence should be addressed to Nurul Zayana Yahya, yana_ukhwah@yahoo.com

Received 19 March 2012; Revised 29 April 2012; Accepted 29 April 2012

Academic Editor: Luis Antonio Sanchez de Almeida Prado

Thin films of red color poly(2-methoxy-5(2′-ethylhexyloxy)-phenylene vinylene) (MEH-PPV) containing different weight percent of ZnO nanoparticles were obtained by spin-coating techniques. The MEH-PPV:ZnO solutions were spin coated onto silicon and glass substrates. The spun MEH-PPV:ZnO thin films were then used to investigate optical properties by using ultraviolet-visible spectrometer (UV-Vis) and photoluminescence spectrophotometer (PL). The morphologies were investigated by using field emission scanning electron microscopy (FESEM), while the identification of ZnO in the final product was determined by using energy-dispersive X-ray spectroscopy (EDS). The UV-Vis absorption band increases, while the optical bandgap decreases when the amount of ZnO nanoparticles increases. ZnO nanoparticles apparently have no effect on the conjugation segments of MEH-PPV. PL spectra show that the emission peak increases and slightly red shift as ZnO concentration increases. Based on SEM images of MEH-PPV:ZnO nanocomposite thin films, ZnO nanoparticles form agglomerated regions.

1. Introduction

Recently, the preparation of polymer-inorganic composite has been increasingly studied due to the novel synergy effects as well as enhanced optical and electronic properties. Previous studies have reported on polymer-inorganic solar cells using CdSe [1], TiO_2 [2], SiO_2 [3], and ZnO nanoparticles [4]. The composites have good effects on optical, electronic properties [5] and also improve the stability [6] which is important in organic devices. The effects of the nanoparticles on the structure and optical properties of the polymer are still a subject of research. Baraton et al. reported that blends using TiO_2 nanoparticles do not break the PPV, conjugation lengths [7]. Yang et al. observed that SiO_2 nanoparticles would reduce the conjugation lengths of PPV and this reduction becomes significantly important as the content of SiO_2 increases [8].

Conducting unsaturated poly(2-methoxy-5(2′-ethylhexyloxy)-phenylene vinylene] (MEH-PPV) has attracted a great deal of interests in its applications in PLEDs [9], FETs [10], and solar cells [11] due to its particular structure and luminescent properties. Its asymmetric alkoxy side chains make MEH-PPV soluble in common organic solvents such as tetrahydrofuran (THF), chloroform, xylene, and toluene. In this work, we studied nanocomposites made by incorporation of the different amount of ZnO nanoparticles in MEH-PPV matrix. Since MEH-PPV is a soluble conjugated polymer, one can incorporate oxide nanoparticles into MEH-PPV directly. We investigated the optical and structural properties of the hybrid materials and discussed the influences of the nature of the behavior of the composites.

2. Experimental Method

MEH-PPV, sodium dodecyl sulfate (SDS), and ZnO nanoparticles were purchased from Sigma-Aldrich and used as supplied. The average molecular weight (M_n) of the polymer ranges from 40,000 to 70,000 g/mol. Five solutions of MEH-PPV in tetrahydrofuran (THF) were mixed with <100 nm diameter of ZnO in different weight percents (0 wt%, 5 wt%, 10 wt%, 15 wt%, and 20 wt%). A certain amount of SDS was added into MEH-PPV:ZnO solutions to

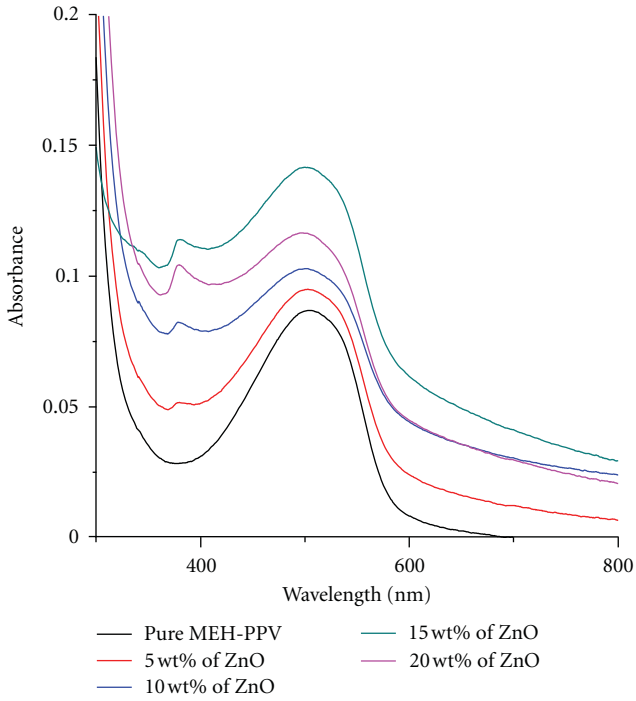

Figure 1: UV-Vis absorption spectra of pure MEH-PPV and its nanocomposites.

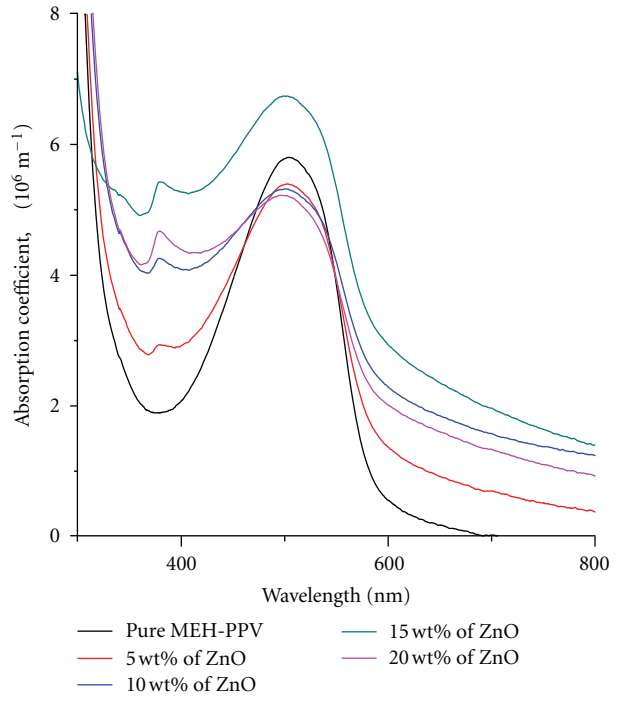

Figure 2: Absorption coefficient spectra of pure MEH-PPV and its nanocomposites.

improve the dispersion of ZnO into the MEH-PPV matrix. Then, the nanocomposite solutions were sonicated for 30 minutes and further stirred for 1 hour. Thin films were obtained by spin coating onto cleaned silicon and glass substrates. This process was repeated for 10 times to yield the required thickness.

Optical characterization of the fresh samples was performed by UV-Vis using JASCO V-670, and the thickness was measured using Veeco Dektak 150. PL measurement was made by using a Fluorolog 3 spectrophotometer. An SEM image was obtained using JEOL JSM-7600F equipped with EDS.

3. Results and Discussion

3.1. UV-Vis Spectra. Figure 1 shows the UV-Vis absorption spectra (300–800 nm) of pure MEH-PPV and its nanocomposite thin films. The absorption peaks of the pure MEH-PPV and its composites are located at ~507 nm. These peaks are attributed to π-π^* transition of the conjugated polymer [12]. The addition of ZnO nanoparticles to MEH-PPV shows an increment in the optical absorptions which means that ZnO helps in light harvesting in the visible region. These increments are due to the absorption of ZnO nanoparticles into the MEH-PPV. The increase in absorption is higher as the amount of nanoparticles increases. As the concentration of ZnO nanoparticles increases, the absorption peaks also appear broadened. This may be due to the distribution of energy levels corresponding to the π-π^* transition. The absorption peaks of ZnO nanoparticles appear in the UV region (<400 nm). This peak increases when the amount of ZnO nanoparticles increases. This could also be due to the nano-size of the ZnO, which could increase the surface area, thus making the absorption stronger. From transmittance data, the absorption coefficient (α) can be calculated. α was obtained through Lambert's law, which is indicated by the following relation:

$$\alpha = \frac{1}{t} \ln\left(\frac{1}{T}\right). \quad (1)$$

t is the thickness of thin films, and T is the transmittance. Figure 2 shows the α spectra of the pure MEH-PPV and its nanocomposites. α depends on the wavelength of light, which is being absorbed. MEH-PPV:ZnO nanocomposites containing 15 wt% of ZnO have higher absorption coefficient compared to the other samples. The optical bandgap was determined using Tauc's plot. The relationship between direct bandgap and photon energy is given as

$$\alpha h\nu = A(h\nu - E_g)^{1/2}. \quad (2)$$

The extrapolation of the straight-line portion of the $(\alpha h\nu)^2$ versus $h\nu$ for pure MEH-PPV and MEH-PPV:ZnO nanocomposites revealed that the optical bandgap of the nanocomposites, slightly decreases when the amount of ZnO nanoparticles in MEH-PPV increases as seen in Figure 3. The differences in the bandgap values are too small between the pure polymer and its nanocomposites and ZnO nanoparticles apparently do not affect the conjugation length of MEH-PPV. Therefore, addition of ZnO nanoparticles will not affect the structure of the polymer and hence its optical properties. The thickness and optical bandgap of pure MEH-PPV and its nanocomposites are summarized in Table 1.

Table 1: The thickness and optical bandgap of pure MEH-PPV and its nanocomposites.

Sample	Thickness (nm)	Optical bandgap (eV)
Pure MEH-PPV	34.50	2.1941
5 wt% of ZnO	40.51	2.1664
10 wt% of ZnO	44.51	2.1299
15 wt% of ZnO	48.35	2.1217
20 wt% of ZnO	51.36	2.1340

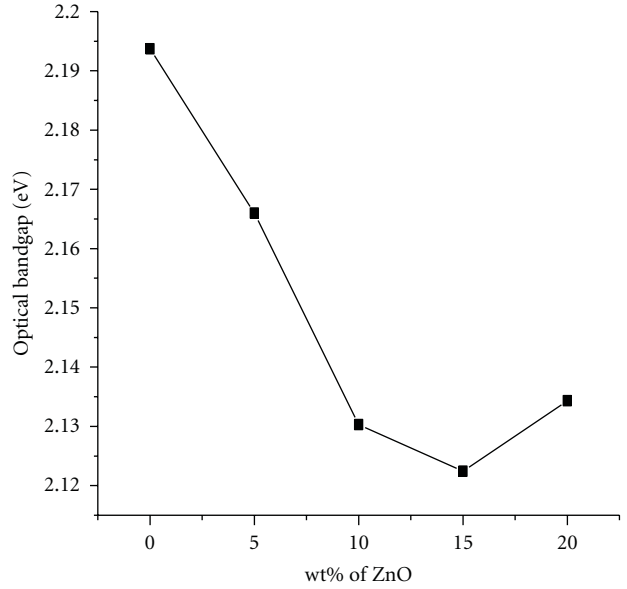

Figure 3: Optical bandgap of pure MEH-PPV and its nanocomposites.

3.2. PL Spectra. Figure 4 shows that the PL spectra of pure MEH-PPV and MEH-PPV:ZnO nanocomposites in the wavelength range from 500 to 700 nm. The emission peak of pure MEH-PPV was found to be at 571 nm due to the emission characteristic of PPV backbone, which arises from the relaxation of excited π-electrons to the ground state. The peak for pure MEH-PPV at 617 nm is related to the interchain states [13]. It can be seen that the emission peak increases and slightly red shift as ZnO concentration increases. A maximum emission is found for nanocomposite with 20 wt% of ZnO. This is related to the high-energy transfer from the particles to the polymer. The change in PL emission peak can be explained in two ways: chain separation and charge trapping effect. ZnO is an n-type semiconductor that can trap electrons and allows more holes to recombine through the interface of MEH-PPV and ZnO. Then, the exciton formation inside nanocomposite layer increases and enhances luminescent properties [14]. Furthermore, the red shift in luminescence peak is related with the changes in the conjugation lengths [3]. The red shift occurred due to the formation of nanoparticles agglomeration in the nanocomposites.

3.3. SEM Images. Figures 5(a), 5(b), and 5(c) represent the effect of the different amount of ZnO nanoparticles

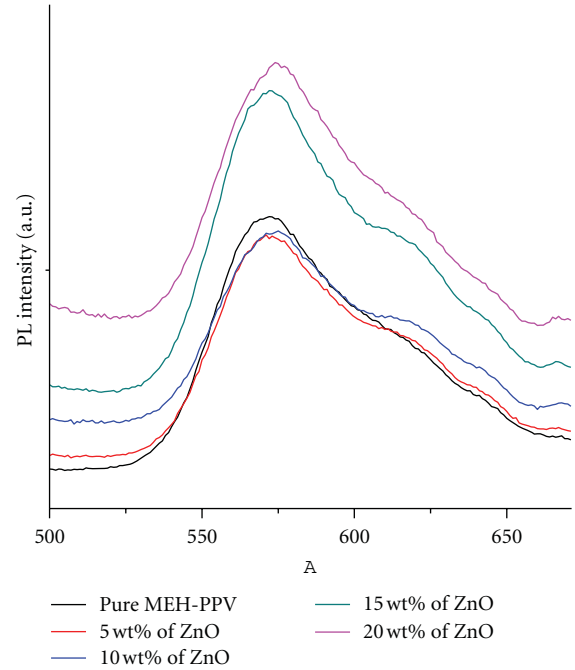

Figure 4: PL spectra of pure MEH-PPV and its nanocomposites.

on the degree of agglomeration and distribution of ZnO particles in nanocomposites thin films. As an amount of ZnO nanoparticles increases, the agglomeration regions become larger, and the phase separation between ZnO and MEH-PPV for nanocomposites thin films can be seen clearly. However, in this paper, the certain amount of SDS was added to improve the dispersion of ZnO with sonication treatment. Although thin films containing 5 and 20 wt% ZnO nanoparticles show agglomeration regions, the ZnO is evenly distributed. ZnO nanoparticles may be dispersed homogeneously in hydroxyl-containing solvents such as EG and glycerol because there are many hydroxyl groups on the surface of the oxide nanoparticles. In this paper, tetrahydrofuran was used as the solvent and ZnO nanoparticles were agglomerated. This agglomeration can be reduced by modifying the nanoparticles structure by adding some surfactant or wetting agent to obtain homogeneous thin films. Figure 5(d) shows the EDS result of composite containing 20 wt% of ZnO nanoparticles. The ZnO peak clearly shows the present ZnO in the thin films.

4. Conclusion

In this paper, we investigated the optical and morphological properties of MEH-PPV containing different weight percents of ZnO nanoparticles. UV-Vis absorption spectra for MEH-PPV:ZnO are more intensive compared to the pure MEH-PPV. Small amounts of ZnO nanoparticles added into MEH-PPV matrix have no effect on conjugation segments. The optical bandgap also slightly decreases when the amount of ZnO increases. PL spectra show that the emission peak increases and slightly red shift as ZnO concentration increases. SEM images show that the degree of agglomeration increases as the amount of ZnO increases.

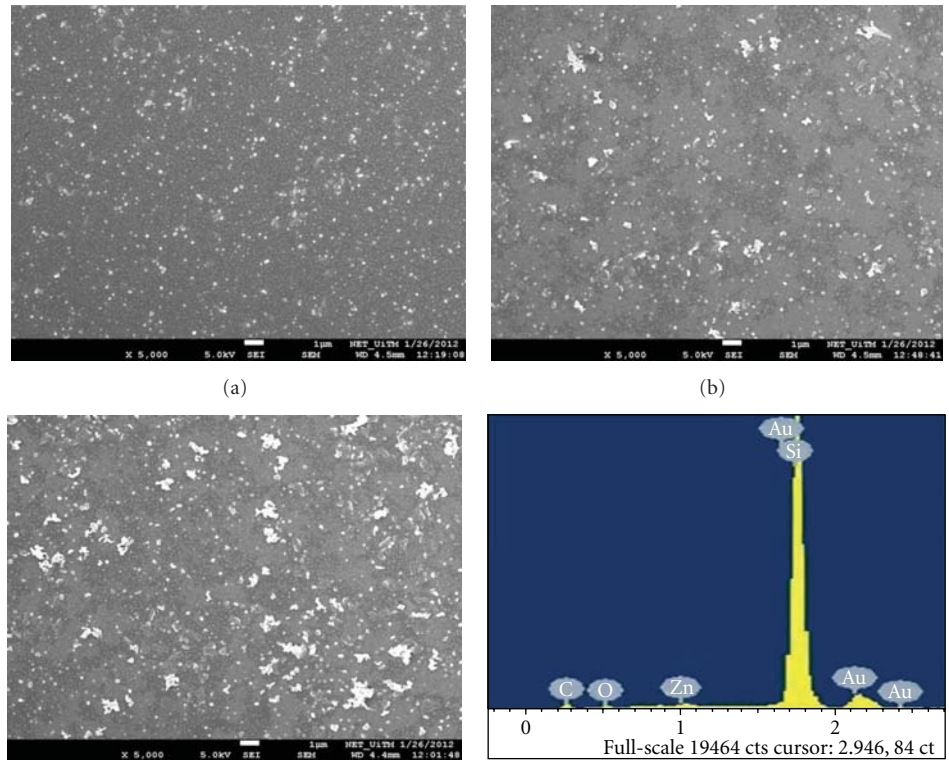

Figure 5: SEM images of pure MEH-PPV and its nanocomposites: (a) 0 wt%, (b) 5 wt%, and (c) 20 wt% of ZnO and (d) EDS result of MEH-PPV: 20 wt% of ZnO.

Acknowledgments

The authors would like to thank Research Management Institute, UiTM (Excellence Fund 600-RMI/ST/DANA 5/3/Dst (436/2011) for the financial support and the members of the Faculty of Applied Sciences, UiTM, Shah Alam for their guidance and advice in completing this project.

References

[1] W. U. Huynh, J. J. Dittmer, and A. P. Alivisatos, "Hybrid nanorod-polymer solar cells," *Science*, vol. 295, no. 5564, pp. 2425–2427, 2002.

[2] A. Petrella, M. Tamborra, M. L. Curri et al., "Colloidal TiO_2 nanocrystals/MEH-PPV nanocomposites: photo(electro) chemical study," *Journal of Physical Chemistry B*, vol. 109, no. 4, pp. 1554–1562, 2005.

[3] S. H. Yang, P. Le Rendu, T. P. Nguyen, and C. S. Hsu, "Fabrication of MEH-PPV/SiO_2 and MEH-PPV/TiO_2 nanocomposites with enhanced luminescent stabilities," *Reviews on Advanced Materials Science*, vol. 15, no. 2, pp. 144–149, 2007.

[4] W. J. E. Beek, M. M. Wienk, and R. A. J. Janssen, "Hybrid solar cells from regioregular polythiophene and ZnO nanoparticles," *Advanced Functional Materials*, vol. 16, no. 8, pp. 1112–1116, 2006.

[5] G. Kickelbick, "Concepts for the incorporation of inorganic building blocks into organic polymers on a nanoscale," *Progress in Polymer Science*, vol. 28, no. 1, pp. 83–114, 2003.

[6] H. Neugebauer, C. Brabec, J. C. Hummelen, and N. S. Sariciftci, "Stability and photodegradation mechanisms of conjugated polymer/fullerene plastic solar cells," *Solar Energy Materials and Solar Cells*, vol. 61, no. 1, pp. 35–42, 2000.

[7] M. I. Baraton, L. Merhari, J. Wang, and K. E. Gonsalves, "Investigation of the TiO_2/PPV nanocomposite for gas sensing applications," *Nanotechnology*, vol. 9, no. 4, pp. 356–359, 1998.

[8] S. H. Yang, T. P. Nguyen, P. Le Rendu, and C. S. Hsu, "Optical and electrical investigations of poly(p-phenylene vinylene)/silicon oxide and poly(p-phenylene vinylene)/titanium oxide nanocomposites," *Thin Solid Films*, vol. 471, no. 1-2, pp. 230–235, 2005.

[9] T. F. Guo, F. S. Yang, Z. J. Tsai, T. C. Wen, S. N. Hsieh, and Y. S. Fu, "High-performance polymer light-emitting diodes utilizing modified Al cathode," *Applied Physics Letters*, vol. 87, no. 1, Article ID 013504, 3 pages, 2005.

[10] T. Sakanoue, E. Fujiwara, R. Yamada, and H. Tada, "Visible light emission from polymer-based field-effect transistors," *Applied Physics Letters*, vol. 84, no. 16, pp. 3037–3039, 2004.

[11] H. Wang, C. C. Oey, A. B. Djurišić et al., "Titania bicontinuous network structures for solar cell applications," *Applied Physics Letters*, vol. 87, no. 2, Article ID 023507, 3 pages, 2005.

[12] S. S. Kim, J. Jo, C. Chun, J. C. Hong, and D. Y. Kim, "Hybrid solar cells with ordered TiO_2 nanostructures and MEH-PPV," *Journal of Photochemistry and Photobiology A*, vol. 188, no. 2-3, pp. 364–370, 2007.

[13] R. Traiphol, N. Charoenthai, T. Srikhirin, T. Kerdcharoen, T. Osotchan, and T. Maturos, "Chain organization and photophysics of conjugated polymer in poor solvents: aggregates, agglomerates and collapsed coils," *Polymer*, vol. 48, no. 3, pp. 813–826, 2007.

[14] J. P. Zou, P. Le Rendu, I. Musa et al., "Investigation of the optical properties of polyfluorene/ZnO nanocomposites," *Thin Solid Films*, vol. 519, no. 12, pp. 3997–4003, 2011.

Hindawi Publishing Corporation
Journal of Nanomaterials
Volume 2012, Article ID 532080, 9 pages
doi:10.1155/2012/532080

Research Article

Comparative Characterization of Multiscale Carbon Fiber Composite with Long and Short MWCNTs at Higher Weight Fractions

Michael Zimmer,[1] Qunfeng Cheng,[1] Shu Li,[1] James Brooks,[2] Richard Liang,[1] Ben Wang,[1] and Chuck Zhang[1]

[1] *High-Performance Materials Institute, Florida State University, 2005 Levy Avenue, Tallahassee, FL 32310, USA*
[2] *National High Magnetic Field Laboratory, Florida State University, A311 1800 E. Paul Dirac Dr., Tallahassee, FL 32310, USA*

Correspondence should be addressed to Michael Zimmer, mmzimmer@gmail.com

Received 2 January 2012; Revised 26 March 2012; Accepted 11 April 2012

Academic Editor: Marcio Rodrigo Loos

There are documented advantages to using carbon nanotubes (CNTs) in composites for various property enhancements. However, to date, only limited studies have been conducted on using of longer CNTs over 1 mm in length. This study used long multiwalled carbon nanotubes (LMWCNTs) and their longer extended networks to test multiple properties in thermal conductivity, electrical conductivity, mechanical strength, and modulus and then compared these properties to those of shorter multi-walled carbon nanotubes (SMWCNTs). For carbon fiber-reinforced composites, the longer graphite paths from LMWCNTs in the matrix were expected to improve all properties. The longer networks were expected to allow for more undisturbed phonon transportation to improve thermal conductivity. This in turn relates to improved electrical conductivity and better mechanical properties. However, results have shown that the LMWCNTs do not improve or decrease thermal conductivity, whereas the shorter MWCNTs provide mixed results. LMWCNTs did show improvements in electrical, mechanical, and physical properties, but compared to shorter MWCNTs, the results in other certain properties varied. This perplexing outcome resides in the functioning of the networks made by both the LMWCNTs and shorter MWCNTs.

1. Introduction

The addition of carbon nanotubes (CNTs) to improve various mechanical and electrical properties in fiber-reinforced composites has undergone numerous studies [1–6]. A great deal of research has been published on the thermal conductivity improvements of CNT/polymer-based composites [7–12]. However, very few studies have been conducted to show the thermal conductivity characteristics of fiber-reinforced composites with CNTs enhancements [13]. All studies were done with the use of single-walled carbon nanotubes (SWCNTs) and multiwalled carbon nanotubes (MWCNTs) of lengths ranging from 10 nm to 80 μm [8, 11, 13] when length dimensions were provided. One study showed the delamination toughness of what they state is long multiwalled carbon nanotubes [14] with a maximum length of 80 μm. To date, however, no studies have shown the thermal conductivity, electrical conductivity, and mechanical properties of millimeters-long multiwalled carbon nanotubes (LMWCNTs) in fiber-reinforced composites.

This study tests the LMWCNTs versus shorter multiwalled carbon nanotubes (SMWCNTs) at a range of 0.5 wt% to 10.0 wt%. This is one of the first introductions of extremely high loadings of CNTs in polymer composites. The limiting factor to having high loading additives in viscous resins is the dispersion quality. One method to overcome the thick viscosity of epoxy resins is using solvents to dilute the mixture to use high-speed shear mixing with blades. The disadvantage to this process is removing the solvent 100% and not, ultimately, affecting the resin composition. Using alternative shear mixers without solvents has been discovered in this study and results in uniform dispersion to accomplish high CNT-loaded composites. The LMWCNTs used are from Nanotech Labs CVD grown to 2 mm in length and

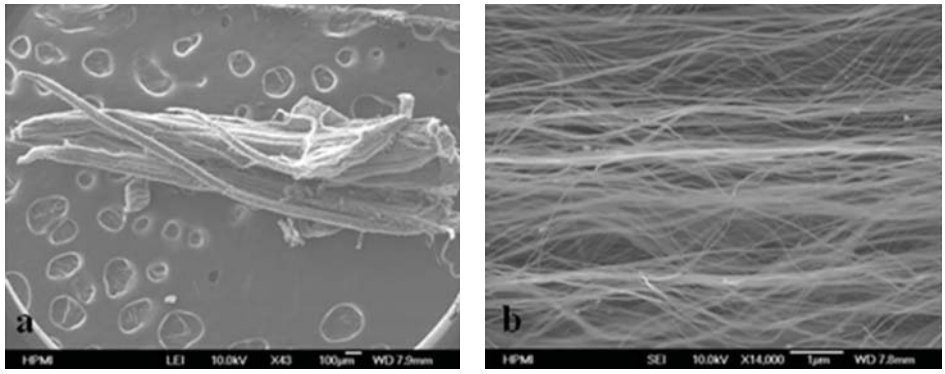

(a) (b)

Figure 1: SEM image of long MWCNTs: (a) full view of a piece of the LMWCNTs forest, (b) magnified image of forest.

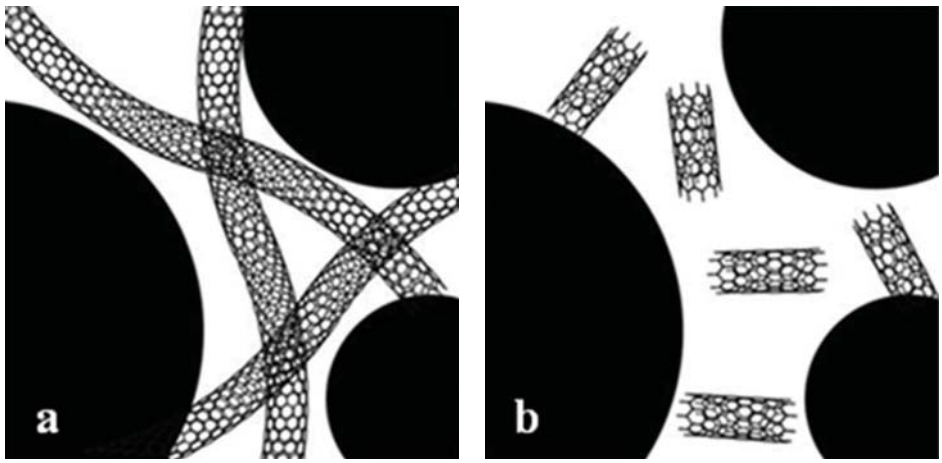

(a) (b)

Figure 2: Comparison of LMWCNTs (a) and SMWCNTs (b) introduced in fiber-reinforced composite.

compare them to 1 micron length high-purity MWCNTs from Bayer. Figure 1 shows SEM images confirming the length of LMWCNTs up to 1.5 mm.

Using LMWCNT and SMWCNT in composites would be to overcome the primary weakness of low thermal conductivity in the matrix of fiber-reinforced composites. Studies have been conducted to improve the thermal characteristics of polymers with the additives of CNTs or other nanoparticles and fillers [15, 16]. The interlaminar interface in composite structures is a resin-rich layer. Improving the thermal performance of the interlaminar interface would increase the through-thickness thermal conductivity. Prior works for enhancing the interlaminar conductivity through the use of nanostructuring have shown good results using carbon black [17].

Phonon thermal conductivity is the principal mechanism of heat transfer that is responsible for thermal conductivity of composite materials [18, 19]. Phonon transport is known as phonon-phonon scattering or normal scattering [18]. Thermal conductivity benefits from normal scattering. Having a continuous conductive path that is free of defects and disruptions with the molecular structure that is crystalline-like, such as metal or graphite lattice, would promote an effective and efficient means of producing high thermal conductivity in composites [18–22]. The polymers' non-crystalline structure hinders the normal scattering [23].

One of the studies investigates if the use of LMWCNTs would provide longer network paths for more phonon transportation using the superior graphite lattice of the nanotube to overcome the polymer's scattering effects. Figure 2 is a representation of the LMWCNT in fiber-reinforced composite compared to shorter MWCNTs. The improved, longer networks should minimize the defects and disruptions the phonons encounter and reduce the resistance along the heat flow path. The electrical conductivity should also benefit from these principles as its conductivity is dictated by electron transportation [18]. With long networks, the electrons should travel with less resistance throughout the composite. Along with the thermal and electrical performance of the composite with LMWCNTs, the mechanical properties should benefit as well. It is expected that the LMWCNT will outperform SMWCNT.

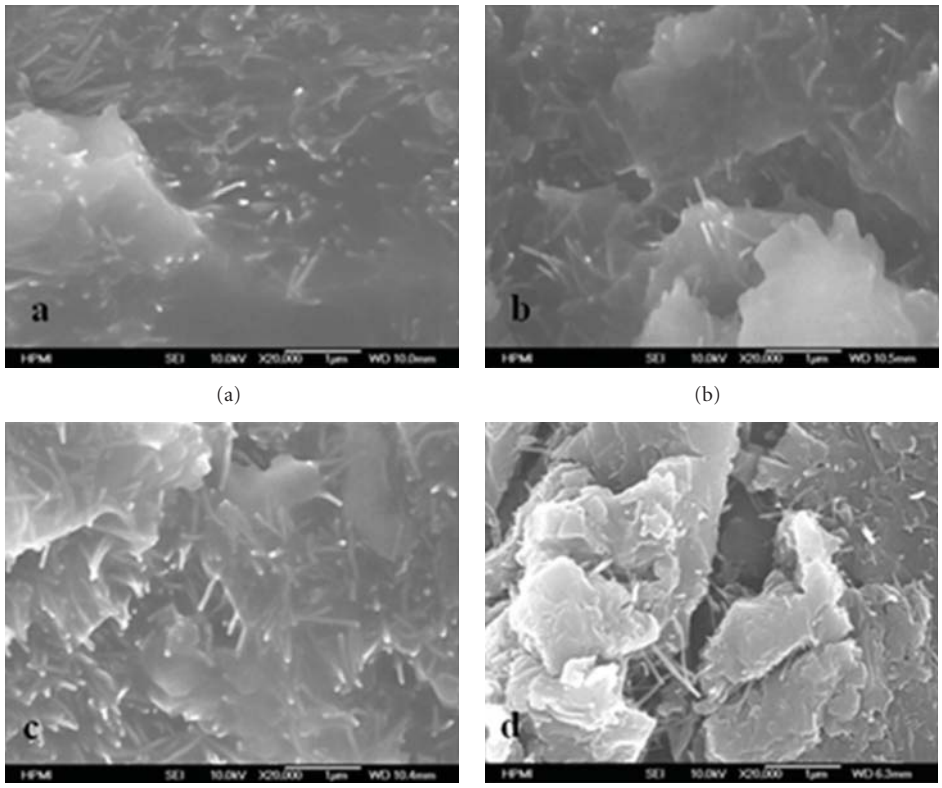

(a) (b)

(c) (d)

Figure 3: SEM of LMWCNT multiscale composite for (a) 0.5 wt%, (b) 1.0 wt%, (c) 5.0 wt%, and (d) 10.0 wt%.

2. Experiment

2.1. Fabrication. LMWCNTs and SMWCNTs were introduced into fiber-reinforced composites by creating a highly loaded nanotube epoxy mixture. The epoxy/nanotube mixture (Epon 862 and Nanotech Labs LMWCNTs) was made using Exakt triple roller mills for shear mixing. Four MWCNT concentrations were mixed at 0.5 wt%, 1.0 wt%, 5.0 wt%, and 10 wt%. The shear mixing process had 3 controllable parameters to produce uniform mixtures: time span of mixing, gap size between the rollers, and speed of the rollers. As the gap size decreased to 5 μm and the speed increased, the MWCNT clumps broke down resulting in higher shearing of the material. The length of time the material underwent the process ensured a uniform mixture.

The MWCNTs/Epon 862 mixture was then incorporated into IM7 carbon fabric for composite fabrication. The fabrication of the composite was performed as a 4-layer hand-layup process using compression molding for curing. The curing cycle was at 177°C for 4 hours. A 55% volume fraction of fiber was achieved for each sample using the controlled molding process. Five, 50 × 50 × 1 mm sample panels of each CNT concentration were made in which sample pieces were cut from for characterization testing.

2.2. Quality Test. SEM imaging was used to visually identify uniformity of the MWCNTs/Epon 862 mixture in the composite. Figures 3 and 4 show the SEM image results for the LMWCNTs and SMWCNTs multiscale composites, respectively. The LMWCNTs could be identified at lower magnifications up to ×2,500, whereas the SMWCNTs required at least ×60,000 for 0.5 wt% and 1.0 wt%. At ×20,000 magnification, the SMWCNTs could be identified for 5.0 wt% and 10 wt%. The images show random CNT orientation and good uniformity of the mixture.

Between the C-Scan and SEM tests, the composites for both LMWCNTs and SMWCNTs showed little or no defects and had a uniformity in material that made for reliable testing and analysis. Samples were polished on the surface to remove any roughness and underwent a sonication bath at 15 minute intervals to clean any debris that might affect any test results.

3. Results

3.1. Thermal Characterization. Samples were cut into 10 × 10 mm squares for thermal diffusivity testing using Netzsch LFA 457 MicroFlash system. Netzsch LFA 457 uses a laser flash method for absolute diffusivity measurement results. Each sample was tested with a reference sample using Pyrex 7740 for specific heat (C_p) calculation using the LFA 457. Due to the samples' anisotropic nature, using DSC would not reveal reliable specific heat results. The LFA 457 can test the thermal diffusivity while simultaneously extrapolating the C_p measurement of the unknown samples. Gathering the diffusivity (α) results and the measured density (ρ) and C_p,

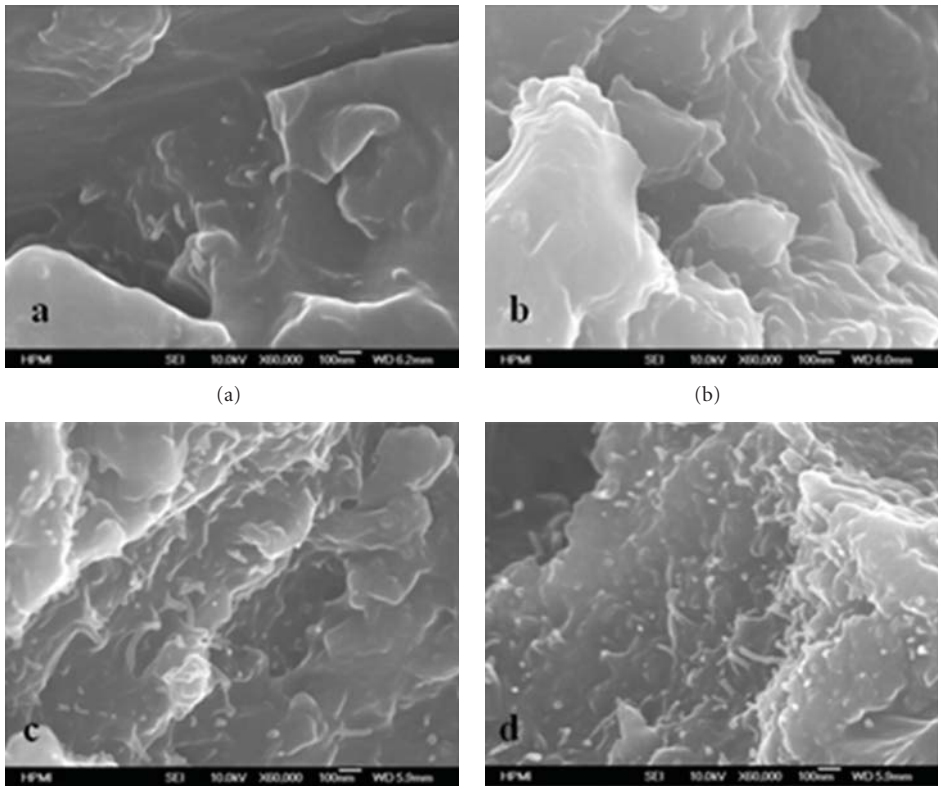

(a) (b)

(c) (d)

Figure 4: SEM of SMWCNTs multiscale composite for (a) 0.5 wt%, (b) 1.0 wt%, (c) 5.0 wt%, and (d) 10.0 wt%.

the thermal conductivity (K) of the samples was calculated using (1). Figures 5 and 6 show the thermal conductivity results for both types of samples taking the average of 6 separate tests:

$$K = \alpha \cdot \rho \cdot C_p. \quad (1)$$

The results of the LMWCNT samples were other than what was expected. It was thought that the thermal conductivity values would increase with increased LMWCNT loading. Only the samples with 10 wt% loading had a clear advantage. The other samples were approximately the same thermal conductance at each temperature range. The SMWCNT samples had an inverse effect compared to the LMWCNT samples but have a clear definition at which loading performs better. Thermal conductivity at 0.5 wt% of SMWCNTs was superior to all samples. As the loading increased, the thermal conductivity values decreased below that of the neat sample. Thermally conductive materials typically have high diffusivity and specific heat values. It was expected that the multiscale composites would show higher values across all loading levels compared to the neat sample. Table 1 shows an excerpt of the specific heat and thermal diffusivity of both samples. The thermal conductivity, therefore, showed no improvements. Only the results of the 10.0 wt% sample showed marginal improvements. This could be due to the induced loading.

The thermal conductivity results for LMWCNT and SMWCNT have altered perception of the thermal behavior

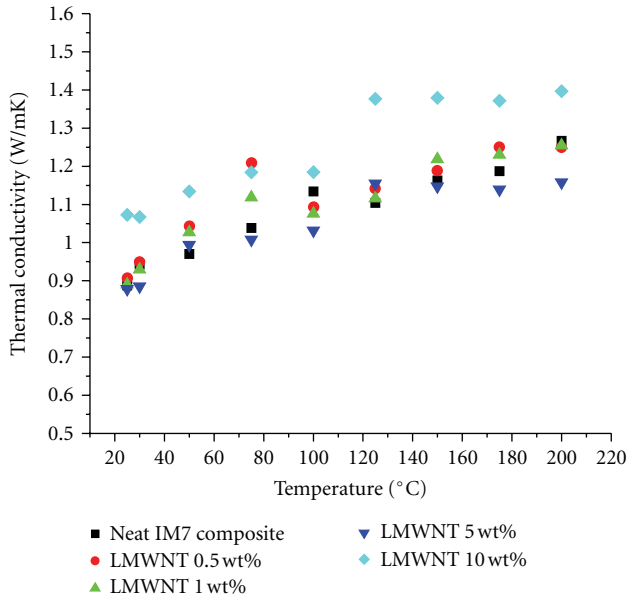

Figure 5: LMWCNT multiscale composite thermal conductivity.

expected in multiscale composites. The idea to add high conductive additives to composites to increase performance must now consider several factors: the size of the material, loading, and possible material structure and orientation

Table 1: Thermal diffusivity and specific heat values of LMWNT and SMWNT samples.

		LMWNT		SMWNT	
		α	C_p	α	C_p
25°C	0.5 wt%	0.662	0.863	0.695	0.851
	1.0 wt%	0.642	0.882	0.622	0.811
	5.0 wt%	0.641	0.885	0.618	0.786
	10.0 wt%	0.528	1.277	0.490	0.943
50°C	0.5 wt%	0.648	1.014	0.674	0.982
	1.0 wt%	0.625	1.045	0.608	0.955
	5.0 wt%	0.617	1.034	0.606	0.859
	10.0 wt%	0.493	1.456	0.476	1.052
100°C	0.5 wt%	0.615	1.120	0.638	1.246
	1.0 wt%	0.592	1.156	0.575	1.209
	5.0 wt%	0.582	1.136	0.572	1.014
	10.0 wt%	0.464	1.614	0.444	1.199
200°C	0.5 wt%	0.537	1.465	0.557	1.513
	1.0 wt%	0.516	1.547	0.502	1.495
	5.0 wt%	0.504	1.475	0.497	1.405
	10.0 wt%	0.387	2.276	0.371	1.720

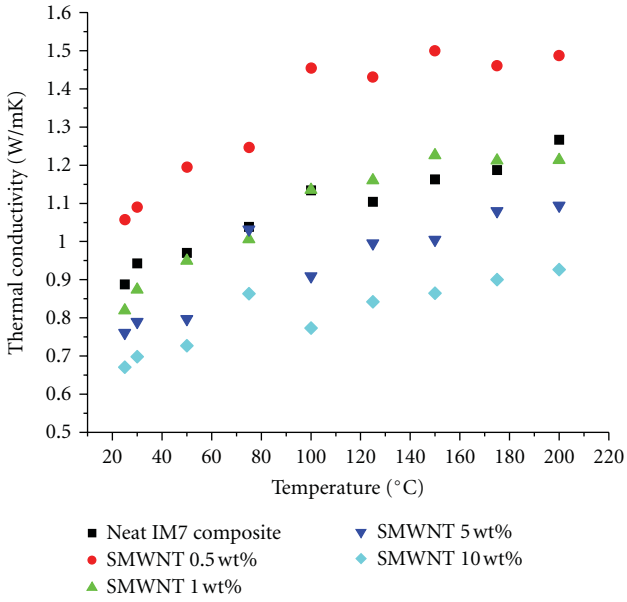

Figure 6: SMWCNT multiscale composite thermal conductivity.

in the composite. What is understood is that chemical composition of polymers will independently dictate the thermal conductivity. Low thermal excitation of polymers along the molecular chain could possibly be accounted for by diffusion of vibrational energy between atoms that relate to thermal transport [24]. Other factors must be present of the unchanging and lowering of thermal conductivity values in the composite samples.

A research group [25] looked at the thermal conductivity effects of carbon nanotube (CNT) networks. The study revealed that packed loadings of CNTs of high heat conductance behaved as thermal insulators [25]. This discovery is largely contributed to the multiple contact resistance or junctions of the CNTs that create interference effects on the transport of phonons [25].

Phonons can be impeded by position and vibration of atoms in neighboring planes [26]. This would be a possible explanation of the interference effects on the transport of phonons. With increased loading, there is more packing of MWCNTs where the scattering effects of the phonons in each MWCNTs disrupt the harmonic frequency of the neighboring phonon transportation in adjacent MWCNTs.

The diffused thermal conduction is also compounded by a well-known point that energy transfer between CNTs is affected by the interfacial resistance with the surrounding polymer [19]. Similarly, a major thermal resistance factor when dealing with multiscale composites is the thermal boundary resistance. The thermal boundary resistance is the increased heat resistance at the interface of two different materials [24, 26]. As heat is applied to the system, the heat passes through the carbon fiber region with minimal decrease in conductivity. The moment the heat propagation reaches the boundary into the resin, a major heat loss occurs. Materials made with mismatched properties in phonon velocity, specific heat, and density show a more significant reduction in thermal conduction than with materials made with substituent parts of similar properties [19, 24, 27].

There are many contributing factors that play a role into the thermal effects observed from the LMWCNTs and SMWCNTs multiscale composites. In the case of the LMWCNTs, it is possible that the long networks snake around in multiple directions that could divert the paths other than the through-thickness direction as desired. Another theory is that the length of LMWCNTs does not create a ballistic

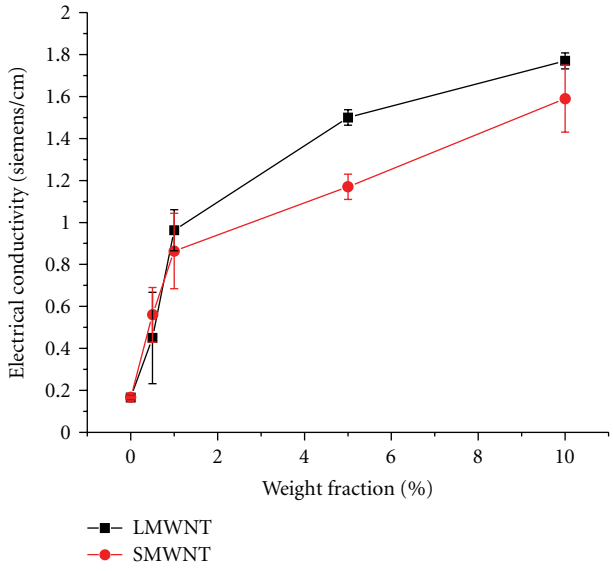

Figure 7: Electrical conductivity of LMWCNT and SMWCNT multiscale composite.

effect of phonons dispersing heat energy [19, 27] where the SMWCNTs at low loadings would. These results are some of the first to be seen at high loadings of carbon nanotubes in a multiscale composite.

3.2. Electrical Characterization. With the enhancement of LMWCNTs and SMWCNTs into the carbon fiber-reinforced system, the interlaminar regions were expected to increase the overall electrical properties of the composite. Improvements in the resistivity were evident when electrical conductivity tests using the 2-probe test were performed. Figure 7 shows the improved electrical conductivity through the thickness of the composites as the LMWCNTs and SMWCNTs loading increased.

The trend in the electrical resistance was outstanding relative to the thermal conductivity indifference. It was thought that the behavior of either the thermal or electrical properties would show a parallel behavior for the other; however, this was not the case. The difference in characteristics between thermal and electrical properties is that the electrical conductance is not disrupted by the multiple contact points or junctions or disrupted by the proximity of other MWCNTs [25]. These junctions were not dependent on the coupling strength between multiple MWCNTs [25, 28]. The electrical conductivity had a strong relationship to the number of junctions made in the composite [29]. The increase in weight fraction of LMWCNTs and SMWCNTs created more contact points, decreasing the distance electrons need to tunnel through the polymer, effectively improving the electrical performance [26, 28–31]. This also demonstrates that more electron tunneling occurred. The phenomena of tunneling overcame the contact resistance that thermal transport encounters. For thermal transport, these resistances and the multiple scattering effects created major barriers. The electrical performance can be greatly impacted when the system has low thermal conductivity as the samples did [28].

3.3. Mechanical Characterization. Figures 8 and 9 show the average of five tests of the flexural modulus and strength using a Shimadzu AGS-J microtensile tester. The testing showed mixed result where some samples performed better in modulus and others did better in strength. In another study, a similar outcome in flexural modulus was observed where the initial loadings of CNTs acted as defects, but as the loading increased, the modulus outperformed the neat sample [32]. It is hard to compare how well LMWCNTs really performed in relation to shorter MWCNTs. In one study, with 1.0 wt% of MWCNTs in a glass fiber system, modulus and strength improved [33]. A study using T650 and 862 resin system with 1.0 wt% of MWCNTs resulted in decreased modulus and strength [34].

The LMWCNT multiscale composite had little or no effect in resisting deformation as the flexural strength shows. The modulus would suggest that low loadings outperformed higher loadings. This is reasonable considering that with higher loadings the stiffness of the sample would increase. However, in the SMWCNT multiscale composite, the values of both strength and modulus spiked at 10.0 wt%. This phenomenon was entirely unexpected. The Shimadzu was recalibrated, and fresh SMWCNT samples were tested again to validate the results with the same affect. Between the 5.0 wt% and 10.0 wt% loading range, the strength and modulus might be increasing. There was no literature published that could provide a valid explanation on the reasoning of the observed results for SMWCNT multiscale composites. Overall, the performance did follow the original theory that LMWCNTs and SMWCNTs would improve the mechanical performance. However, the LMWCNT samples did not show a clear advantage over the SMWCNT samples.

4. Conclusion

The uses of LMWCNTs in composites have yielded unique results. The expectation that the longer network paths of the LMWCNTs would provide better thermal performance at high loadings was proven false. Instead, they functioned more like insulators due to various interference effects and contact and boundary resistances on phonon transportation. Only did LMWCNT samples at 10 wt% showed a visible advantage. The SMWCNTs samples experienced degrading thermal conductivity by this same reasoning. However, the LMWCNTs' network proved to be exceptional on the electrical performance contributed by the increased junctions made in the polymer system with the carbon fibers compared to the SMWCNT multiscale composites. Additionally, the conditions for improving the electrical properties were promoted by the insulating factor the MWCNTs provided. The mechanical properties also benefitted from the use of LMWCNTs and SMWCNTs. It could be said that the SMWCNTs showed better performance with a unique value at 10 wt% without a plausible reasoning.

The research work with different MWCNT sizes and loading levels in fiber-reinforced composites has opened a

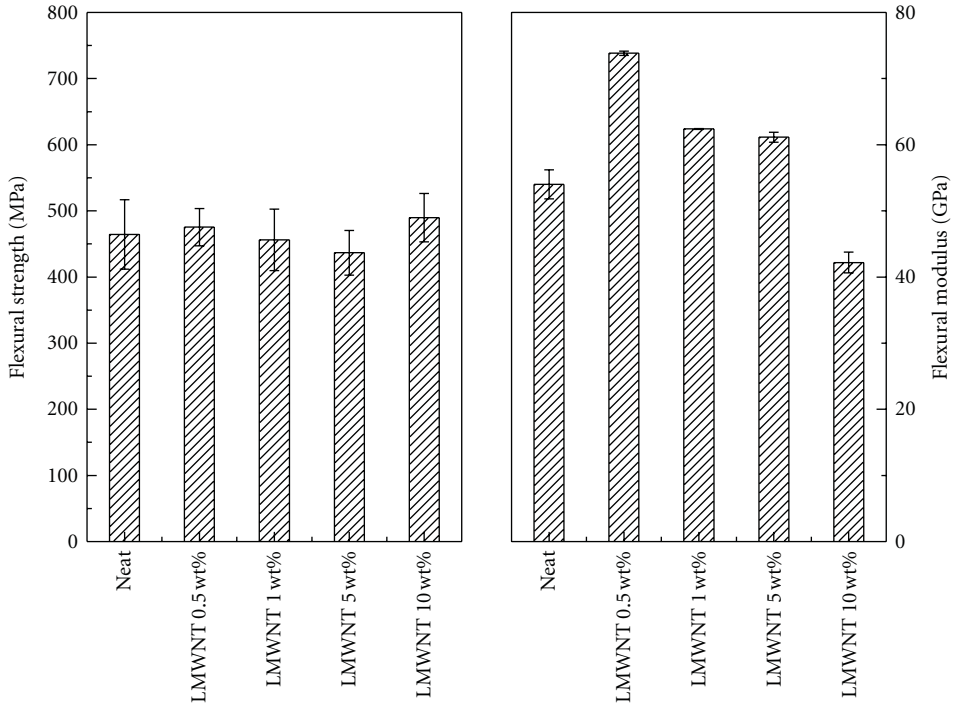

Figure 8: Shimadzu 3-point bending LMWCNT multiscale composite flexural modulus and strength test.

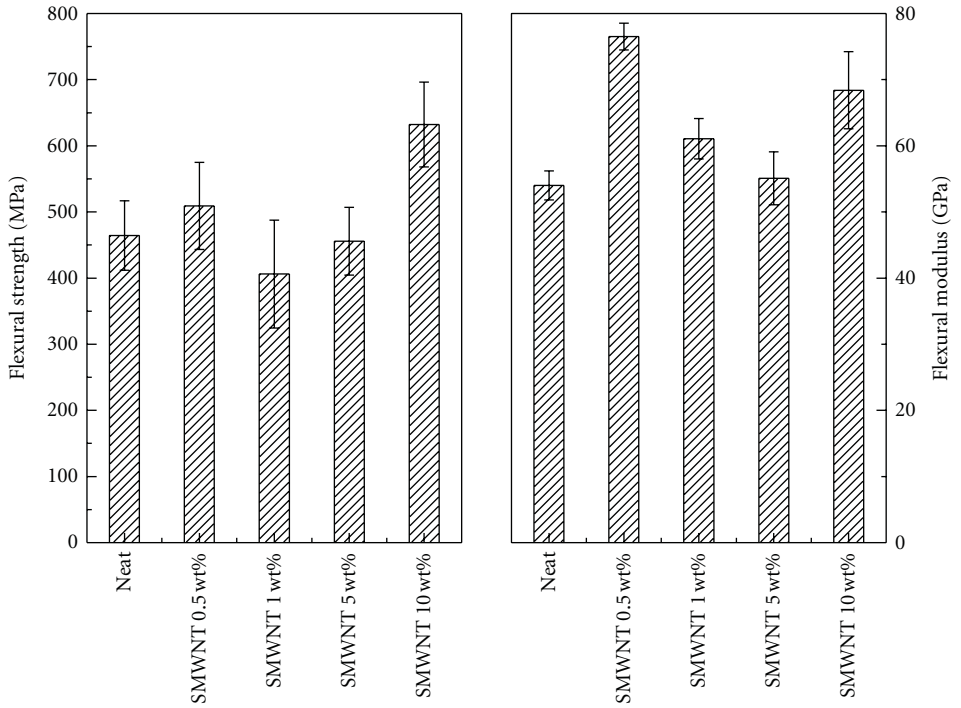

Figure 9: Shimadzu 3-point bending SMWCNT multiscale composite flexural modulus and strength test.

new outlook on the expectation of physical performance in multiscale composites. Much has to be explored in the relationship of nanoscale materials in combination of macro- and microscale systems. LMWCNTs, at this point, do not significantly advance conventional composite's performance over SMWCNTs.

Acknowledgments

M. Zimmer acknowledges the support of Q. Cheng and S. Li for their technical advising on experiments. Thanks to J. Brooks for the expertise on the physics background related to the research. Many thanks to R. Liang, B. Wang, and

C. Zhang for the research advising, financial support, and knowledge provided throughout the term of the research.

References

[1] E. Bekyarova, E. T. Thostenson, A. Yu et al., "Multiscale carbon nanotube-carbon fiber reinforcement for advanced epoxy composites," *Langmuir*, vol. 23, no. 7, pp. 3970–3974, 2007.

[2] Y. H. Lu, M. S. Zhan, and W. H. Zheng, "Preparation and properties of T300 carbon fiber-reinforced thermoplastic polyimide composites," *Journal of Applied Polymer Science*, vol. 102, no. 1, pp. 646–654, 2006.

[3] H. Qian, A. Bismarck, E. S. Greenhalgh, G. Kalinka, and M. S. P. Shaffer, "Hierarchical composites reinforced with carbon nanotube grafted fibers: the potential assessed at the single fiber level," *Chemistry of Materials*, vol. 20, no. 5, pp. 1862–1869, 2008.

[4] V. K. Rangari, M. Yousuf, S. Jeelani, M. X. Pulikkathara, and V. N. Khabashesku, "Alignment of carbon nanotubes and reinforcing effects in nylon-6 polymer composite fibers," *Nanotechnology*, vol. 19, no. 24, Article ID 245703, 2008.

[5] S. Z. Shen, S. Bateman, Q. Yuan, M. Dell'Olio, J. Gotama, and D. Y. Wu, "Thermal properties and fire performance of woven glass fibre reinforced nylon 6 nano-composites with carbon nanotubes," *Advanced Materials Research*, vol. 32, pp. 9–12, 2008.

[6] Z. Fan, M. H. Santare, and S. G. Advani, "Interlaminar shear strength of glass fiber reinforced epoxy composites enhanced with multi-walled carbon nanotubes," *Composites Part A*, vol. 39, no. 3, pp. 540–554, 2008.

[7] T. Borca-Tasciuc, M. Mazumder, Y. Son, S. K. Pal, L. S. Schadler, and P. M. Ajayan, "Anisotropic thermal diffusivity characterization of aligned carbon nanotube-polymer composites," *Journal of Nanoscience and Nanotechnology*, vol. 7, no. 4-5, pp. 1581–1588, 2007.

[8] S. Wang, R. Liang, B. Wang, and C. Zhang, "Dispersion and thermal conductivity of carbon nanotube composites," *Carbon*, vol. 47, no. 1, pp. 53–57, 2009.

[9] W. T. Hong and N. H. Tai, "Investigations on the thermal conductivity of composites reinforced with carbon nanotubes," *Diamond and Related Materials*, vol. 17, no. 7–10, pp. 1577–1581, 2008.

[10] Q. Ngo, B. A. Cruden, A. M. Cassell et al., "Thermal conductivity of carbon nanotube composite films," in *Proceedings of the Materials Research Society Symposium*, vol. 812, pp. 179–184, April 2004.

[11] A. Moisala, Q. Li, I. A. Kinloch, and A. H. Windle, "Thermal and electrical conductivity of single- and multi-walled carbon nanotube-epoxy composites," *Composites Science and Technology*, vol. 66, no. 10, pp. 1285–1288, 2006.

[12] M. B. Bryning, D. E. Milkie, M. F. Islam, J. M. Kikkawa, and A. G. Yodh, "Thermal conductivity and interfacial resistance in single-wall carbon nanotube epoxy composites," *Applied Physics Letters*, vol. 87, no. 16, Article ID 161909, 3 pages, 2005.

[13] Y. A. Kim, S. Kamio, T. Tajiri et al., "Enhanced thermal conductivity of carbon fiber/phenolic resin composites by the introduction of carbon nanotubes," *Applied Physics Letters*, vol. 90, no. 9, Article ID 093125, 3 pages, 2007.

[14] L. Tong, X. Sun, and P. Tan, "Effect of long multi-walled carbon nanotubes on delamination toughness of laminated composites," *Journal of Composite Materials*, vol. 42, no. 1, pp. 5–23, 2008.

[15] C. Zweben, "Thermal materials solve power electronics challenges," *Power Electronics Technology*, vol. 32, no. 2, pp. 40–47, 2006.

[16] G. W. Lee, M. Park, J. Kim, J. I. Lee, and H. G. Yoon, "Enhanced thermal conductivity of polymer composites filled with hybrid filler," *Composites Part A*, vol. 37, no. 5, pp. 727–734, 2006.

[17] S. Han, J. T. Lin, Y. Yamada, and D. D. L. Chung, "Enhancing the thermal conductivity and compressive modulus of carbon fiber polymer-matrix composites in the through-thickness direction by nanostructuring the interlaminar interface with carbon black," *Carbon*, vol. 46, no. 7, pp. 1060–1071, 2008.

[18] I. Grigoriev and E. Melilikhov, *Handbook of Physical Quantities*, CRC Press, New York, NY, USA, 1997.

[19] G. Chen, "Phonon heat conduction in nanostructures," *International Journal of Thermal Sciences*, vol. 39, no. 4, pp. 471–480, 2000.

[20] J. Klett, A. D. Mcmillan, and N. C. Gallego, *The Role of Structure on the Thermal Properties of Graphite Foams*, Oak Ridge National Laboratory, 2007.

[21] J. Singh, *Excitation Energy Transfer Processes in Condensed Matter: Theory and Applications*, Plenum Press, New York, NY, USA, 1994.

[22] C. Kittel, *Introduction to Solid State Physics*, Wiley, New York, NY, USA, 5th edition, 1976.

[23] R. C. Zeller and R. O. Pohl, "Thermal conductivity and specific heat of noncrystalline solids," *Physical Review B*, vol. 4, no. 6, pp. 2029–2041, 1971.

[24] J. Bodzenta, "Influence of order-disorder transition on thermal conductivity of solids," *Chaos, Solitons and Fractals*, vol. 10, no. 12, pp. 2087–2098, 1999.

[25] R. S. Prasher, X. J. Hu, Y. Chalopin et al., "Turning carbon nanotubes from exceptional heat conductors into insulators," *Physical Review Letters*, vol. 102, no. 10, Article ID 105901, 4 pages, 2009.

[26] S. T. Huxtable, D. G. Cahill, S. Shenogin et al., "Interfacial heat flow in carbon nanotube suspensions," *Nature Materials*, vol. 2, no. 11, pp. 731–734, 2003.

[27] D. Cahill and R. Pohl, "Lattic vibrations and heat transport in crystals," *Annual Reviews*, vol. 39, pp. 93–121, 1988.

[28] K. Esfarjani, M. Zebarjadi, and Y. Kawazoe, "Thermoelectric properties of a nanocontact made of two-capped single-wall carbon nanotubes calculated within the tight-binding approximation," *Physical Review B*, vol. 73, no. 8, Article ID 085406, 6 pages, 2006.

[29] C. Yeh, *A study of nanostructure and properties of mixed nanotube buckypaper materials: fabrication, process modeling, characterization and property modeling [Ph.D. dissertation]*, Florida State University, Tallahassee, Fla, USA, 2007.

[30] E. Kymakis, I. Alexandou, and G. A. J. Amaratunga, "Single-walled carbon nanotube-polymer composites: electrical, optical and structural investigation," *Synthetic Metals*, vol. 127, no. 1–3, pp. 59–62, 2002.

[31] A. Buldum and J. P. Lu, "Contact resistance between carbon nanotubes," *Physical Review B*, vol. 63, no. 16, Article ID 161403, 3 pages, 2001.

[32] R. B. Mathur, S. Chatterjee, and B. P. Singh, "Growth of carbon nanotubes on carbon fibre substrates to produce hybrid/phenolic composites with improved mechanical properties," *Composites Science and Technology*, vol. 68, no. 7-8, pp. 1608–1615, 2008.

[33] J. Qiu, C. Zhang, B. Wang, and R. Liang, "Carbon nanotube integrated multifunctional multiscale composites," *Nanotechnology*, vol. 18, no. 27, Article ID 275708, 2007.

[34] R. J. Sager, P. J. Klein, D. C. Lagoudas et al., "Effect of carbon nanotubes on the interfacial shear strength of T650 carbon fiber in an epoxy matrix," *Composites Science and Technology*, vol. 69, no. 7-8, pp. 898–904, 2009.

Hindawi Publishing Corporation
Journal of Nanomaterials
Volume 2012, Article ID 749732, 10 pages
doi:10.1155/2012/749732

Research Article

Star Poly(*N*-isopropylacrylamide) Tethered to Polyhedral Oligomeric Silsesquioxane (POSS) Nanoparticles by a Combination of ATRP and Click Chemistry

Shiao-Wei Kuo,[1] Jing-Long Hong,[1] Yu-Chan Huang,[1] Jem-Kun Chen,[2] Shih-Kang Fan,[2] Fu-Hsiang Ko,[2] Chih-Wei Chu,[2] and Feng-Chih Chang[2]

[1] *Department of Materials and Optoelectronic Science, Center for Nanoscience and Nanotechnology, National Sun Yat-Sen University, Kaohsiung 804, Taiwan*
[2] *Institute of Applied Chemistry, National Chiao Tung University, Hsinchu 30010, Taiwan*

Correspondence should be addressed to Shiao-Wei Kuo, kuosw@faculty.nsysu.edu.tw

Received 7 January 2012; Accepted 21 February 2012

Academic Editor: Luis Antonio Sanchez de Almeida Prado

New star poly(*N*-isopropylacrylamide)-*b*-polyhedral oligomeric silsesquioxane (PNIPAm-*b*-POSS) copolymers were synthesized from octa-azido functionalized POSS (N_3-POSS) and alkyne-PNIPAm, which was prepared using an alkyne-functionalized atom transfer radical polymerization (ATRP) initiator (propargyl 2-bromo-2-methylpropionamide), via click chemistry. These star PNIPAm-*b*-POSS copolymers undergo a sharp coil-globule transition in water at above 32°C changing from a hydrophilic state below this temperature to a hydrophobic state above it, which is similar to linear PNIPAm homopolymers. More interestingly, we found that these star polymers exhibited strong blue photoluminescence in water above a lower critical solution temperature (LCST). This photoluminescence was likely due to the constrained geometric freedom and relatively rigid structure caused by intramolecular hydrogen bonding within the star PNIPAm polymers, which exhibit an intrinsic fluorescent behavior.

1. Introduction

The PNIPAm homopolymer undergoes a sharp coil-globule transition in water at 32°C, transitioning from a hydrophilic state below this temperature to a hydrophobic state above it [1–5]. The lower critical solution temperature (LCST) corresponds to the region in the phase diagram where the enthalpic contribution of the hydrogen bonds between water and the polymer chain is less than the entropic gain of the system as a whole and is largely dependent on the hydrogen-bonding capabilities of the constituent monomer units. Unlike hyperbranched polymers, star polymers also possess unique structures within the regular polymer branches as each polymer chain has only one branching point. Well-defined star polymers can be used as models to test theories about the influence of molecular structure on polymer properties [6–10].

POSS-containing copolymers have received increasing attention during the past decade as a novel category of nanoscale-structured materials for various applications [11], including liquid crystals [12], low-dielectric materials [13–16], nanocomposites [17], self-assembled structures [18–20], and photoresists in lithographic technology [21, 22], because of their thermal and mechanical properties. POSS is an inorganic Si_8O_{12} core that can be functionalized by attaching either seven inert organic hydrocarbon groups and a unique functional group or eight functional groups that are capable of polymerization or crosslinking [23–30]. It is in this latter regard that we have sought to develop star polymers consisting of well-defined PNIPAm functionalized cubic silsesquioxanes. PNIPAm/POSS nanocomposites have been widely reported in recent years [31–34]. For example, Zheng and colleagues have reported that PNIPAm/POSS nanocomposites were prepared through the reaction between the N–H group of PNIPAm and the epoxy group of octa(propylglycidyl ether)-POSS, swelled in water, and exhibited the characteristics of hydrogels [31]. These POSS-containing, hybrid hydrogels showed substantially faster swelling,

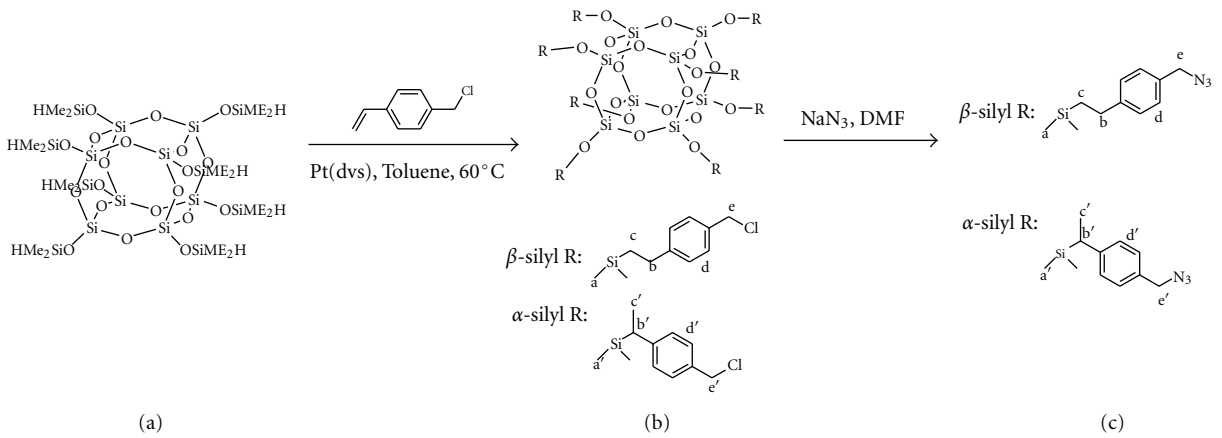

Scheme 1: Hydrosilylation of styrene monomers with (a) $Q_8M_8{}^H$ to give the (b) OVBC-POSS and the (c) N_3-POSS.

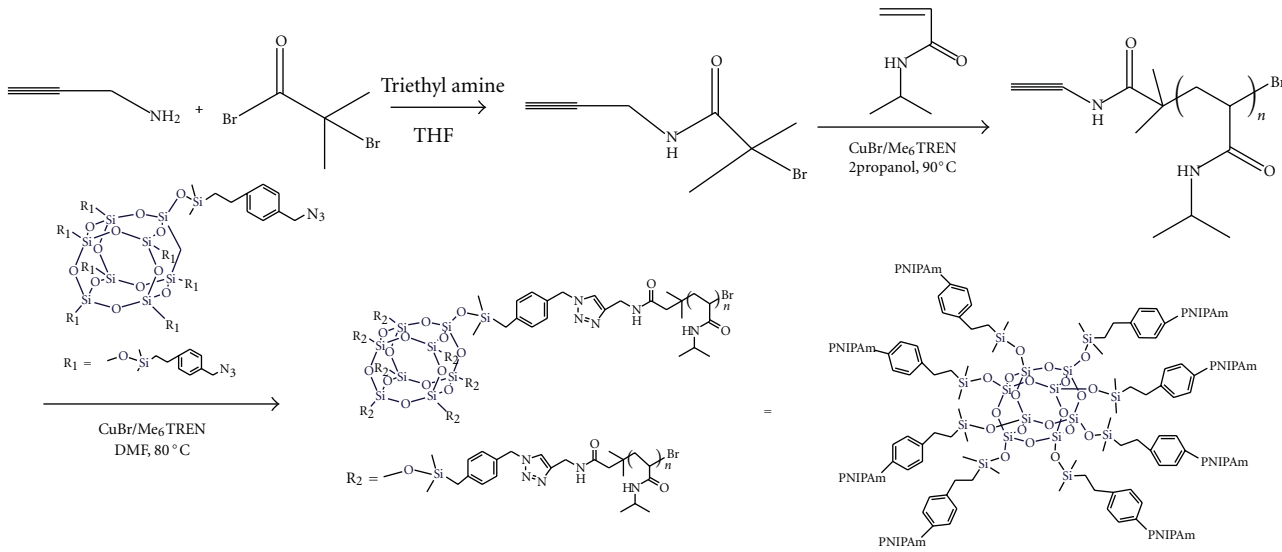

Scheme 2: The synthesis of the alkyne PNIPAm through ATRP and the click reaction to form star PNIPAm-*b*-POSS.

deswelling, and reswelling response rates than a control organic gel with a comparable degree of crosslinking. POSS; end-capped poly(ethylene oxide) was also incorporated into the crosslinked PNIPAm to form a physically interpenetrating polymer network [32]. Zhang et al. used a POSS-containing reversible addition fragmentation chain transfer (RAFT) agent in the RAFT polymerization of NIPAm to form a POSS-end-capped PNIPAm hybrid, which assembled into well-defined core/shell nanostructured micelles in solvents, with the average diameter of the micelles increasing with increasing molecular weight of the PNIPAm [34].

In this work, we prepared POSS nanoparticles functionalized with eight PNIPAm polymer chains through a combination of atom transfer radical polymerization (ATRP) and click chemistry. To the best of our knowledge, this is the first paper that reports the star PNIPAm-POSS polymers through combination of ATRP and click chemistry. First, we synthesize a multifunctional octa-azide POSS (N_3-POSS) molecule, shown in Scheme 1, [35, 36], and then clicked it to an alkyne-PNIPAm polymer, which had been prepared using an alkyne-terminal ATRP initiator as shown in Scheme 2. The molecular weight, chemical structure and photoluminescence properties of star PNIPAm-*b*-POSS were characterized in this study by gel permeation chromatography (GPC), Fourier transform infrared spectroscopy (FTIR), nuclear magnetic resonance (NMR) spectroscopy, and fluorescence spectroscopy (PL).

2. Experimental

2.1. Materials. Vinyl benzyl chloride (VBC), *N*,*N*-dimethylformamide, sodium azide (NaN_3), copper (I) bromide (CuBr, 98%), N, N, N', N'', N''-pentamethyldiethylenetriamine (PMDETA, 99%), and platinum complex (platinum-1,3-divinyltetramethyldisiloxane, Pt-dvs, 2 wt% Pt in xylene) were purchased from Aldrich, USA. Before use, the solution of the platinum complex was diluted 100-fold with xylene. Toluene was dried by distillation before using in

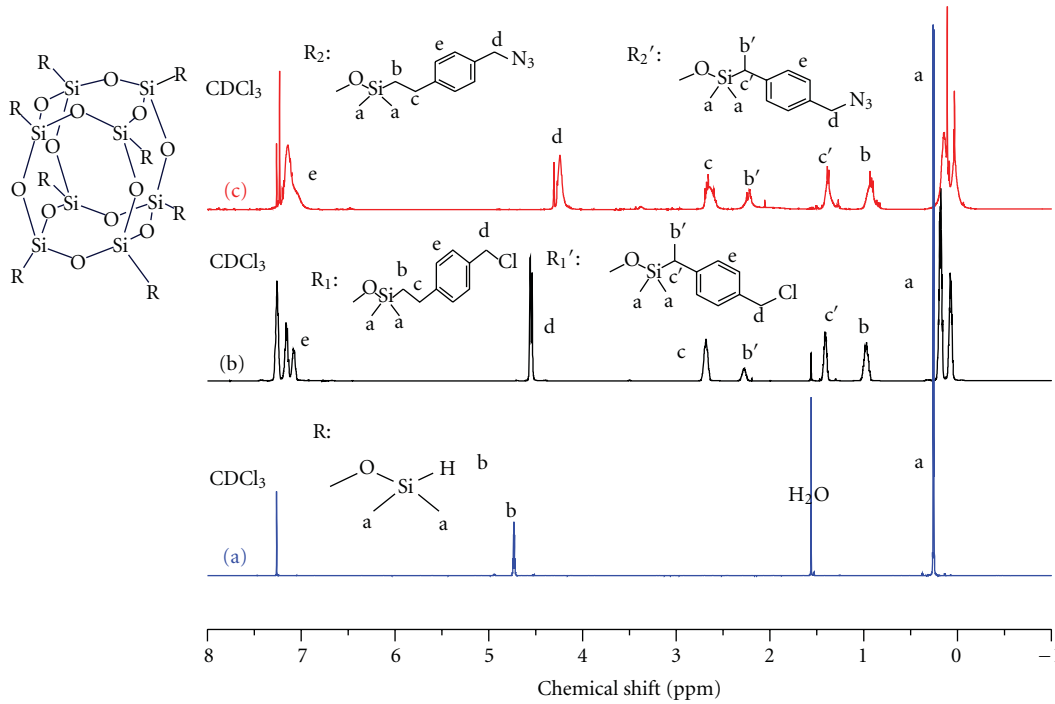

Figure 1: ^{1}H NMR spectra of (a) $Q_8M_8{}^{H}$, (b) OVBC-POSS, and (c) N_3-POSS in $CDCl_3$.

the hydrosilylation reaction. Octakis(dimethylsiloxy)silsesquioxane ($Q_8M_8{}^{H}$) containing eight hydrosilane groups was purchased from the Hybrid Plastics Co., USA. *N*-isopropylacrylamide (NIPAm) monomer was obtained from the Tokyo Chemical Industrial CO., Ltd. The NIPAm monomer was recrystallized from hexanes and dried in vacuum prior to use. Hexamethylated tris(2-(dimethylamino)ethyl)amine (Me_6TREN) was synthesized according to the method by Ciampolini and Nardi [37]. Propargyl 2-bromo-2-methylpropionamide was prepared according to the literature procedure [2, 3].

2.2. Synthesis of N_3-POSS [35, 36]. N_3-POSS was synthesized by reacting OVBC-POSS with sodium azide (NaN_3) as shown in Scheme 1. The OVBC-POSS was prepared by mixing $Q_8M_8{}^{H}$ (1 g, 0.98 mmol) with vinyl-benzyl-chloride (1.20 g, 7.86 mmol) in toluene (50 mL) while heating at 60°C under argon and then adding Pt(dvs) (0.07 mL, 0.13 mmol) via syringe. After stirring for 4 h, the Pt(dvs) catalyst was removed by filtering through activated charcoal; subsequent removal of the solvent via rotary evaporation yielded a viscous liquid. The chemical structure of the OVBC-POSS was determined using ^{29}Si NMR spectroscopy and possessed two peaks, one each for $(CH_3)_2$Si–H and Si–O–Si$(CH_3)_2$H at −2.1 and 109.3 ppm, respectively. In addition, the ^{29}Si NMR spectrum had three peaks at 10.28, 12.16, and −109.2 ppm corresponding to $(CH_3)_2$Si–$(CHCH_3)$, $(CH_3)_2$Si–CH_2–CH_2–, and Si–O–Si$(CH_3)_2$H, respectively. The chemical shifts clearly indicate that the hydrosilylation reaction went to completion under the reaction conditions. In a typical synthesis of N_3-POSS, OVBC-POSS (1 g, 0.45 mmol), NaN_3 (1.01 g, 15.4 mmol), and anhydrous DMF (50 mL) were added to a flask and heated at 120°C for 48 h. The solvents were then concentrated, and the residue was dissolved in THF. The sodium salts were removed by running through a neutral alumina column. A yellowish viscous liquid was obtained after drying in a vacuum oven overnight at room temperature.

2.3. Synthesis of Alkyne-PNIPAm [38]. A 100 mL dried Schlenk flask containing a magnetic stirrer bar was charged with CuBr (14.3 mg, 0.1 mmol) and NIPAM (1.35 g, 12 mmol). After filling the flask with argon, IPA (3 mL) was added, and the solution was stirred for 10 min at room temperature. The mixture was degassed three times using a freeze-pump-thaw cycle and then vigorously stirred at 0°C. After complete degassing, Me_6TREN (23.0 mg; 0.1 mmol) was injected into the solution with a syringe. After 10 minutes, the desired amount of propargyl 2-bromo-2-methylpropionamide was injected into the solution to initiate the reaction. The mixture was heated at 50°C for 12 h and then evaporated to dryness under vacuum. The residue was diluted with THF and then passed through an alumina column to remove the copper catalyst. The product was precipitated from ether three times and dried under vacuum overnight at room temperature to obtain the polymer as a white powder.

2.4. Synthesis of Star PNIPAm-b-POSS Copolymers. N_3-POSS (0.0115 g), alkyne-PNIPAm (0.5 g), and CuBr (3.5 mg, 0.025 mmol) were dissolved in DMF (20 mL) in a flask equipped with a magnetic stir bar. After one freeze-thaw-pump cycle, PMDETA (5.2 μL, 0.025 mmol) was added, and the reaction mixture was carefully degassed using three freeze-thaw-pump cycles, placed in an oil bath thermostated

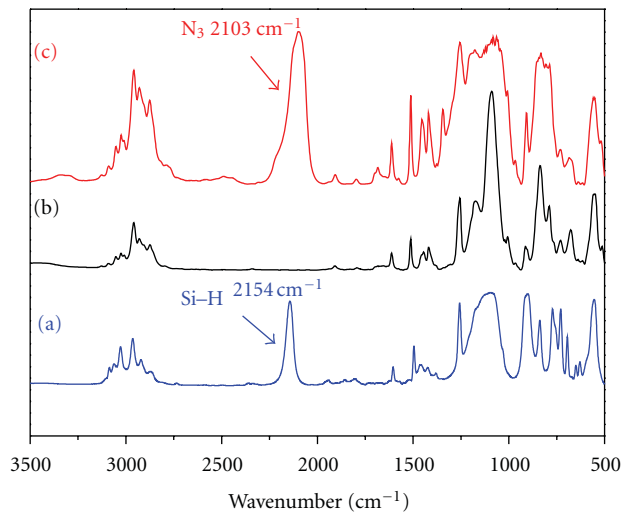

FIGURE 2: FTIR spectra of (a) $Q_8M_8{}^H$, (b) OVBC-POSS, and (c) N_3-POSS recorded at room temperature.

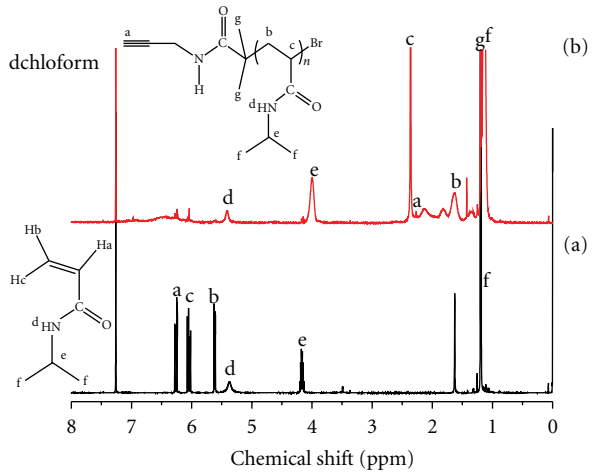

FIGURE 3: ^{1}H NMR spectra of (a) NIPAm monomer and (b) alkyne-PNIPAm in $CDCl_3$.

at 60°C and stirred for 24 h. After removing all of the solvents at reduced pressure, the residue was dissolved in CH_2Cl_2 and passed through a neutral alumina column to remove the copper catalyst. The star PNIPAm-*b*-POSS was obtained as a dark powder.

2.5. Characterizations. Using $CDCl_3$ as the solvent, ^{1}H NMR spectra were recorded on a Varian Unity Inova 500 FT NMR spectrometer operated at 500 MHz; chemical shifts are reported in parts per million (ppm). The molecular weight and molecular weight distribution were determined through gel permeation chromatography (GPC) using a Waters 510 HPLC equipped with a 410 differential refractometer, a refractive index (RI) detector, and three Ultrastyragel columns (100, 500, and 10^3 Å) connected in series in order of increasing pore size (eluent: DMF, flow rate: 0.6 mL/min). The FT-IR spectra of the samples in KBr disks were measured using a Nicolet Avatar 320 FT-IR spectrometer and collecting 32 scans at a resolution of 1 cm^{-1} after the sample chamber

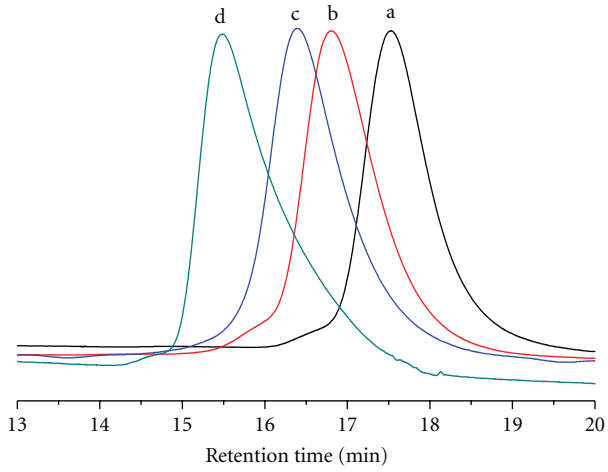

FIGURE 4: GPC traces of the molecular weight for the alkyne-PNIPA (a) 3100, (b) 5100, (c) 6300, and (d) 10100 g/mol.

had been purged with nitrogen to maintain the film's dryness. Thermal analysis was carried out using a DSC instrument (TA Instruments Q-20). The sample (ca. 4–6 mg) was weighed and sealed in an aluminum pan, and the measurement was obtained using a scan rate of 20°C/min and a temperature range of 25 to 200°C. The glass transition temperature (T_g) was taken as the midpoint of the heat capacity transition between the upper and lower points of deviation in the extrapolated glass and liquid lines. Dynamic Light Scattering (DLS) measurements were performed using a Brookhaven 90 plus Particle Size Analyzer (Brookhaven Instruments Corporation, USA) equipped with a 35 mW, 632.8 nm He-Ne laser. The temperature was controlled by the heating and cooling process, and the measurements were obtained at a 90° angle. Photoluminescence (PL) excitation and emission spectra were collected at room temperature using a monochromatized Xe light source.

3. Results and Discussion

3.1. Synthesis of N_3-POSS. The peaks for the Si–H protons (4.7 ppm) in Figure 1(a) disappeared in the spectrum of OVBC-POSS, which indicates that the hydrosilylation reaction went to completion. The spectrum in Figure 1(b) indicates that the vinyl groups of the VBC underwent hydrosilylation with the Si–H bonds of the $Q_8M_8{}^H$ in both the α and β configurations; that is, a mixture of these two orientations exists. The complete substitution of the chloride atoms by the azido groups was confirmed by the ^{1}H NMR spectrum, shown in Figure 1(c). After the substitution reaction, the resonance of the benzyl CH_2 connected to the chloride atoms shifted upfield, from 4.50 to 4.31 ppm [35, 36]. The complete loss of the resonance at 4.50 ppm suggests that the substitution reaction went to completion under the reaction conditions. Figure 2 presents the FTIR spectra of $Q_8M_8{}^H$, OVBC-POSS, and N_3-POSS. The strong absorption peak in all compounds around 1100 cm^{-1} represents the siloxane Si–O–Si vibration and is a general feature of POSS derivatives. The characteristic stretching vibrations for the Si–H group appeared as the peak at 2200 cm^{-1}, as shown

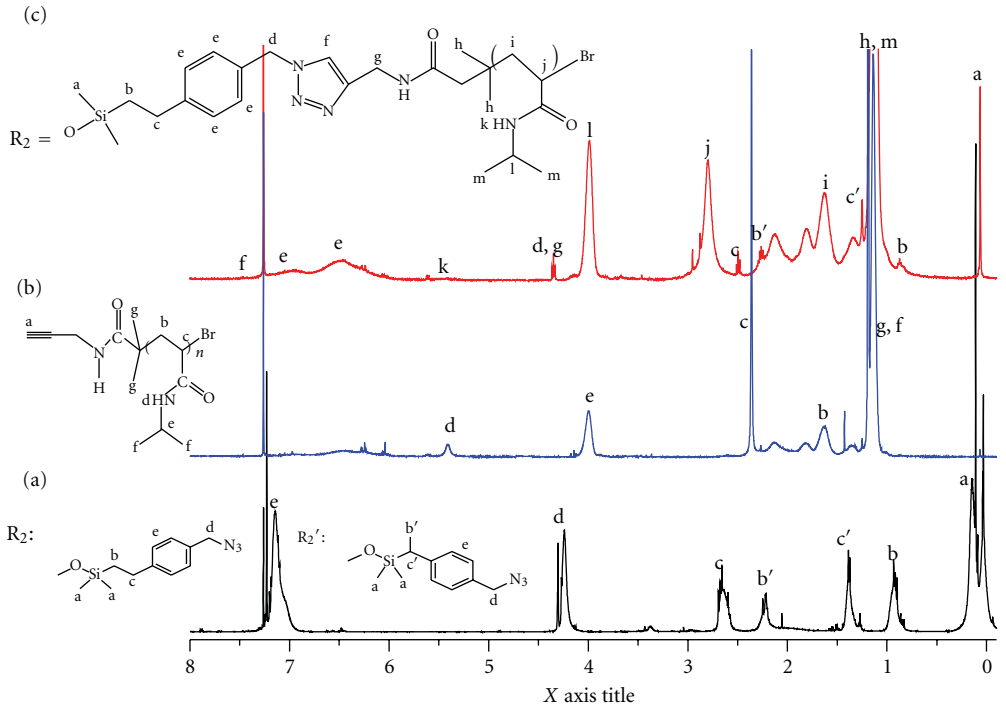

Figure 5: ^{1}H NMR spectra of (a) N_3-POSS, (b) alkyne-PNIPAm, and (c) star PNIPAm-*b*-POSS in $CDCl_3$.

in Figure 2(a). In the spectrum for OVBC-POSS, this peak disappeared completely, which indicates that the reaction reached completion. The N_3-POSS clearly showed a peak at 2096 cm^{-1}, indicative of the presence of azido groups, after the substitution reaction, as shown in Figure 2(c). All results based on the ^{1}H NMR and FTIR analyses were indicative of the successful synthesis of N_3-POSS.

3.2. Synthesis of Alkyne-PNIPAm. The alkyne-terminated PNIPAm was prepared using an alkyne functionalized ATRP initiator (propargyl 2-bromo-2-methylpropionamide). Figure 3(a) shows the peaks for the vinyl NIPAm monomer (ca. 5.61, 6.04, and 6.25 ppm), which disappear completely after chain extension via ATRP. The other alkyl CH and CH_2 protons in the NIPAm monomer appeared as multiplets at 4.17 and 1.17 ppm, respectively, while the singlet at 5.37 ppm belonged to the proton on the amide nitrogen atom. These three peaks remained in the spectrum for the alkyne-PNIPAm, as shown in Figure 3(b). The singlet at 2.25 ppm corresponds to the C≡C–H while the alkyl CH and CH_2 on the alkyne-PNIPAm main chain were located between 1.60 and 2.34 ppm, respectively. The GPC curves of alkyne-PNIPAm synthesized from different monomer/initiator ratios are both symmetrical and monomodal, as shown in Figure 4. The molecular weight increases with increasing monomer/initiator ratios, which is consistent with the principles of ATRP. Furthermore, the PDI of the alkyne-PNIPAm is narrow, which indicates successful chain extension of the PNIPAm through ATRP. These results are summarized in Table 1.

3.3. The Synthesis and Thermoresponsive Properties of Star PNIPAm-b-POSS Copolymers. The azide/alkyne click reaction was performed at 0°C over 24 h using CuBr/PMDETA as a catalyst and DMF as the solvent and was confirmed with ^{1}H, ^{13}C NMR and FTIR [39]. The peak assignments of N_3-POSS and alkyne-PNIPAm have been shown in Figures 1 and 3. In addition, the peaks of star PNIPAm-*b*-POSS are assigned in Figure 5(c). Because the molecular weight of the PNIPAm was very low, the proton signals of the POSS are clearly displayed in Figure 5(c). With the exception of the overlapping proton signals around 1.63 and 2.80 ppm, the PNIPAm peaks are easily identified. The resonance of the benzyl CH_2 connected to the azide in the N_3-POSS shifted downfield, from 4.23 to 4.38 ppm, in the star PNIPAm-*b*-POSS spectrum. In addition, the methyl (CH_3) attached to the silicone atom was found at 0.04 ppm from N_3-POSS, which also indicates the synthesis of star PNIPAm-*b*-POSS was successful. The click reaction was also characterized by ^{13}C NMR, as shown in Figure 6. The carbonyl and amide carbon signals in the star PNIPAm-*b*-POSS spectrum appeared at 174 and 170 ppm, respectively, while the phenyl rings showed up at 126 and 128 ppm. Clearly, the alkyne carbon signal at 81.0 ppm in the alkyne-PNIPAm spectrum disappeared in the star PNIPAm-*b*-POSS spectrum. The peak at 143.5 ppm is from the carbon of the triazole structures

Table 1: Molecular characterization of the alkyne-PNIPAm homopolymer during ATRP.

	Monomer : initiator	M_w [a]	M_n [a]	PDI[a]	T_g [b]
PNIPAM1	200 : 1	11700	10100	1.15	140
PNIPAM2	100 : 1	7300	6300	1.16	141
PNIPAM3	80 : 1	5700	5100	1.12	140
PNIPAM4	50 : 1	3600	3100	1.14	112

[a] Polydispersity index and molecular weight, measured by GPC. [b] Obtained from DSC by 20°C/min.

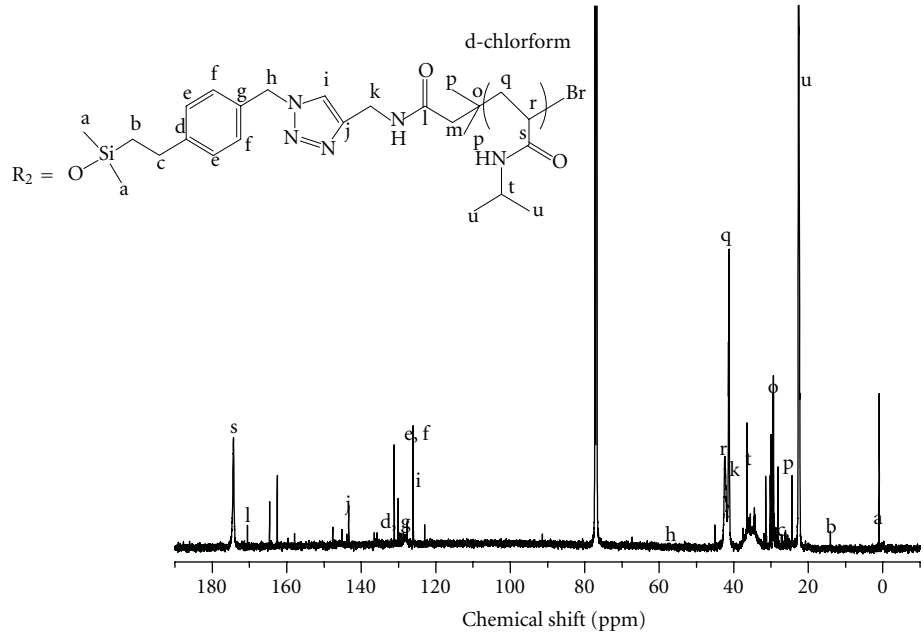

Figure 6: ^{13}C NMR spectrum of star PNIPAm-*b*-POSS in $CDCl_3$.

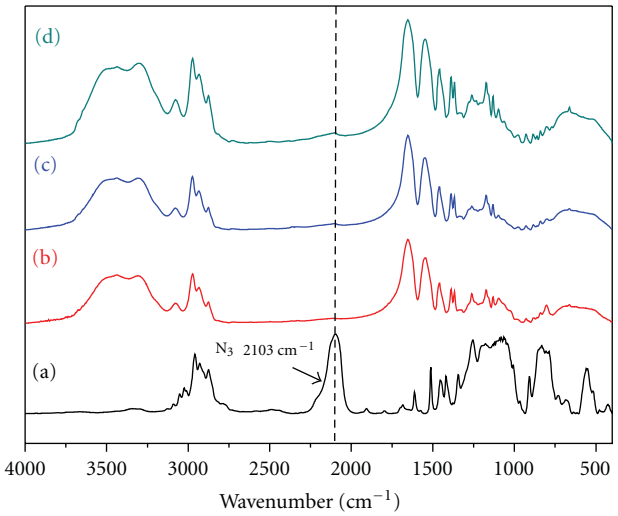

Figure 7: FTIR spectra of (a) N_3-POSS, (b) PNIPAm (3.1 k)-*b*-POSS, (c) PNIPAm (6.3 k)-*b*-POSS, and (d) PNIPAm (10.1 k)-*b*-POSS.

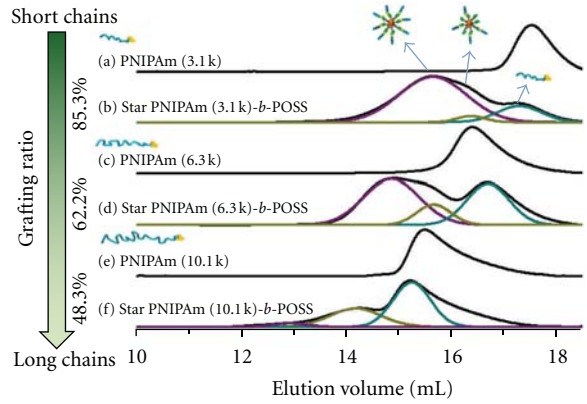

Figure 8: GPC traces of (a) alkyne-PNIPAm and (b) star PNIPAm (3.1 k)-*b*-POSS.

formed by the click reaction. The peaks for the N_3-POSS methyl and methylene carbons remained at 0.2 ppm and 14.0 ppm, respectively, in the star PNIPAm-*b*-POSS spectrum. All other carbon signals for the star PNIPAm-*b*-POSS are assigned in Figure 6. The complete disappearance of the characteristic FTIR signals for the azide and acetylene groups is shown in Figure 7. The peak at 2100 cm^{-1}, which corresponds to the azide in N_3-POSS, completely disappeared from the spectrum for the star PNIPAm-*b*-POSS copolymers while the characteristic Si–O–Si (siloxane) absorption for POSS, which appears at 1100 cm^{-1}, remained. These results indicate that all the azide and acetylene functionalities participated in the click reaction [30, 39]. In addition, the FTIR spectra in Figure 7 show the appearance of two new peaks at 1653 and 1550 cm^{-1}, which corresponds to the stretching vibration of the amide I and amide II groups of the PNIPAm in the star PNIPAm-*b*-POSS copolymers. The GPC trace of the star PNIPAm-*b*-POSS block copolymer obtained after the click reaction is shown in Figure 8. Block copolymers prepared from the alkyne-PNIPAm resulted in products nearly devoid of the alkyne-PNIPAm peak and with lower retention times, which supports the formation of star PNIPAm-*b*-POSS copolymers. Because of the clear separation between ungrafted PNIPMm peas and the star PNIPAm-b-POSS copolymer, we are able to quantify the contents of grafted PNIPAm ratios. On the GPC traces, the peaks at shorter and longer retention times in each GPC trace corresponded to the elution of the full PNIPAm-b-POSS and partial PNIPAm-b-POSS as shown in Figure 8(b) and

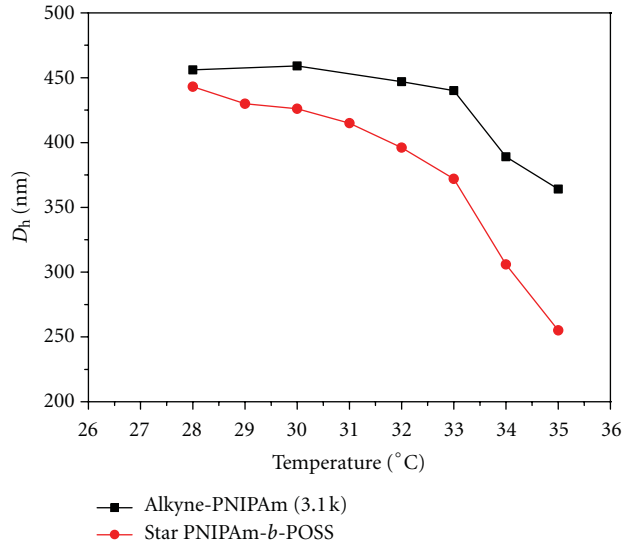

Figure 9: Variation of the average hydrodynamic diameter (D_h) with the temperature of the alkyne-PNIPAm and the star PNIPAm-*b*-POSS.

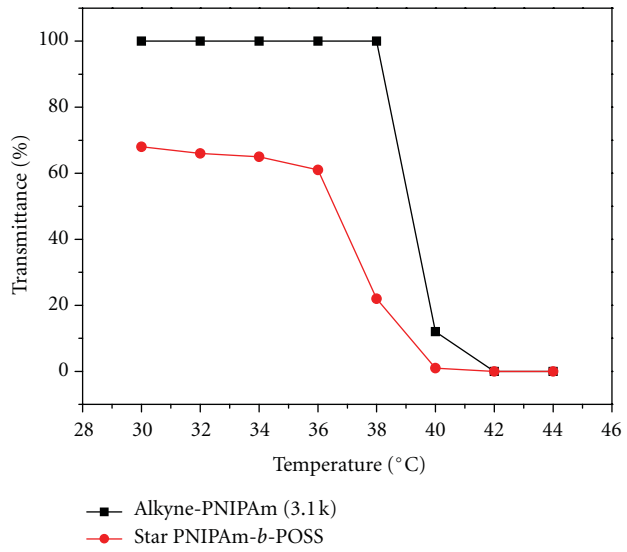

Figure 10: Transmittance versus temperature of the alkyne-PNIPAm and the star PNIPAm-*b*-POSS.

smaller ungrafted alkyne-PNIPAm, respectively. The ratio of grafted PNIPAm was determined by comparing the grafted PNIPAm peak ratio after using Gaussian fitting. Comparing the different chain length of the alkyne-PNIPAm to POSS provides an indication that the polymer's molecular weight has an influence on the grafted ratio of the star PNIPAm-*b*-POSS copolymers. Clearly, as the molecular weight of PNIPAm is increased, the graft ratio is decreased (85.3 to 48.3%). This result can be explained by the decreased reactivity of the chain-end alkyne functionality that becomes less accessible as the polymer adopts a more random coil structure at high molecular weight [40]. All of the results from the ^{1}H NMR, ^{13}C NMR, FTIR, and GPC analyses indicated that the synthesis of star PNIPAm-*b*-POSS was successful.

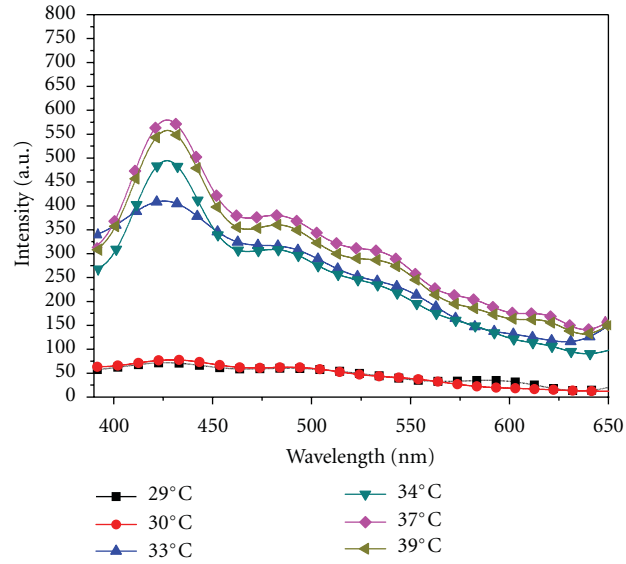

Figure 11: PL spectra of the alkyne-PNIPAm with increasing temperature.

Dynamic light scattering (DLS) was employed to determine both the hydrodynamic diameter ($\langle D_h \rangle$) of the alkyne-PNIPAm and star PNIPAm-*b*-POSS and their temperature-responsive behavior. As shown in Figure 9, increasing the temperature from 26 to 36°C decreased the average hydrodynamic diameter of pure alkyne-PNIPAm from 460 to 340 nm and star PNIPAm-*b*-POSS copolymers from 440 nm to 200 nm, which corresponds to the "deswelling" states of PNIPAm [1, 5]. Both the linear and star PNIPAm clearly displayed dimensional change with temperature, implying that the volumes of these PNIPAm polymers can shrink or swell with changing temperature. Most importantly, the size dependence of the PNIPAm during the heating process coincides reversibly with that during the cooling process. Therefore, after a cycle of temperature increases and decreases, the hydrodynamic diameter returns to its starting value [1]. In addition, the star PNIPAm-*b*-POSS copolymer has a lower hydrodynamic diameter than the linear alkyne-PNIPAm, indicating that the star polymers can collapse into a denser globule as a result of the star architecture [41]. Also, pure alkyne-PNIPAm homopolymers are highly water soluble at temperatures below 38°C. The transparent aqueous alkyne-PNIPAm solution becomes opaque above a specific temperature, as shown in Figure 10, and becomes transparent again when the temperature decreases, which corresponds to a reversible phase transition. The star PNIPAm-*b*-POSS copolymer had lower transmittance than the linear alkyne-PNIPAm since the POSS and benzyl functional groups are not water soluble, which would decrease their transmittance; however, it also had a similar phase transition to the pure alkyne-PNIPAm at ca. 38°C. Scheme 3 shows the possible phase transitions of star PNIPAm-*b*-POSS with increasing temperature. The random coils of the star PNIPAm chains first collapse to form a dense globule at ca. 32°C and then phase separated from the aqueous solution at ca. 38°C. We found that the LCST increased with decreasing molecular

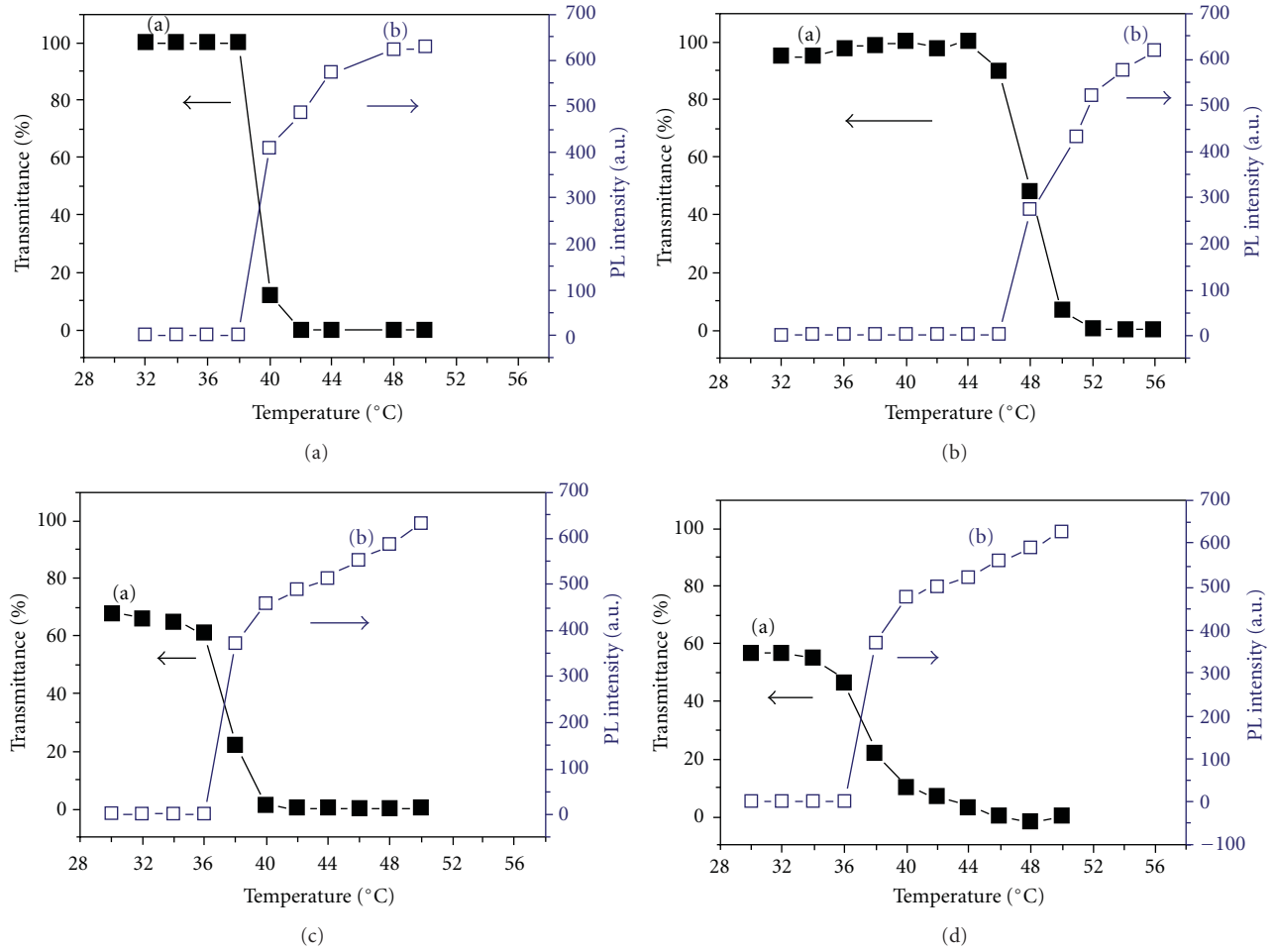

Figure 12: Transmittance and PL intensity with increasing temperature of the (a) alkyne-PNIPAm (10.1 k), (b) alkyne-PNIPAm (3.1 k), (c) star PNIPAm (10.1 k)-*b*-POSS, and (d) star PNIPAm (3.1 k)-*b*-POSS.

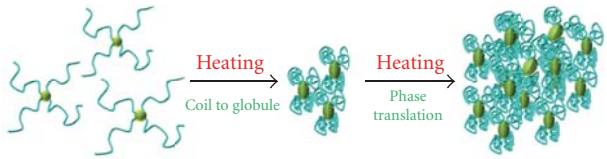

Scheme 3: The possible phase transitions of the star PNIPAm-*b*-POSS with increasing temperature.

weight for both the alkyne-PNIPAm and the star PNIPAm-*b*-POSS because the low molecular weight is more difficult to phase-separate due to entropy constraints.

Figure 11 shows the PL spectra of the alkyne-PNIPAm with increasing temperature. Clearly, no emission was observed below 32°C while a high-intensity emission appeared above 32°C, which means that the aggregation of the PNIPAm chain could enhance the emission properties of the material. Figure 12 summarizes the transmittance and PL intensity of the alkyne-PNIPAm and the star PNIPAm-*b*-POSS with increasing temperature. The transmittance clearly decreases with increasing temperature, which would enhance the PL intensity of the PNIPAm polymers. Because no traditional fluorophores are present in the PNIPAm main chain, their fluorescence was unexpected. This interesting phenomenon has already been reported by some groups [42–52]. Wu et al. reported hyperbranched poly(amino ester) could also emit blue photoluminescence without oxidation or protonation and proposed that the coexistence of tertiary amine and carbonyl groups in the core was the key structural factor in inducing fluorescence [51]. Lin et al. reported that the fluorescence properties of HPEA were due to the relationship of its three-dimensional structure, but the linear polymer failed to show any fluorescence [52], and the mechanism is still unresolved. They proposed that the hyperbranched polymers are highly cascaded with three-dimensional globular architectures, which is similar to PNIPAm above the LCST in this study. We believe that the intramolecular hydrogen-bonding interaction between the amide hydrogen and carbonyl in PNIPAm above the LCST is also an important phenomenon, and the aggregation of the PNIPAm chain could enhance the emission properties. In addition, a protic solvent-like water can act as a hydrogen-bonding donor for the interior oxygen atoms and stabilize the molecular conformation [52]. Due to the constrained

geometric freedom and relatively rigid structure above the LCST, these star polymers exhibit an intrinsic fluorescent behavior.

4. Conclusions

The molecular weight, chemical structure, and photoluminescence properties of star PNIPAm-*b*-POSS copolymers are characterized by GPC, FTIR, and NMR and indicate that we have successfully synthesized a novel octa-functionalized PNIPAm POSS (PNIPAm-*b*-POSS) from N_3-POSS and alkyne-PNIPAm via click chemistry. More interestingly, we found that these star polymers exhibited strong blue photoluminescence in water when above a lower critical solution temperature (LCST). This photoluminescence was likely due to the constrained geometric freedom and relative rigid structure caused by intramolecular hydrogen bonding within the star PNIPAm dentritic polymers, which exhibit an intrinsic fluorescent behavior.

Acknowledgments

This work was supported financially by the National Science Council, Taiwan, under Contract no. NSC 100-2221-E-110-029-MY3 and NSC 100-2628-E-110-001. The authors do not have a direct financial relation with POSS, Hybrid Plastics Co., USA, Tokyo Chemical Industrial Co., and Brookhaven Instruments Corporation that might lead to a conflict of interests for any of the authors.

References

[1] H. K. Fu, S. W. Kuo, C. F. Huang, F. C. Chang, and H. C. Lin, "Preparation of the stimuli-responsive ZnS/PNIPAM hollow spheres," *Polymer*, vol. 50, no. 5, pp. 1246–1250, 2009.

[2] C. J. Huang and F. C. Chang, "Using click chemistry to fabricate ultrathin thermoresponsive microcapsules through direct covalent layer-by-layer assembly," *Macromolecules*, vol. 42, no. 14, pp. 5155–5166, 2009.

[3] C. J. Huang and F. C. Chang, "Polypeptide diblock copolymers: syntheses and properties of poly(N-isopropylacrylamide)-b-polylysine," *Macromolecules*, vol. 41, no. 19, pp. 7041–7052, 2008.

[4] H. Ringsdorf, J. Venzmer, and F. M. Winnik, "Fluorescence studies of hydrophobically modified poly(N-isopropylacrylamides)," *Macromolecules*, vol. 24, no. 7, pp. 1678–1686, 1991.

[5] P. Kujawa, F. Tanaka, and F. M. Winnik, "Temperature-dependent properties of telechelic hydrophobically modified poly(N-isopropylacrylamides) in water: evidence from light scattering and fluorescence spectroscopy for the formation of stable mesoglobules at elevated temperatures," *Macromolecules*, vol. 39, no. 8, pp. 3048–3055, 2006.

[6] C. F. Huang, H. F. Lee, S. W. Kuo, H. Xu, and F. C. Chang, "Star polymers via atom transfer radical polymerization from adamantane-based cores," *Polymer*, vol. 45, no. 7, pp. 2261–2269, 2004.

[7] C. F. Huang, S. W. Kuo, H. C. Lin et al., "Thermal properties, miscibility and specific interactions in comparison of linear and star poly(methyl methacrylate) blend with phenolic," *Polymer*, vol. 45, no. 17, pp. 5913–5921, 2004.

[8] J. Xia, X. Zhang, and K. Matyjaszewski, "Synthesis of star-shaped polystyrene by atom transfer radical polymerization using an "arm first" approach," *Macromolecules*, vol. 32, no. 13, pp. 4482–4484, 1999.

[9] H. Gao and K. Matyjaszewski, "Synthesis of star polymers by a combination of ATRP and the "click" coupling method," *Macromolecules*, vol. 39, no. 15, pp. 4960–4965, 2006.

[10] W. Zhang and A. H. E. Müller, "A "click chemistry" approach to linear and star-shaped telechelic POSS-containing hybrid polymers," *Macromolecules*, vol. 43, no. 7, pp. 3148–3152, 2010.

[11] S.-W. Kuo and F.-C. Chang, "POSS related polymer nanocomposites," *Progress in Polymer Science*, vol. 36, no. 12, pp. 1649–1696, 2011.

[12] Q. Pan, X. Chen, X. Fan, Z. Shen, and Q. Zhou, "Organic-inorganic hybrid bent-core liquid crystals with cubic silsesquioxane cores," *Journal of Materials Chemistry*, vol. 18, no. 29, pp. 3481–3488, 2008.

[13] Y. J. Lee, J. M. Huang, S. W. Kuo, and F. C. Chang, "Low-dielectric, nanoporous polyimide films prepared from PEO-POSS nanoparticles," *Polymer*, vol. 46, no. 23, pp. 10056–10065, 2005.

[14] B. H. Yang, H. Y. Xu, Z. Z. Yang, and X. Y. Liu, "Design and architecture of low-dielectric-constant organic-inorganic hybrids from octahydridosilsesquioxanes," *Journal of Materials Chemistry*, vol. 19, no. 47, pp. 9038–9044, 2009.

[15] Y. L. Liu and M. H. Fangchiang, "Polyhedral oligomeric silsesquioxane nanocomposites exhibiting ultra-low dielectric constants through POSS orientation into lamellar structures," *Journal of Materials Chemistry*, vol. 19, no. 22, pp. 3643–3647, 2009.

[16] Y. J. Lee, J. M. Huang, S. W. Kuo, J. S. Lu, and F. C. Chang, "Polyimide and polyhedral oligomeric silsesquioxane nanocomposites for low-dielectric applications," *Polymer*, vol. 46, no. 1, pp. 173–181, 2005.

[17] T. Hirai, M. Leolukman, T. Hayakawa, M. A. Kakimoto, and P. Gopalan, "Hierarchical nanostructures of organosilicate nanosheets within self-organized block copolymer films," *Macromolecules*, vol. 41, no. 13, pp. 4558–4560, 2008.

[18] C. H. Lu, J. H. Wang, F. C. Chang, and S. W. Kuo, "Star block copolymers through nitroxide-mediated radical polymerization from polyhedral oligomeric silsesquioxane (POSS) core," *Macromolecular Chemistry and Physics*, vol. 211, no. 12, pp. 1339–1347, 2010.

[19] C. H. Lu, S. W. Kuo, W. T. Chang, and F. C. Chang, "The self-assembled structure of the diblock copolymer PCL-b-P4VP transforms upon competitive interactions with octaphenol polyhedral oligomeric silsesquioxane," *Macromolecular Rapid Communications*, vol. 30, no. 24, pp. 2121–2127, 2009.

[20] W. B. Zhang, B. Sun, H. Li et al., "Synthesis of in-chain-functionalized polystyrene-block-poly(dimethylsiloxane) diblock copolymers by anionic polymerization and hydrosilylation using dimethyl-4-(1-phenylvinyl)phenylsilane," *Macromolecules*, vol. 42, no. 19, pp. 7258–7262, 2009.

[21] Y. Ni and S. Zheng, "A novel photocrosslinkable polyhedral oligomeric silsesquioxane and its nanocomposites with poly(vinyl cinnamate)," *Chemistry of Materials*, vol. 16, no. 24, pp. 5141–5148, 2004.

[22] H. M. Lin, S. Y. Wu, P. Y. Huang, C. F. Huang, S. W. Kuo, and F. C. Chang, "Polyhedral oligomeric silsesquioxane containing copolymers for negative-type photoresists," *Macromolecular Rapid Communications*, vol. 27, no. 18, pp. 1550–1555, 2006.

[23] H. Xu, S. W. Kuo, J. S. Lee, and F. C. Chang, "Preparations, thermal properties, and Tg increase mechanism of

inorganic/organic hybrid polymers based on polyhedral oligomeric silsesquioxanes," *Macromolecules*, vol. 35, no. 23, pp. 8788–8793, 2002.

[24] H. Xu, S. W. Kuo, J. S. Lee, and F. C. Chang, "Glass transition temperatures of poly(hydroxystyrene-co-vinylpyrrolidone-co-isobutylstyryl polyhedral oligosilsesquioxanes)," *Polymer*, vol. 43, no. 19, pp. 5117–5124, 2002.

[25] Y. C. Sheen, C. H. Lu, C. F. Huang, S. W. Kuo, and F. C. Chang, "Synthesis and characterization of amorphous octakis-functionalized polyhedral oligomeric silsesquioxanes for polymer nanocomposites," *Polymer*, vol. 49, no. 18, pp. 4017–4024, 2008.

[26] S. W. Kuo, H. F. Lee, W. J. Huang, K. U. Jeong, and F. C. Chang, "Solid state and solution self-assembly of helical polypeptides tethered to polyhedral oligomeric silsesquioxanes," *Macromolecules*, vol. 42, no. 5, pp. 1619–1626, 2009.

[27] S. W. Kuo, Y. C. Wu, C. H. Lu, and F. C. Chang, "Surface modification of gold nanoparticles with polyhedral oligomeric silsesquioxane and incorporation within polymer matrices," *Journal of Polymer Science B*, vol. 47, no. 8, pp. 811–819, 2009.

[28] K. W. Huang, L. W. Tsai, and S. W. Kuo, "Influence of octakis-functionalized polyhedral oligomeric silsesquioxanes on the physical properties of their polymer nanocomposites," *Polymer*, vol. 50, no. 20, pp. 4876–4887, 2009.

[29] R. S. Shih, C. H. Lu, S. W. Kuo, and F. C. Chang, "Hydrogen bond-mediated self-assembly of polyhedral oligomeric silsesquioxane-based supramolecules," *Journal of Physical Chemistry C*, vol. 114, no. 30, pp. 12855–12862, 2010.

[30] Y.-C. Lin and S.-W. Kuo, "Self-assembly and secondary structures of linear polypeptides tethered to polyhedral oligomeric silsesquioxane nanoparticles through click chemistry," *Journal of Polymer Science A*, vol. 49, no. 10, pp. 2127–2137, 2011.

[31] J. Mu and S. Zheng, "Poly(N-isopropylacrylamide) nanocrosslinked by polyhedral oligomeric silsesquioxane: temperature-responsive behavior of hydrogels," *Journal of Colloid and Interface Science*, vol. 307, no. 2, pp. 377–385, 2007.

[32] K. Zeng, L. Wang, and S. Zheng, "Rapid deswelling and reswelling response of poly(*N*-isopropylacrylamide) hydrogels via formation of interpenetrating polymer networks with polyhedral oligomeric silsesquioxane-capped polyethylene oxide amphiphilic telechelics," *Journal of Physical Chemistry B*, vol. 113, no. 35, pp. 11831–11840, 2009.

[33] K. Zeng, Y. Fang, and S. Zheng, "Organic-inorganic hybrid hydrogels involving poly(N-isopropylacrylamide) and polyhedral oligomeric silsesquioxane: preparation and rapid thermoresponsive properties," *Journal of Polymer Science B*, vol. 47, no. 5, pp. 504–516, 2009.

[34] W. Zhang, L. Liu, X. Zhuang, X. Li, J. Bai, and Y. Chen, "Synthesis and self-assembly of tadpole-shaped organic/inorganic hybrid poly(N-isopropylacrylamide) containing polyhedral oligomeric silsesquioxane via RAFT polymerization," *Journal of Polymer Science A*, vol. 46, no. 21, pp. 7049–7061, 2008.

[35] Y. C. Wu and S. W. Kuo, "Synthesis and characterization of polyhedral oligomeric silsesquioxane (POSS) with multifunctional benzoxazine groups through click chemistry," *Polymer*, vol. 51, no. 17, pp. 3948–3955, 2010.

[36] S. W. Kuo and H. T. Tsai, "Control of peptide secondary structure on star shape polypeptides tethered to polyhedral oligomeric silsesquioxane nanoparticle through click chemistry," *Polymer*, vol. 51, no. 24, pp. 5695–5704, 2010.

[37] M. Ciampolini and N. Nardi, "Five-coordinated high-spin complexes of bivalent cobalt, nickel, and copper with tris(2-dimethylaminoethyl)amine," *Inorganic Chemistry*, vol. 5, no. 1, pp. 41–44, 1966.

[38] C.-T. Lai, R.-H. Chien, S.-W. Kuo, and J.-L. Hong, "Tetraphenylthiophene-functionalized poly(n-isopropylacrylamide): probing lcst with aggregation-induced emission," *Macromolecules*, vol. 44, no. 16, pp. 6546–6556, 2011.

[39] W. Zhang and A. H. E. Müller, "Synthesis of tadpole-shaped POSS-containing hybrid polymers via "click chemistry"," *Polymer*, vol. 51, no. 10, pp. 2133–2139, 2010.

[40] Y.-S. Ye, W.-C. Shen, C.-Y. Tseng et al., "Versatile grafting approaches to star-shaped POSS-containing hybrid polymers using RAFT polymerization and click chemistry," *Chemical Communications*, vol. 47, no. 38, pp. 10656–10658, 2011.

[41] J. Zhu, X. Zhu, E. T. Kang, and K. G. Neoh, "Design and synthesis of star polymers with hetero-arms by the combination of controlled radical polymerizations and click chemistry," *Polymer*, vol. 48, no. 24, pp. 6992–6999, 2007.

[42] W. I. Lee, Y. Bae, and A. J. Bard, "Strong blue photoluminescence and ECL from OH-terminated PAMAM dendrimers in the absence of gold nanoparticles," *Journal of the American Chemical Society*, vol. 126, no. 27, pp. 8358–8359, 2004.

[43] D. Wang and T. Imae, "Fluorescence emission from dendrimers and its pH dependence," *Journal of the American Chemical Society*, vol. 126, no. 41, pp. 13204–13205, 2004.

[44] D. Onoshima and T. Imae, "Dendritic nano- and microhydrogels fabricated by triethoxysilyl focal dendrons," *Soft Matter*, vol. 2, no. 2, pp. 141–148, 2006.

[45] D. Wang, T. Imae, and M. Miki, "Fluorescence emission from PAMAM and PPI dendrimers," *Journal of Colloid and Interface Science*, vol. 306, no. 2, pp. 222–227, 2007.

[46] O. Yemul and T. Imae, "Synthesis and characterization of poly(ethyleneimine) dendrimers," *Colloid and Polymer Science*, vol. 286, no. 6-7, pp. 747–752, 2008.

[47] K. Tamano and T. Imae, "Investigation of Luminescent poly(propylene imine) dendrimer," *Journal of Nanoscience and Nanotechnology*, vol. 8, no. 9, pp. 4329–4334, 2008.

[48] C. C. Chu and T. Imae, "Fluorescence investigations of oxygen-doped simple amine compared with fluorescent PAMAM dendrimer," *Macromolecular Rapid Communications*, vol. 30, no. 2, pp. 89–93, 2009.

[49] L. Pastor-Pérez, Y. Chen, Z. Shen, A. Lahoz, and S. E. Stiriba, "Unprecedented blue intrinsic photoluminescence from hyperbranched and linear polyethylenimines: polymer architectures and pH-effects," *Macromolecular Rapid Communications*, vol. 28, no. 13, pp. 1404–1409, 2007.

[50] M. J. Jasmine and E. Prasad, "Fractal growth of PAMAM dendrimer aggregates and its impact on the intrinsic emission properties," *Journal of Physical Chemistry B*, vol. 114, no. 23, pp. 7735–7742, 2010.

[51] D. Wu, Y. Liu, C. He, and S. H. Goh, "Blue photoluminescence from hyperbranched poly(amino ester)s," *Macromolecules*, vol. 38, no. 24, pp. 9906–9909, 2005.

[52] Y. Lin, J. W. Gao, H. W. Liu, and Y. S. Li, "Synthesis and characterization of hyperbranched poly(ether amide)s with thermoresponsive property and unexpected strong blue photoluminescence," *Macromolecules*, vol. 42, no. 9, pp. 3237–3246, 2009.

Hindawi Publishing Corporation
Journal of Nanomaterials
Volume 2012, Article ID 975106, 7 pages
doi:10.1155/2012/975106

Research Article

Preparation of Silver Nanostructures from Bicontinuous Microemulsions

M. A. Pedroza-Toscano,[1] M. Rabelero-Velasco,[1] R. Díaz de León,[2] H. Saade,[2] R. G. López,[2] E. Mendizábal,[1] and J. E. Puig[1]

[1] *Departamentos de Ingeniería Química y Química, CUCEI, Universidad de Guadalajara, Boul. M. García Barragán No. 1431, 44430 Guadalajara, SAL, Mexico*
[2] *Departamento de Procesos de Polimerización, Centro de Investigación en Química Aplicada, Boulevard Enrique Reyna No. 140, 252294 Saltillo, CAOH, Mexico*

Correspondence should be addressed to R. G. López, glopez@ciqa.mx

Received 9 February 2012; Revised 28 March 2012; Accepted 2 April 2012

Academic Editor: Alejandro Manzano Ramirez

Precipitation of silver nanoparticles at 70°C was carried out by dosing a 1.3 M sodium borohydride aqueous solution over bicontinuous microemulsions formed with a mixture of sodium bis(2-ethylhexyl) sulfosuccinate (AOT) and sodium dodecylsulfate (SDS) as surfactants, a 0.5 M silver nitrate aqueous solution, and toluene. Weight ratios of 2.5/1 and 3/1 AOT/SDS were used in the precipitation reactions. Silver nanoparticles were characterized by transmission electronic microscopy, X-ray diffraction, and atomic absorption spectroscopy. A mixture of isolated spheroidal nanoparticles (≈15 wt.%) with an average diameter around 10 nm and wormlike structures (≈85 wt.%) with an average length close to 480 nm and an average diameter ca. 40 nm was obtained, regardless of the AOT/SDS ratio. Higher yields were obtained compared with those reported when reverse microemulsions were employed. Formation of wormlike structures was ascribed to one-dimensional aggregation of crystal and particles within the channels of bicontinuous microemulsions, which performed as templates.

1. Introduction

Reverse microemulsions have been used for several years in precipitation reactions to obtain inorganic nanoparticles of the metals Cu, Pd, Rh, Ir, Au, and Pt and of metal compounds such as $Al(OH)_3$, Fe_3O_4, TiO_2, V_2O_5, ZnO, and ZrO_2 [1]. In these cases the particles precursors are situated in the aqueous phase of a reverse microemulsion, to which another reverse microemulsion containing the precipitating agent or an aqueous solution of the precipitating agent is added, to produce the inorganic nanoparticles [2–8].

Nowadays there is an increasing interest in the preparation and characterization of silver nanoparticles, because of their applications in catalysis [9, 10], in nonlinear optical technology, as bactericidal agent [11, 12] and in nanosphere lithography [13]. The synthesis of silver nanoparticles with average diameters smaller than 15 nm and narrow size distributions has been reported by precipitation in reverse microemulsions, but the productivity is usually low (≤0.4 g/100 g microemulsion) [3–5, 7, 8, 14, 15]. To increase the productivity of silver nanoparticles, Sosa et al. [16] used high water-content reverse microemulsions. Lim et al. [17] used bicontinuous microemulsions for obtaining zinc oxide nanoparticles; however, their productivity was not so high (0.7 g nanoparticles/100 g microemulsion) and the particles were relatively large (>150 nm in average diameter). Also, our group have employed bicontinuous microemulsions with larger water-to-oil ratios than those in reverse microemulsions, to obtain very small nanoparticles of magnetite-maghemite [18, 19], zinc oxide [20, 21], and silver [22] with diameters smaller than 10 nm and productivities higher than 1 g nanoparticles/100 g microemulsion, which is significantly larger than those obtained when reverse microemulsions were utilized. Recently, Kowlgi et al. [23] obtained platinum

nanoparticles with average diameters from 1.8 to 18 nm in bicontinuous microemulsions, depending on the concentration of the platinum precursor aqueous solution.

In the only report, as far as we know, on precipitation of silver nanoparticles in bicontinuous microemulsions, Reyes et al. [22] used microemulsions stabilized with a mixture of AOT/SDS (2/1, w/w) containing 0.5 M silver nitrate ($AgNO_3$) aqueous solution, and toluene to obtain a mixture of isolated spheroidal and wormlike nanoparticles. The proportion of the latter decreased as the concentration of the precipitating agent (sodium borohydride) in the aqueous solution added to the microemulsion diminished.

As a continuation of the work of Reyes et al. [22], we report here the preparation of silver nanoparticles in bicontinuous microemulsions stabilized with different AOT/SDS weight ratios and their effect on the morphology and size. Nanoparticles were characterized by transmission electron microscopy (TEM), X-ray diffraction, and atomic absorption spectroscopy.

2. Materials and Methods

2.1. Materials. SDS and AOT were 98% pure from Sigma-Aldrich. $AgNO_3$ (98.2% pure from Merck) and toluene (99% pure from Golden Bell) were used as received. De-ionized and triple-distilled water with conductivity smaller than 6 μS/cm was used.

2.2. Phase Diagram and Electrical Conductivity Determination. The one-phase microemulsion region at the reaction temperature (70°C) was determined by titrating solutions of AOT/SDS (2.5/1 and 3/1 by weight) in toluene at different surfactant/toluene ratios (in the range of 5 to 65 w/w) with a 0.5 M $AgNO_3$ aqueous solution under continuous agitation. The phase boundaries were detected as those compositions where samples became turbid. Samples were also examined with cross-polarizers to rule out liquid crystalline phases that might form. Phase boundaries were checked by preparing samples by weight with compositions above and below the titration-determined phase boundaries in sealed glass vials.

To determine the compositions where bicontinuous microemulsion formed, conductivities of samples along lines A, B, and C, which corresponds to 50/50, 55/45, and 60/40 surfactant mixture-to-toluene weight ratio (Figure 1), were analyzed with a 3173R JENCO conductivity meter at 70°C. To prepare silver nanoparticles two compositions in the bicontinuous microemulsion region were used. In both cases, the concentrations of 0.5 M $AgNO_3$ aqueous solution, surfactants mixture, and toluene (35, 39, and 25 wt.%, resp.) were the same and only the AOT/SDS weight ratio was modified (2.5/1 and 3/1).

2.3. Silver Particles Precipitation. The precipitation reaction was carried out in duplicate at 70°C in a 250 mL jacketed glass reactor equipped with a reflux condenser and an inlet for the sodium borohydride aqueous solution feeding. The procedure for the precipitation reaction started by loading the reactor with the microemulsion (100 g) and raising the temperature to 70°C. Then, a 1.3 M sodium borohydride aqueous solution was dosed at a rate of 0.1 g/min for 150 minutes. At these conditions, the molar ratio sodium borohydride/silver nitrate was 10% higher than the stoichiometric ratio. After completing the sodium borohydride addition, the reaction was allowed to proceed for 30 more minutes and then acetone was added to precipitate the solids, which were allowed to settle for 24 hours. The precipitate was washed at least ten times with a water-acetone solution (81/19, w/w) and then dried in an oven at 60°C for 24 hours.

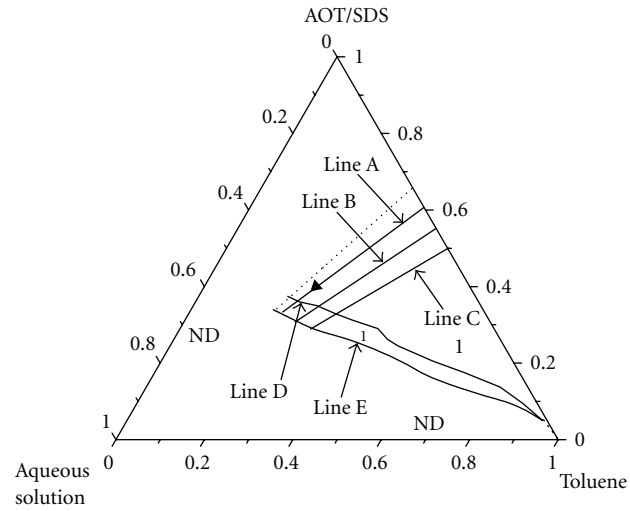

Figure 1: Partial phase diagrams at 70°C for mixtures of toluene, 0.5 M $AgNO_3$ aqueous solution, and AOT/SDS weight ratios of 2.5/1 (D) and 3/1 (E). The one-phase microemulsion region is denoted by 1ϕ. The nondetermined (ND) regions were not examined because they are not interesting for the present work. Lines A, B, and C, indicate the compositions along which electrical conductivity measurements were performed. Solid triangle shows the composition where the precipitation reactions were made.

2.4. Characterization. The resulting product, a fine powder, was characterized in a Siemens D-5000 X-ray diffractometer (XRD). Particle size was determined by TEM in a JEOL JEM-1010; for this, the resulting powder was dispersed in acetone with an ultrasonicator, and then a drop of the dispersion was deposited on a copper grid, where the solvent was allowed to evaporate. The purity of the final product was determined in a Varian Spectra250 AA atomic absorption spectrometer.

3. Results and Discussion

To delimit the region where one-phase microemulsions formed, pseudoternary phase diagrams were obtained. The systems were prepared with a mixture of AOT/SDS at two different weight ratios, toluene, and 0.5 M $AgNO_3$ aqueous solution. Figure 1 shows the pseudoternary phase diagrams for the systems containing mixtures of AOT/SDS with weight ratios of 2.5/1 and 3/1. A slightly larger microemulsion region was obtained when the AOT/SDS ratio of 3/1 was used in the formulation. The microemulsion

regions obtained with both AOT/SDS ratios extend to the central part of the diagram, which suggests the existence of bicontinuous microemulsions. However, the microemulsion regions do not extend to the water-rich zone of the diagram as it was detected when AOT/SDS (2/1 w/w) mixture was employed [22], which indicates the absence of normal (oil-in-water) microemulsions. This can be explained since AOT tends to form inverse micelles and (w/o) microemulsions whereas SDS tends to form normal micelles and (o/w) microemulsions [24].

Because it is desirable to obtain the largest possible amount of silver nanoparticles, three ratios of surfactants/toluene mixture (50/50, 55/45, and 60/40 w/w), which allows higher concentrations of aqueous solution inside the microemulsion region, were selected. To find the bicontinuous microemulsion region, the content of the 0.5 M aqueous $AgNO_3$ solution was increased while maintaining the ratio of surfactant/toluene constant (lines A, B, and C, in Figure 1) and their electrical conductivities were measured.

Figures 2 and 3 depict the electrical conductivity for the AOT/SDS weight ratios of 2.5/1 and 3/1, respectively, as a function of the amount of the $AgNO_3$ aqueous solution for the three selected surfactants/toluene weight ratios (50/50, 55/45, and 60/40). For the two chosen AOT/SDS weight ratios (2.5/1 and 3/1), the conductivities along the microemulsion region were very low in the cases of 50/50 and 55/45 surfactants/toluene ratios. When the 60/40 surfactants/toluene weight ratio was used and the AOT/SDS weight ratio was 3/1, the microemulsion conductivity started to rise when the $AgNO_3$ aqueous solution concentration was around 22.5 wt.%, reaching a maximum of 1900 μS/cm at around 40 wt.%, followed by a conductivity drop. For the microemulsions prepared with the 2.5/1 AOT/SDS weight ratio, the electrical conductivity started to increase at about 20 wt.% $AgNO_3$ aqueous solution; then the conductivity increased steeply and reached a maximum (4400 μS/cm) at a concentration of about 38 wt.%. In this case a drop in electrical conductivity could not be detected because the conductivity was not measured at aqueous $AgNO_3$ solution concentrations higher than 40 wt.%, because at this aqueous solution concentration, microemulsions do not form. According to the percolation theory, bicontinuous microemulsions show a high conductivity as a result of having continuous (or connected) aqueous phase domains [25–28]. In contrast, reverse microemulsions are very poor electrical conductors because of their discontinuous microstructure [25–28]. From the results obtained here, it follows that bicontinuous microemulsions form at a surfactants/toluene ratio of 60/40 (w/w) and AOT/SDS weight ratios of 2.5/1 and 3/1. When the former ratio is used, bicontinuous microemulsions develop in the range from 25–30 to 40 wt.% $AgNO_3$ aqueous solution; in the latter case, the span of the bicontinuous microemulsion region ranges from 27.5–30 to 45 wt.% $AgNO_3$ aqueous solution.

Precipitation reactions were carried out in bicontinuous microemulsions containing 35 wt.% 0.5 M $AgNO_3$ aqueous solution and AOT/SDS weight ratios of 2.5/1 and 3/1. The appearance of the precursor microemulsions was yellowish-translucent but then they turned black with the addition

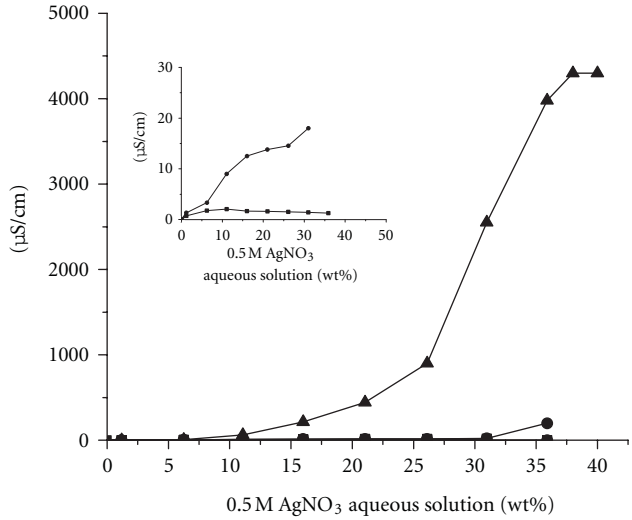

Figure 2: Electrical conductivity of the one-phase microemulsions versus concentration of 0.5 M $AgNO_3$ aqueous solutions for AOT/SDS weight ratios of 2.5/1 and ratios of surfactants/toluene of 50/50 (■), 55/45 (•), and 60/40 (▲) w/w.

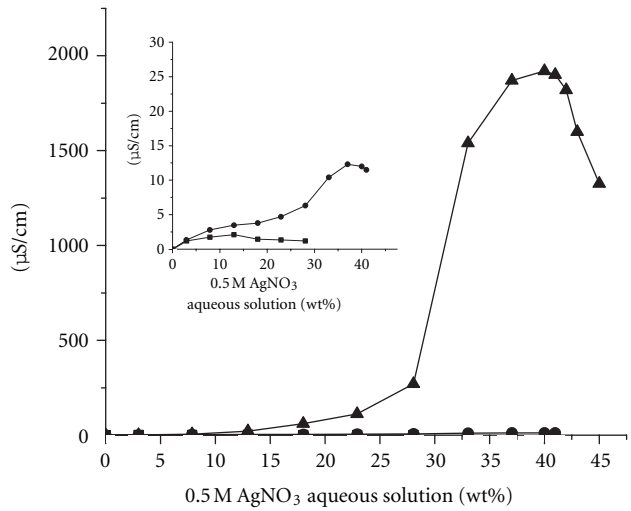

Figure 3: Electrical conductivity of the one-phase microemulsions versus concentration of 0.5 M $AgNO_3$ aqueous solutions for AOT/SDS weight ratios of 3/1 and ratios of surfactants/toluene of 50/50 (■), 55/45 (•) and, 60/40 (▲) w/w.

of the $NaBH_4$ aqueous solution. At the end of the reaction, the product (a grayish-black powder) was recovered, obtaining productivities of ca. 1.5 g Ag/100 g microemulsion-precipitating agent mixture and yields higher than 85% (Table 1) as determined by atomic absorption spectroscopy. When only the bicontinuous microemulsion is considered, the productivity is 1.7 g Ag/100 g microemulsion. This productivity is larger than the largest one calculated from the data in those reports that employed reverse microemulsions (0.4 g of Ag/100 g microemulsion) [4].

Figure 4 shows the X-ray diffraction pattern (XRDP) of the Ag nanoparticles obtained from microemulsions

Table 1: Ag nanoparticles purity, productivity and yield of the precipitation reactions.

AOT/SDS weight ratio	Ag purity (%)	Productivity (g Ag/100 g reaction mixture)	Yield (%)
2.5/1	93.76 ± 1.26	1.59 ± 0.06	91.34 ± 3.25
3/1	93.58 ± 1.54	1.48 ± 0.04	85.05 ± 2.44

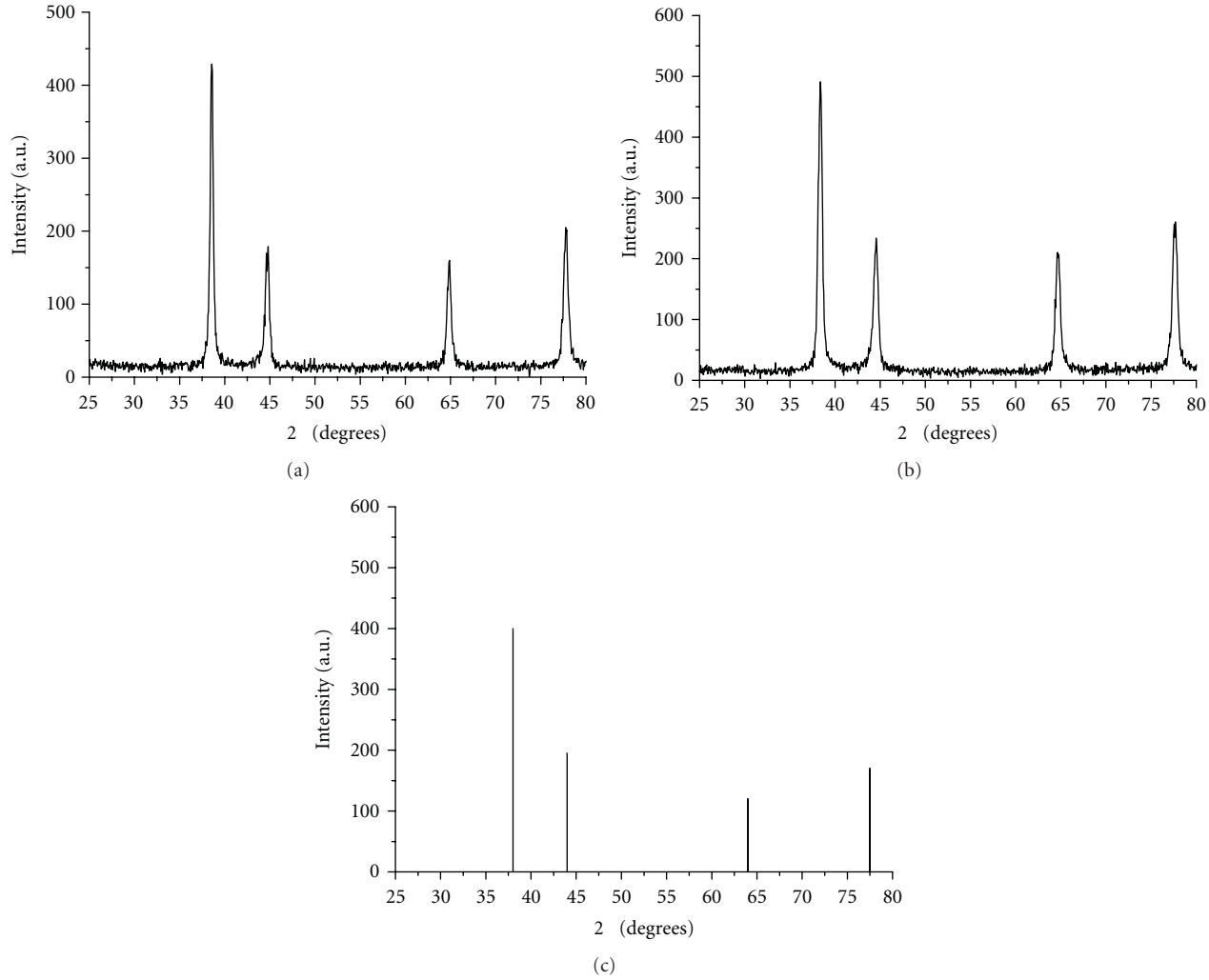

Figure 4: X-ray diffraction patterns for the precipitation reactions carried out at 2.5/1 (a) and 3/1 (b) AOT/SDS weight ratios. Standard pattern of silver is included (c).

made with the AOT/SDS weight ratios of 2.5 and 3/1 and the Ag-standard XRDP (JCPDS card file number 893722). The XRDPs of the Ag nanoparticles show the major four characteristic signals of silver crystal (at 38.14, 44.32, 64.60, and 77.44 $2\theta^{\circ}$), which corresponds to the face-centered cubic phase of pure silver nanoparticles.

An estimation of the average crystal size of the particles obtained in the precipitation reactions was made with the data from their XRDPs (Figure 4) and the well-known Scherrer equation:

$$d = \frac{K\lambda}{\beta \cos\theta}, \quad (1)$$

where d is the mean diameter of grain in nm, K is the dimensional factor (0.9), λ is the X-ray wavelength (0.154 nm), β is the line broadening at half the maximum intensity in radians, and θ is the Bragg's angle. Values of d of 17.85 ± 1.13 and 13.60 ± 1.90 nm for the precipitations carried out using the AOT/SDS ratios of 2.5/1 and 3/1, respectively, were obtained. According to this, the later AOT/SDS ratio limits to some extent crystal growth, probably because the higher content of AOT leads to a decrease in the diameter of the channels in the microemulsion, reducing the number of the Ag atoms in the vicinity of the nuclei.

Figure 5 depicts representative micrographs of the products prepared with AOT/SDS weight ratios of 2.5/1 and 3/1 along with their corresponding histograms of particle

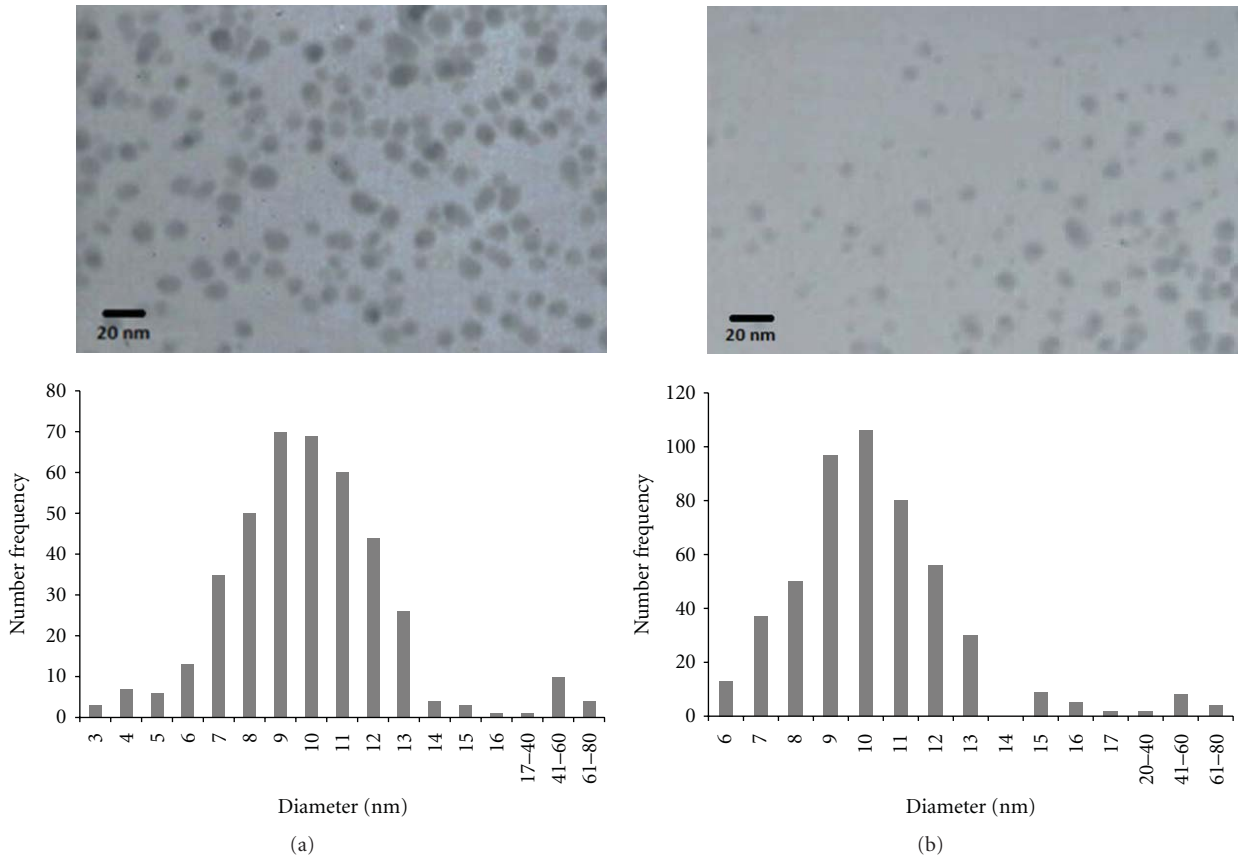

(a) (b)

Figure 5: TEM micrographs and their histograms for particles obtained from precipitation at 70°C in bicontinuous microemulsions containing 35 wt.% 0.5 M $AgNO_3$ aqueous solution and 39 wt.% AOT/SDS weight ratios of 2.5 (a) and 3/1 (b).

diameters obtained measuring over 500 particles. Most of the particles were isolated spheroids; however, a few wormlike particles were also observed (Figure 6). These histograms indicate that there are two particle populations: one including particles with diameters ≤ 16 nm, which was determined by measuring only the isolated spheroidal nanoparticles, and another one that includes larger particles (from 17 to 80 nm in diameter), which are forming the wormlike structures. Furthermore, the length of the worms was measured. Table 2 shows the average dimensions of the isolated spheroidal nanoparticles and of the wormlike nanoparticles as well as the number and weight fraction of the latter in the final product mixture. For the weight fraction calculation reported in Table 2, the isolated spheroidal nanoparticles were taken as perfect spheres, while wormlike nanoparticles were considered as cylinders. Then, the particles volume was calculated, and with the measured number proportion of spheroid and wormlike nanoparticles (Table 2) and the silver density, the weight fraction of each type of structure was estimated. Table 2 discloses that the isolated spheroidal nanoparticles have diameters of ca. 10 nm, whereas the wormlike structures show average lengths of around 480 nm and average diameters close to 40 nm. Although the number of larger particles is small (<3%), they represent 84 to 87 wt.%. Furthermore, data from Table 2 indicate that there is not statistical effect of the AOT/SDS ratio studied in this work on the morphology and size. However, there is a great difference between these results and those obtained in our previous work [22], where practically only isolated spheroidal nanoparticles with 3 nm in average diameter were obtained. In that work also a low concentration of $NaBH_4$ aqueous solution was used, but microemulsions were stabilized with a lower AOT/SDS weight ratio (2/1). An explanation of the differences between the results reported here and those of Reyes et al. [22] would arise from the increase in the proportion of AOT molecules in the surfactant layer, which diminished the protector effect of this layer during the inter-channel collisions, leading to a an increase in the fusion-fission rate during Ag particle formation and, consequently, on the nanoparticles coalescence, giving more wormlike nanostructures.

A comparison of the nanostructures dimensions determined by TEM with those calculated from X-ray data indicates that the average diameter of the isolated spheroidal nanoparticles (≈10 nm) is smaller than the average crystal diameters (17.9 and 13.6 nm for AOT/SDS weight ratio, 2.5/1 and 3/1, resp.). This suggests that each nanoparticle in the population of isolated spheroidal structures is formed of a single crystal. In contrast, the wormlike nanoparticles, the dimensions of which are much higher than the average crystal diameter, are formed by aggregation of crystals. This aggregation arises from the fact that crystals and particles

Table 2: Average sizes of silver nanoparticles and composition of the final mixture.

AOT/SDS weight ratio	Spheroidal nanoparticles	Wormlike nanoparticles			
	D_n (nm)	Average diameter (nm)	Average length (nm)	Average number percent	Average weight percent
2.5/1	10.18 ± 1.95	43 ± 17.55	490 ± 205	2.6 ± 1.2	86.7 ± 2.45
3/1	9.64 ± 2.05	38.00 ± 15.34	465 ± 181	2.7 ± 0.2	84.4 ± 2.87

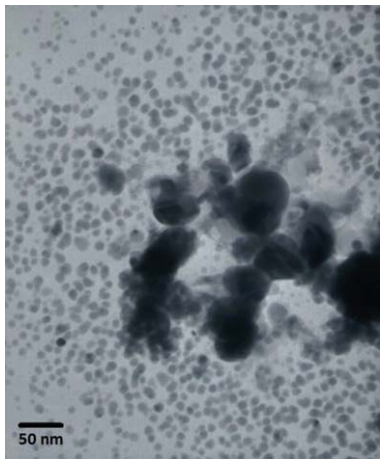

Figure 6: Representative micrograph of wormlike nanostructures obtained in precipitation reactions.

within the channels of bicontinuous microemulsions are not protected with a surfactant layer, as they are in the case of precipitation in reverse microemulsions. This condition favors the crystal and particle aggregation as a consequence of collisions between these structures. Moreover, because microemulsions channels act as templates, one-dimensional aggregation would be expected, forming the wormlike structures.

4. Conclusions

Silver nanoparticles with two particle size populations were obtained by precipitation in bicontinuous microemulsions. The productivity of silver nanoparticles obtained by this method was around 1.5 g silver nanoparticles/100 g microemulsion-precipitating agent mixture, which is higher than those reported with reverse microemulsions. The structures forming the smaller particles population were isolated spheroids with an average diameter of 10 nm, which represents around 15% of the total weight of the nanoparticles. The larger particles composing the other population were wormlike structures with an average length of 480 nm and average diameter of 40 nm and although they are only 3% of the total number of particles, they represent around 85% of the total weight of the obtained Ag nanostructures. No statistical effect of AOT/SDS ratio on morphology and particle size was identified. Formation of wormlike structures was ascribed to a one-dimensional aggregation of crystals and particles within the microemulsion channels, which would arise from these nanostructures acting as templates.

Acknowledgments

This work was supported by FOMIXJAL (Grant no. 2009-05-124211) and CONACYT (Grants no. CB-2007-82437 and CB-2007-84009). One of the authors (M. A. Pedroza-Toscano) acknowledges the scholarship from CONACYT. The authors are grateful to Alejandro Espinoza and Blanca Huerta for their technical assistance in characterization work.

References

[1] K. Osseo-Asare, *Handbook of Microemulsion Science and Technology*, Marcel Dekker, New York, NY, USA, 1999.

[2] P. Barnickel and A. Wokaun, "Synthesis of metal colloids in inverse microemulsions," *Molecular Physics*, vol. 69, no. 1, pp. 1–9, 1990.

[3] C. Petit, P. Lixon, and M. P. Pileni, "In situ synthesis of silver nanocluster in AOT reverse micelles," *Journal of Physical Chemistry*, vol. 97, no. 49, pp. 12974–12983, 1993.

[4] L. A. Pavlyukhina, T. O. Zaikova, G. V. Odegova, S. A. Savintseva, and V. V. Boldyrev, "Silver cluster and nanoparticles: preparation in water-in-oil microemulsions and some physical properties," *Inorganic Materials*, vol. 34, no. 2, pp. 109–113, 1998.

[5] Z. Zhang, R. C. Patel, R. Kothari, C. P. Johnson, S. E. Friberg, and P. A. Aikens, "Stable silver clusters and nanoparticles prepared in polyacrylate and inverse micellar solutions," *Journal of Physical Chemistry B*, vol. 104, no. 6, pp. 1176–1182, 2000.

[6] W. Zhang, X. Qiao, and J. Chen, "Synthesis and characterization of silver nanoparticles in AOT microemulsion system," *Chemical Physics*, vol. 330, no. 3, pp. 495–500, 2006.

[7] W. Zhang, X. Qiao, J. Chen, and H. Wang, "Preparation of silver nanoparticles in water-in-oil AOT reverse micelles," *Journal of Colloid and Interface Science*, vol. 302, no. 1, pp. 370–373, 2006.

[8] W. Zhang, X. Qiao, and J. Chen, "Synthesis of nanosilver colloidal particles in water/oil microemulsion," *Colloids and Surfaces A*, vol. 299, no. 1–3, pp. 22–28, 2007.

[9] N. Pradhan, A. Pal, and T. Pal, "Silver nanoparticle catalyzed reduction of aromatic nitro compounds," *Colloids and Surfaces A*, vol. 196, no. 2-3, pp. 247–257, 2002.

[10] H. Nakatsuji, H. Nakai, K. Ikeda, and Y. Yamamoto, "Mechanism of the partial oxidation of ethylene on an Ag surface: dipped adcluster model study," *Surface Science*, vol. 384, no. 1–3, pp. 315–333, 1997.

[11] Q. L. Feng, J. Wu, G. Q. Chen, F. Z. Cui, T. N. Kim, and J. O. Kim, "A mechanistic study of the antibacterial silver ions on Escherichia coli and Staphylococcus aureus," *Journal of Biomedical Materials Research*, vol. 52, no. 4, pp. 662–668, 2000.

[12] J. W. Kim, J. E. Lee, S. J. Kim et al., "Synthesis of silver/polymer colloidal composites from surface-functional porous polymer microspheres," *Polymer*, vol. 45, no. 14, pp. 4741–4747, 2004.

[13] J. C. Hulteen, D. A. Treichel, M. T. Smith, M. L. Duval, T. R. Jensen, and R. P. Van Duyne, "Nanosphere lithography: size-tunable silver nanoparticle and surface cluster arrays," *Journal of Physical Chemistry B*, vol. 103, no. 19, pp. 3854–3863, 1999.

[14] J. N. Solanki and Z. V. P. Murthy, "Highly monodisperse and sub-nano silver particles synthesis via microemulsion technique," *Colloids and Surfaces A*, vol. 359, no. 1–3, pp. 31–38, 2010.

[15] X. Wu, T. Wang, and H. Wu, "Facile preparation and formation mechanism of uniform silver nanoparticles using OP-10 as emulsifier in reverse microemulsion," *Journal Wuhan University of Technology, Materials Science Edition*, vol. 26, no. 1, pp. 38–42, 2011.

[16] Y. D. Sosa, M. Rabelero, M. E. Treviño, H. Saade, and R. G. López, "High-yield synthesis of silver nanoparticles by precipitation in a high-aqueous phase content reverse microemulsion," *Journal of Nanomaterials*, vol. 2010, Article ID 392572, 6 pages, 2010.

[17] B. P. Lim, J. Wang, S. C. Ng, C. H. Chew, and L. M. Gan, "A bicontinuous microemulsion route to zinc oxide powder," *Ceramics International*, vol. 24, no. 3, pp. 205–209, 1998.

[18] J. Esquivel, I. A. Facundo, M. E. Treviño, and R. G. López, "A novel method to prepare magnetic nanoparticles: precipitation in bicontinuous microemulsions," *Journal of Materials Science*, vol. 42, no. 21, pp. 9015–9020, 2007.

[19] A. L. Loo, M. G. Pineda, H. Saade, M. E. Treviño, and R. G. López, "Synthesis of magnetic nanoparticles in bicontinuous microemulsions. Effect of surfactant concentration," *Journal of Materials Science*, vol. 43, no. 10, pp. 3649–3654, 2008.

[20] S. López-Cuenca, L. A. Pérez Carrillo, M. Rabelero Velasco et al., "High-yield synthesis of zinc oxide nanoparticles from bicontinuous microemulsions," *Journal of Nanomaterials*, vol. 2011, Article ID 431382, 6 pages, 2011.

[21] L. E. Romo, H. Saade, B. Puente, M. L. López, R. Betancourt, and R. G. López, "Precipitation of zinc oxide nanoparticles in bicontinuous microemulsions," *Journal of Nanomaterials*, vol. 2011, Article ID 145963, 9 pages, 2011.

[22] P. Y. Reyes, J. A. Espinoza, M. E. Treviño, H. Saade, and R. G. López, "Synthesis of silver nanoparticles by precipitation in bicontinuous microemulsions," *Journal of Nanomaterials*, vol. 2010, Article ID 948941, 7 pages, 2010.

[23] K. Kowlgi, U. Lafont, M. Rappolt, and G. Koper, "Uniform metal nanoparticles produced at high yield in dense microemulsions," *Journal of Colloid and Interface Science*, vol. 372, no. 1, pp. 16–23, 2012.

[24] J. N. Israelachvili, *Intermolecular and Surface Forces*, Academic Press, San Diego, Calif, USA, 2nd edition, 1991.

[25] H. F. Eicke, M. Borkovec, and B. Das-Gupta, "Conductivity of water-in-oil microemulsions: a quantitative charge fluctuation model," *Journal of Physical Chemistry*, vol. 93, no. 1, pp. 314–317, 1989.

[26] M. Borkovec, H. F. Eicke, H. Hammerich, and B. Das Gupta, "Two percolation processes in microemulsions," *Journal of physical chemistry*, vol. 92, no. 1, pp. 206–211, 1988.

[27] J. F. Billman and E. W. Kaler, "Structure and phase behavior in five-component microemulsions," *Langmuir*, vol. 6, no. 3, pp. 611–620, 1990.

[28] A. Maitra, C. Mathew, and M. Varshney, "Closed and open structure aggregates in microemulsions and mechanism of percolative conduction," *Journal of Physical Chemistry*, vol. 94, no. 13, pp. 5290–5292, 1990.

Hindawi Publishing Corporation
Journal of Nanomaterials
Volume 2012, Article ID 283031, 8 pages
doi:10.1155/2012/283031

Research Article

Microstructure and Crystallization Kinetics of Polyurethane Thermoplastics Containing Trisilanol Isobutyl POSS

Vinicius Pistor,[1,2] Daniela de Conto,[1] Felipe Gustavo Ornaghi,[1,2] and Ademir José Zattera[1]

[1] *Laboratory of Polymers, Center of Exact Sciences and Technology (CCET), University of Caxias do Sul (UCS), 95070-560 Caxias do Sul, RS, Brazil*
[2] *Laboratory of Advanced Polymers, Federal University of Rio Grande do Sul (UFRGS), 91501-970 Porto Alegre, RS, Brazil*

Correspondence should be addressed to Ademir José Zattera, ajzattera@terra.com.br

Received 14 November 2011; Revised 24 January 2012; Accepted 28 February 2012

Academic Editor: Sérgio Henrique Pezzin

The synthesis of thermoplastic polyurethanes (TPU) from the reaction of a NCO group-containing prepolymer and 0, 1.14, 1.71, and 2.28 wt% of trisilanol isobutyl polyhedral oligomeric silsesquioxane (POSS) was carried out in an instrumented batch mixer. The samples were characterized by thermogravimetric analysis (TGA), differential scanning calorimetry (DSC), X-ray diffraction (XRD), and scanning electron microscopy (SEM). SEM analysis shows that the incorporation of POSS promoted strongly aggregation through physical interactions (formation of POSS-rich domains). Modifications in the TPU microstructure and the reduction in the crystal size were observed in the XRD diffractograms. The incorporation of POSS equally altered the TPU crystallization, and samples bearing higher concentrations of POSS formed two distinct types of crystalline structures. The kinetics of crystallization showed that nucleation strongly depends on the balance between TPU crystal formation and POSS-rich domains.

1. Introduction

Polyurethanes represent a class of polymers with wide applications, including the medical, automotive, and industrial sectors [1]. These materials are an important class of thermoplastic and thermosetting polymers because of their mechanical, thermal, and chemical properties, which can be defined through the proper selection of a huge variety of materials [2]. The characteristic structural element in the vast majority of polyurethanes is the urethane group, based on a polyaddition reaction. The urethane bonds result from the reaction of an isocyanate (–N=C=O) with an alcohol (−OH) group [1, 3]. The application of polyurethane elastomers with thermoplastic features was first described in the 1950s, and they were first marketed in the 1960s. Currently, thermoplastic polyurethane (TPU) is one of the most versatile products within the group of engineered thermoplastics with elastomeric properties [4].

According to Odian [5], thermoplastic elastomers are multifunctional polymeric materials that usually present the processability of thermoplastics and the elasticity of vulcanised elastomers. However, some aspects of these materials restrict some of their applications even today because of the peculiarities of their processing. For example, when processing TPU by mixing in the molten state, they become extremely susceptible to thermal degradation and thermooxidation in the range of temperatures required for processing [6].

Polyurethanes are generally characterised by their low-thermal stability due to the thermally unstable urethane group. The thermal decomposition of urethane starts at the range from 150 to 200°C [7]. Above the temperatures of thermal stability, the urethane bonds dissociate and reassociate simultaneously [8]. The degradation caused by the dissociation of urethane bonds is reversible; however, since reduction in temperature leads to a recovery of urethane (reaction between the hydroxyl and the terminal isocyanate) [9–11], Lu et al. [12] described that the thermal degradation of polyurethanes in the melt state is inevitable as a result of the fusion that usually occurs around or above the temperature for stability of the urethane bonds (temperatures lower than 250°C). As a result of the process

of dissociation and reassociation of urethane, the molecular weight can change. Therefore, heat treatment of thermoplastic polyurethane above a critical temperature, particularly under experimental conditions or during processing in the molten state, can significantly change the viscosity, the crystallization behaviour, and even the mechanical properties of the resulting liquid [8]. Fortunately, with the rise of nanotechnology as one of the most promising fields in the development and modification of polymeric materials, many materials previously found to be too difficult to process can be revisited.

Polyhedral oligomeric silsesquioxane (POSS) molecules are structurally well defined as a three-dimensional cage [13, 14]. These compounds bear a silicon-containing inorganic core surrounded by organic groups. The typical size of the POSS cages is approximately 1.5 nm. Because of its hybrid nature and nanometric size, POSS are promising materials for nanocomposites [13–16]. The incorporation of POSS cages into the main chain of polymers can result in drastic changes in their properties, including increased processing temperature, oxidation resistance, surface hardness, improved mechanical properties, and reduced flammability and heat release. These improvements have been observed for a large number of thermoplastic polymers and some thermosetting polymers [13]. Aiming to improve the thermal stability of TPU in the range from 150 to 200°C [7] associated with the crystallization process, *in situ* addition of the trisilanol isobutyl polyhedral oligomer silsesquioxane (POSS) into the synthesis of thermoplastic polyurethane was achieved through a torque rheometer. Measurements were then carried out to evaluate the changes in thermal and morphological properties generated in the crystal structure of these nanocomposites.

2. Materials

The materials used in this study were Urecon 185 prepolymer (18% free NCO Coim), 1,4-butanediol (BDO, MCassab), and polyhedral oligomer trisilanol isobutyl silsesquioxane (POSS) (POSS, Hybrid Plastics). These materials were used as received. The chemical structures of the materials are illustrated in Figure 1.

3. Methods

3.1. Synthesis in Torque Rheometer. The syntheses were performed in an instrumented torque rheometer using roller type rotors counter-rotating at 90 rpm and at a temperature of 70°C for 60 minutes. The total volume of the rheometer chamber is 75 cm^{-3}, the total mass of each mixture being 50 g. The stoichiometry was calculated on the basis of the equivalents of isocyanate (NCO) and hydroxyl (OH) groups for the prepolymer and BDO, respectively (molar ratio NCO/OH = 1/1). A rate of 98% reacted NCO was maintained throughout the syntheses. Amounts of 1.14, 1.71, and 2.28 wt% of POSS were added *in situ* to the TPU synthesis reaction. The polymers were removed from the rheometer as solids and postcured at 90°C for 24 hours.

3.2. Thermogravimetric Analysis (TGA). The TGA analysis (TGA50-Shimdzu) was performed under an N_2 atmosphere (50 mL·min^{-1}) using approximately 20 mg of each sample. The analysis was performed at a heating rate of 10°C·min^{-1} from 25 to 730°C.

3.3. Differential Scanning Calorimetry (DSC). The DSC analysis (DSC 50-Shimadzu) was performed under a N_2 atmosphere (50 mL·min^{-1}) using approximately 10 mg of each sample. Samples were initially heated from ambient temperature to 250°C at a heating rate of 10°C·min^{-1}, cooling until the temperature of −80°C and then heated again at a rate of 10°C·min^{-1} to 250°C.

3.4. X-Ray Diffraction (XRD). X-ray diffractograms were collected using a sample holder mounted on a Shimadzu diffractometer (XRD-6000) with monochromatic CuKα radiation (λ = 0.15418 nm) and the generator working at 40 kV and 30 mA. Intensities were measured in the range of $3 < 2\theta < 35°$, typically with scan steps of 0.05° and 2 s/step (1.5° min^{-1}). Peak separations were carried out using Gaussian deconvolution. The determination coefficients (r^2) were close to unity (0.9982 and 0.9991). The d spacings were calculated using the Bragg equation [17, 18], and the crystallite sizes (L) were calculated using the Scherrer equation [17, 18].

3.5. Scanning Electron Microscopy (SEM). Scanning electron microscopy (SEM) was carried out using a Superscan S-550 instrument with a secondary electron detector and an acceleration voltage of 15.0 kW. The scanning was carried out at a magnification of 200 × (50 μm) and 1200 × (10 μm). The samples were previously covered with gold.

3.6. The Avrami Method. Throughout the decades, several kinetic models were developed to quantify the kinetic parameters involved in solid state reactions. For example, the original derivation performed by Avrami [19–21] was simplified by Meares [22] and Hay [23]. Equation (1) represents the original derivation Avrami used for isothermal experiments. Equation (2) presents the double logarithm used to obtain the kinetic parameters proposed by Avrami:

$$\alpha(t) = 1 - e^{-kt^n}, \tag{1}$$

$$\ln[-\ln(1-\alpha(t))] = \ln k + n \ln t, \tag{2}$$

where k is the Avrami constant dependent on the rate of nucleation or crystal growth and n is the Avrami exponent dependent on the dimensional process.

Taking into account the influence of the rate of heating/cooling on nonisothermal crystallization on the parameter k, Jeziorny [24] proposed the following relation using the Avrami equation:

$$\ln k' = \left(\frac{\ln k}{\phi}\right), \tag{3}$$

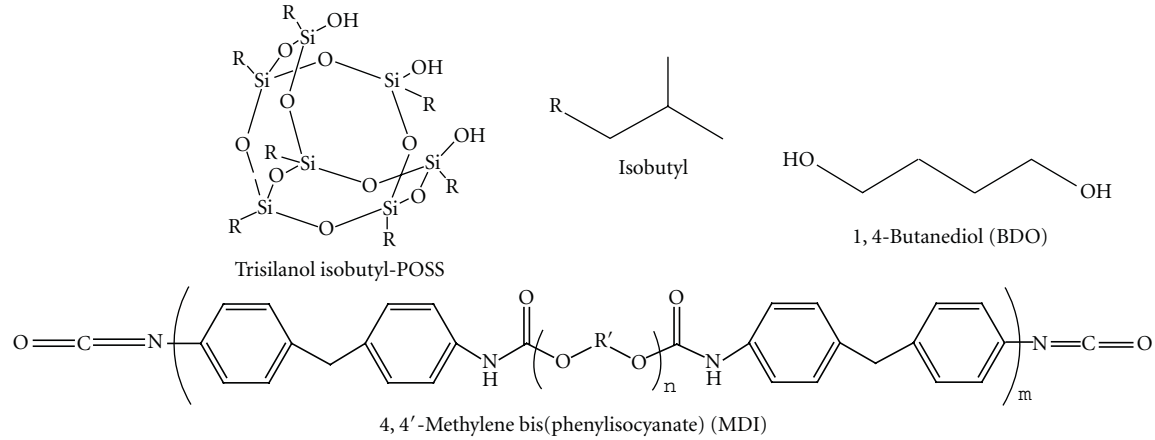

Figure 1: Chemical structures used for obtaining the nanocomposites studied.

where ϕ is the heating rate in $^{\circ}C \cdot min^{-1}$. Through the analysis of Jeziorny, in this case α is a function of temperature ($\alpha(T)$). Therefore, the constant k' was corrected as a function of ϕ.

4. Results and Discussion

4.1. Morphologic Characteristics. Figure 2 shows images obtained by cryogenic fracture in scanning electron microscopy (SEM) at ×200 and ×1200 related to images I and II, respectively. The images (a), (b), (c) and (d) correspond to 0, 1.14, 1.71 and 2.28 wt% of POSS, respectively. The morphology of the TPU presents detachment regions at interfacial fractures [25]. The incorporation of POSS nanocages (images Ib, Ic and Id) changed the morphology and showed more detachment regions than those observed for pure TPU. This modification in the microstructure was more evident by observing images IIa, IIb, IIc and IId. The POSS incorporated *in situ* in the TPU reaction was dispersed as clusters with diameters from 1 to 3 μm throughout the TPU microstructure.

This dispersion occurred because POSS has a strong aggregation effect through physical interactions [26]. This strong aggregation effect may be due to the silicon and oxygen cage being hydrophobic, as well as the isobutyl branches having poor chemical interactions with the TPU, which is hydrophilic in character. In this way, the only face of the nanocages interacting with the matrix would be the hydroxyls on the open face of the POSS cage (Figure 1).

4.2. X-Ray Diffraction (XRD). Three diffraction peaks in the range $2\theta = 18 - 23^{\circ}$ can be noted in Figure 3. These diffraction peaks with interplanar spacing (d-spacing) of 0.463, 0.413, and 0.379 nm were related to the lateral distances in the contours (interfaces) of the hard crystallised segments [27, 28]. These diffraction peaks were superimposed on the amorphous halo (Figure 3(b)) for the dispersion of TPU chains with regular interplanar spacing [29]. The hard segments of the crystal were related to various hydrogen bonds between urethane groups [30].

In the range of reflection of $2\theta \approx 11^{\circ}$, the diffraction peaks corresponding to a d-spacing of 0.851 nm were associated with the reflections reminiscent of the plan (001) and related to the perpendicular region of the lamellar surface [28]. The presence of POSS was confirmed in the scanning range of $2\theta = 7 - 8^{\circ}$ with d-spacing of 1.2 and 1.1 nm for peak V and VI, respectively [31]. Through the calculation of the crystallite size by the Scherrer equation [17, 18], it was possible to evaluate the influence of POSS domains in the crystalline structure of the TPU. The determination of the crystal size is detailed in Table 1.

The diffraction peaks of V and VI were associated with the microphase separation of the crystalline structure of POSS [31]. The incorporation of POSS reduced both the crystallite size (L_I) of the region perpendicular to the lamellar surface [28] and L_{II}. For the sizes L_{III} and L_{IV}, there was no clear tendency related to the incorporation of POSS, but all POSS-containing samples showed reduced L_{IV} compared with pure TPU. As the sizes of crystals in the region between $2\theta = 18 - 23^{\circ}$ were related to the formation of spherulites [32], the reduction in size of the crystals and the perpendicular region to the lamellar surface showed that the presence of POSS microdomains promoted modifications in crystal formation. Moreover, the larger the amount of POSS incorporated, the smaller the size of the POSS crystalline domains (L_V and L_{VI} in Table 1) and, consequently, the smaller the crystalline domains formed between the TPU hard segments (L_I and L_{II} in Table 1).

4.3. Crystallization Behavior by the Avrami Method. Considering the effects of the incorporation of POSS in the crystal structure of the TPU, it was possible to verify through the crystallization thermograms in Figure 4 that the addition of 1.14 wt% of POSS increased the TPU crystallization temperature.

This observation suggests that the crystallization was negatively impacted by nucleation through the POSS microdomains (Figure 2). The samples containing 1.71 and 2.28 wt% of POSS had even a higher range of crystallization temperature than the sample containing 1.14 wt% and

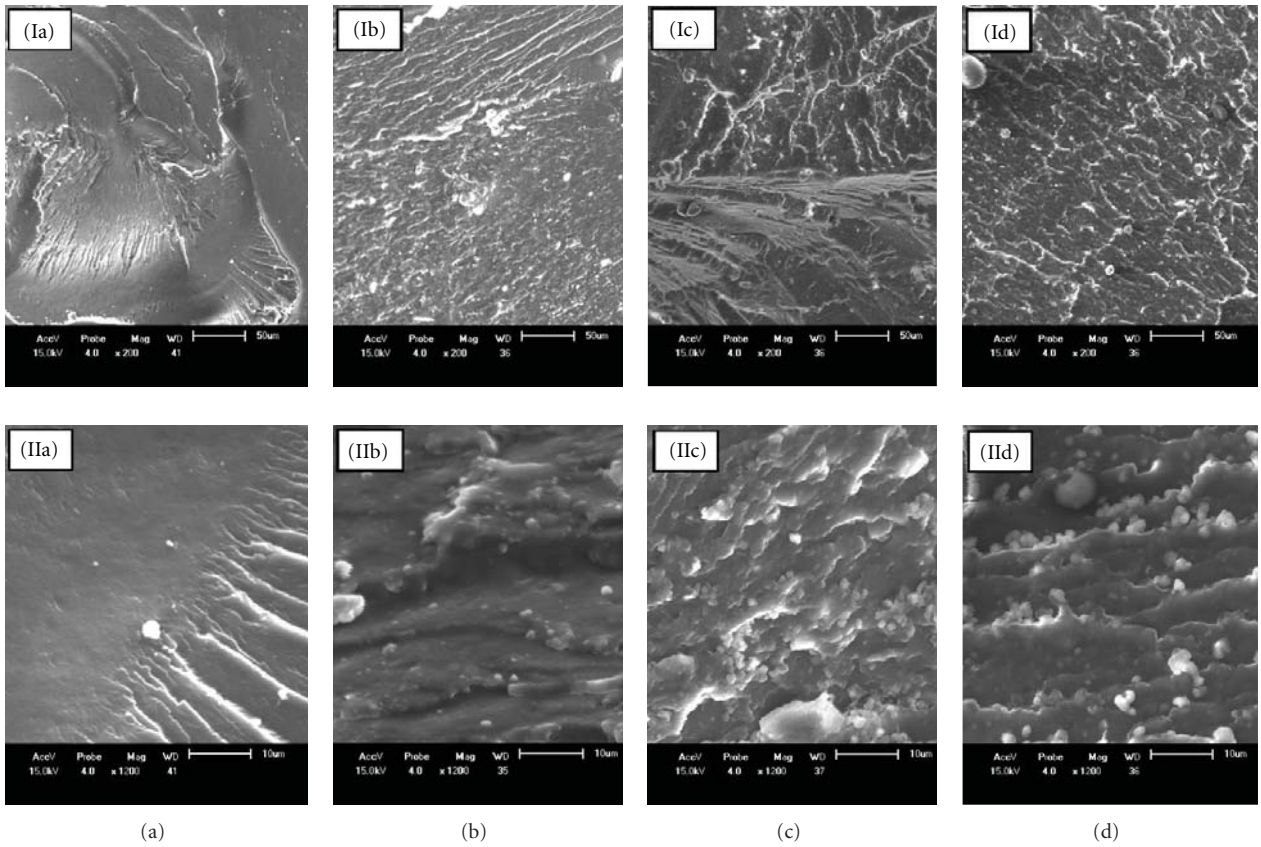

Figure 2: (a), (b), (c), and (d) morphological images obtained by scanning electron microscopy (SEM) for TPU and the TPU/POSS systems studied corresponding to 0, 1.14, 1.71, and 2.28 wt% of POSS at magnifications of ×200 and ×1200 for I and II, respectively.

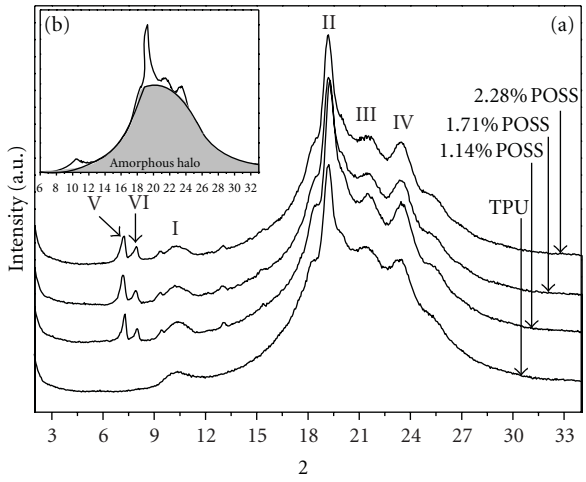

Figure 3: Analysis of X-ray diffraction data obtained with scan steps of 0.05° and 2 s/step (1.5° min^{-1}) for the samples studied where (a) Comparative curves obtained for the nanocomposites and (b) representation of an amorphous halo in the TPU sample.

showed a double crystallization peak that indicated the formation of two distinct types of crystalline structures.

The sample containing 1.14 wt% did not cause the same effect probably due to the fact that the amount of POSS seen in the SEM analysis (Figure 2) is not sufficient to modify the crystallization.

Table 1: Crystallite sizes obtained by the Sherrer equation for the diffraction peaks studied.

Sample	L_{I} (nm)	L_{II} (nm)	L_{III} (nm)	L_{IV}(nm)	L_{V} (nm)	L_{VI} (nm)
TPU	148.27	21.07	123.42	96.24	—	—
1.14%	30.37	20.49	127.79	60.78	54.49	162.35
1.71%	21.24	18.31	94.04	53.79	68.44	126.11
2.28%	16.73	17.27	135.38	58.57	22.99	107.85

The Avrami method was used to determine the kinetic parameters of crystallization at a heating rate of 10°C·min^{-1}. By integrating the exothermic crystallization peaks observed in Figure 4 it was possible to determine the conversion for the samples studied using the following relationship:

$$\alpha = \frac{1}{\Delta H_c} \int_0^t \frac{d(\Delta H_t)}{dt} dt, \tag{4}$$

where α is the fraction converted at time t, ΔH_c is the total heat involved in the process of crystallization, and ΔH_t is the heat generated at each time instant (t) [33, 34].

The conversion (α) curves in Figure 5 represent the evolution of the crystallization process, and as observed in the DSC thermograms, it was noted that the samples containing

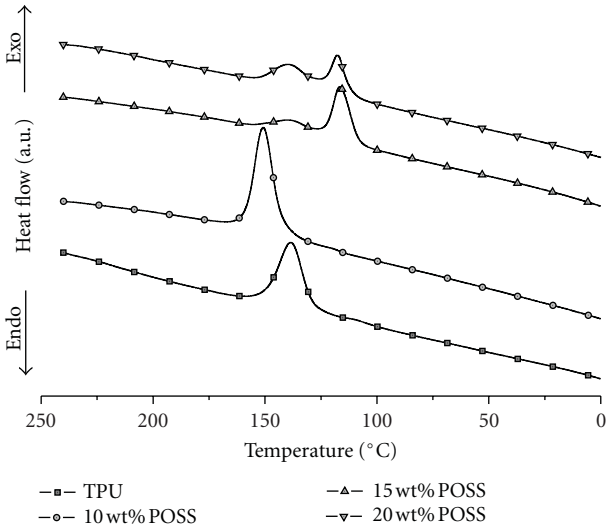

Figure 4: Crystallization thermograms obtained at a cooling rate of $10^{\circ}C \cdot min^{-1}$ after removal of the thermal history carried out at a heating rate of $10^{\circ}C \cdot min^{-1}$ from -50 to $240^{\circ}C$.

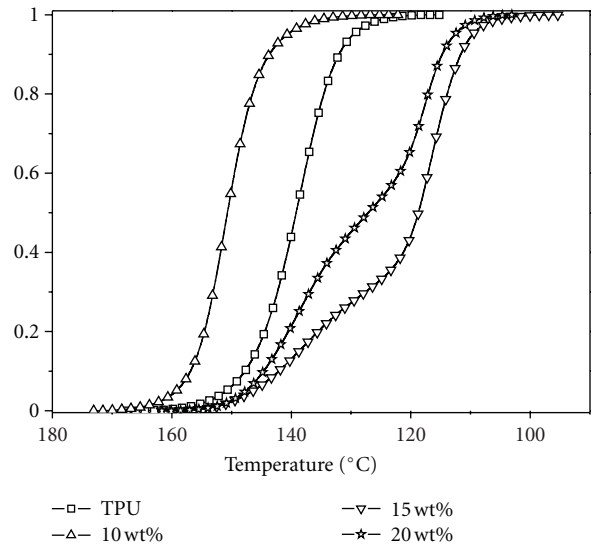

Figure 5: Conversion (α) curves obtained by integrating the exothermic peak crystallization.

1.71 and 2.28 wt% of POSS presented two velocity crystallization gradients. These two ranges of crystallization will be discussed as the first and second stages of crystallization in these samples. With the determination of α and making use of (2), Figure 6 representing the adjustment made to the Avrami equation was obtained [19–21].

According to Liu et al. [35], the Avrami equation represents only the initial polymer crystallization growth steps. The spherulites grew outward with a constant radial growth rate until a shock occurred as a result of the end of growth at the intersection of the crystals. Thus, the region for obtaining kinetic parameters related to the linear fit was determined at the more linear region in Figure 6. Table 2 presents the results obtained from DSC thermograms and the Avrami model. The degree of crystallinity calculated from the DSC analysis was determined by considering the enthalpy of crystallization of a 100% crystalline material ($H_{100\%}$ = 196.8 $J \cdot g^{-1}$) [34].

From the results depicted in Table 2 it was possible to observe a crystallization shift to higher temperatures for the sample containing 1.14 wt% of POSS. Moreover, the samples containing 1.71 and 2.28 wt% presented decreased enthalpy and degree of crystallinity, respectively. The reduction in ΔH_c and degree of crystallinity (% Cryst.) in the samples containing 1.71 and 2.28 wt% were associated with higher dispersion of the POSS compared with the sample containing 1.14 wt%. The 1.14 wt% sample had higher ΔH_c. This probably occurs because at this POSS content, the effect of spatial restriction at crystal interfaces is reduced. This would explain the increase in the crystallization temperature and crystallinity degree. It was also observed (L_{VI} in Table 1) that the incorporation of a higher nanocage content promotes a reduction in the POSS microphase sizes. The presence of POSS microdomains favoured the interaction of rigid segments with the POSS nanocages through the effect of

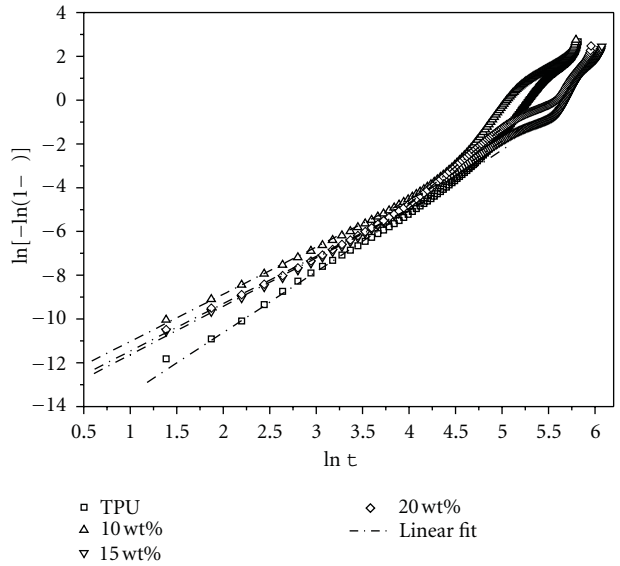

Figure 6: Linear fit used to obtain the Avrami kinetic parameters.

space hindrance at the interface of crystal growth as compared with pure TPU. This observation was supported by a double crystallization peak, which suggests that these samples were undergoing distinct nucleation and crystal growth phenomena.

The value of the rate constant (k'), corroborated with the results observed in the crystallization thermograms. With the increase in POSS content, the constant velocity of crystal growth and the half-life ($t_{1/2}$; i.e., the time required for 50% of the crystallization to occur) for the first crystallization stage decreased. The half-life reduction could be associated with the fact that smaller crystals were forming in the presence of POSS; thus, even with reduced k' the lowest

Table 2: DSC and kinetic crystallisation parameters for the Avrami method obtained at a heating rate of $10^{\circ}C \cdot min^{-1}$.

Sample	T_c (°C)	ΔH_c ($J \cdot g^{-1}$)	% Cryst.	k' (min^{-1})	$t_{1/2}$ (min)	n	r
TPU	138.54	24.02	12.21	16.18	0.32	2.77895	0.9986
1.14 wt.%	150.84	28.36	14.41	13.18	0.26	2.15848	0.9988
1.71 wt.%	140.2 and 115.9	19.68	10.00	13.88 and 16.00	0.26 and 0.33	2.21 and 2.83	0.9975
2.28 wt.%	140.8 and 117.9	18.82	9.56	13.62 and 18.77	0.25 and 0.39	2.16 and 3.50	0.9992

values of $t_{1/2}$ were principally dependent on the size of the crystalline domains and the type of crystal formed. The Avrami exponent (n) values were found to be $n \approx 3$ for pure TPU. The effect on the crystallization here described by the Avrami method would be that crystallization is controlled by three-dimensional diffusion in the form of spheres (spherulites) [22], characteristic of the type of crystals formed in the TPU crystallization [24, 32].

Begenir et al. [36], studying the crystallization behaviour of polyurethane elastomeric copolymers and polyether-b-amide, observed that the crystallization occurred in three dimensions from precores of hard segments due to regions of microphase separation (crystalline and amorphous). The authors also described that crystallization occurred through the association of hard segments by hydrogen bonding between urethane groups. Table 2 shows that by adding POSS (considering only the first stage of crystallization of the samples containing 1.71 and 2.28 wt%), the Avrami exponent values found were $n \approx 2$. The exponent n tending to 2 indicates that the crystallization could occur sporadically as two-dimensional discs [22]. This change in the values of n is in agreement with the reduction in crystal sizes L_{I} and L_{II} in Table 1. Then, for the second crystallization stage observed for samples containing 1.71 and 2.28 wt% of POSS, the values of k', $t_{1/2}$, and n were similar to those of pure TPU. The values of k', $t_{1/2}$ in the second crystallization stage (for 1.71 and 2.28 wt% of POSS) demonstrate as seen earlier the formation of radial spherulites. The sample containing 1.14 wt% of POSS showed only one value of $n \approx 2$, and the formation of disks could increase crystal packing. This assumption would explain why higher values were observed for %Cryst. and ΔH_c for the sample containing 1.14 wt% of POSS.

Figure 7 illustrates the crystallization behaviour related to the results shown in Table 2. For the exponent $n \approx 3$ (pure TPU), the dimensional processes demonstrated that crystal growth occurred radially along with the formation of small cores until the formation of well-defined crystals. The spherulites were composed of lamellar structures, which grow out radially. The individual chains were folded back and tangentially to the spherical surface of the growing spherulites [37]. However, at 1.14 wt% of POSS, the Avrami exponent tended to $n \approx 2$. This result shows that POSS impeded the radial crystal growth, thus making crystals oriented in at least one dimension of the plane. This behaviour corroborated the reduction in L_{I} displayed in Table 1.

According to Sperling [38], the crystal growth rate in the radial direction is constant until spherulites are formed. However, impurities, such as atactic components, can become a hindrance at the interlayer region. According to Zheng et al. [39], POSS tends to crystallise in two-dimensional lamellar structures. Although lamellar structures are found in low amounts of POSS, the plates became more organised for increased amounts of POSS. Strachota et al. [26] described the POSS undergoing strong aggregation due to physical interactions. As the nanocages interact strongly with each other [26] and tend to crystallise in two dimensions to form lamellar structures [39], it was possible to rationalize why the Avrami exponent tended to $n \approx 2$ for the TPU crystallization in the presence of POSS.

For the samples containing 1.71 and 2.28 wt% of POSS, two stages of crystallization were observed (Figure 7). The first crystallization stage was typical of disk formation with $n \approx 2$ due to the effect of nucleation on POSS, which acted as a system impurity. In the second crystallization stage, the change in the Avrami exponent (n) from 2 to 3 suggests that after the formation of crystals in the form of discs, spherulites formed.

This second stage was possibly related to the dispersion of the nanocages and the POSS crystalline domains reduction in size as determined by XRD. Moreover, since both the ΔH_c and the percentage of crystallinity (%Cryst.) suggested the formation of smaller crystals, the higher heterogeneity in the formation of the two crystalline phases was ascertained.

5. Conclusions

The influence of isobutyl trisilanol POSS on the crystalline structure of thermoplastic polyurethane was studied. POSS was added to replace the percentage mass of 1.4 butanediol in the *in situ* synthesis reaction by a torque rheometer.

The incorporation of POSS showed that clusters along the TPU microstructure occurred as a result of a strong aggregation effect through physical interactions between the nanocages.

The POSS reduced crystallite sizes were associated with spherulites formation at the crystallographic plane L_I and at the interlayer region of the crystals L_{II}. Increased POSS percentages also entrained diminished microdomains (L_{VI}) size.

The crystallization temperature was increased for the 1.14 wt% of POSS sample. However, for 1.71 and 2.28 wt% of POSS in the system, a double crystallization peak was noted, indicating the formation of two distinct types of crystalline structures. The adverse behaviour observed for the sample containing 1.14 wt% of POSS was associated to the low level of the nanocages incorporation. The double crystallization peak for the 1.71 and 2.28 wt% of POSS samples occurs probably because of the reduction in crystal size at the L_{I} and L_{II} planes in XRD analysis and by the spatial hindrance caused at the crystal interface.

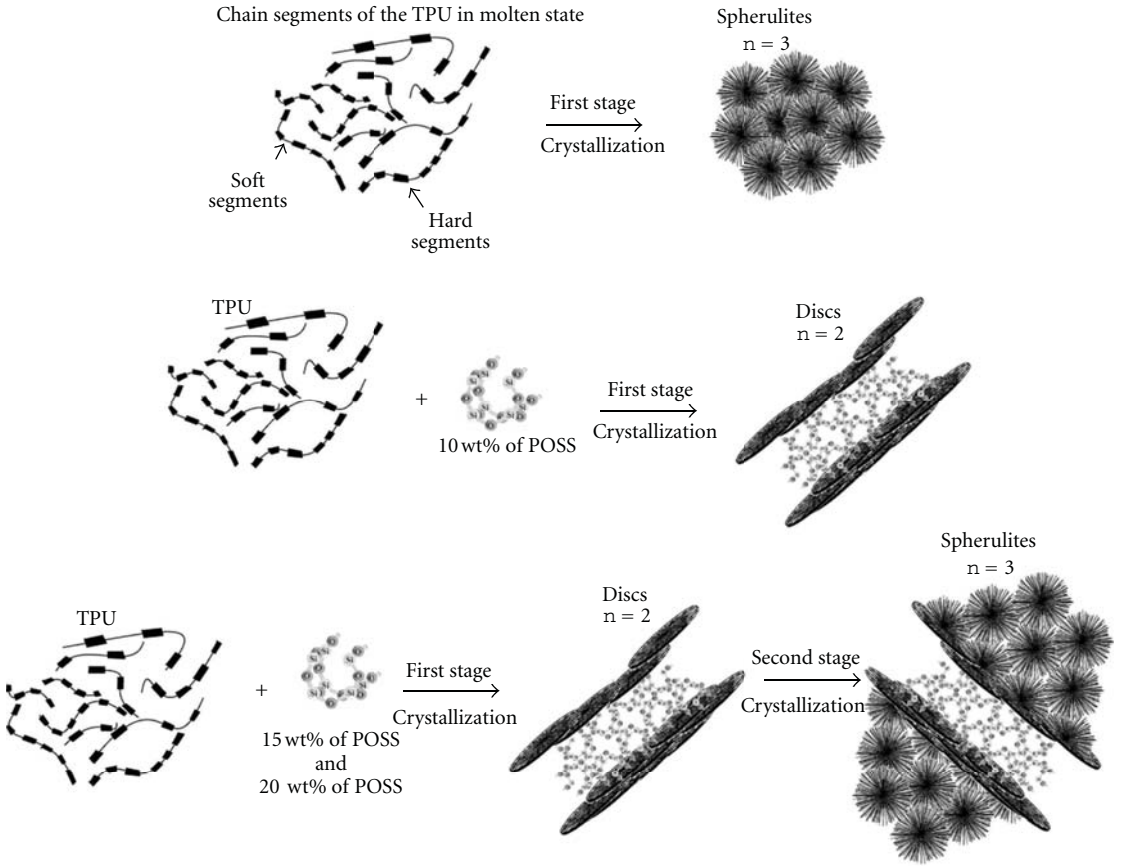

Figure 7: Schematics for the TPU and the nanocomposites nucleation and crystal growth phenomena.

The rate of crystal growth and the reduction in half-lives with increasing POSS content in the first crystallization stage was likely associated with the formation of smaller crystals in the presence of POSS. In the presence of POSS, crystallization occurs as two-dimensional discs, forming lamellar structures. The samples containing 1.71 and 2.28 wt% of POSS showed two crystallization stages, forming disks at first and then moving to spherulites. These results suggest that even the formation of clusters upon POSS incorporation showed a strong influence on the crystal nucleation and growth mechanism and these modifications should be considered for future applications of this type of nanoparticles.

Acknowledgment

The authors gratefully acknowledge the Brazilian National Council for Scientific and Technological Development (CNPq) for financial support.

References

[1] G. T. Howard, "Biodegradation of polyurethane: a review," *International Biodeterioration & Biodegradation*, vol. 49, no. 4, pp. 245–252, 2002.

[2] C. R. Kumar and J. Karger-Kocsis, "Curing and mechanical behavior of carboxylated NBR containing hygrothermally decomposed polyurethane," *European Polymer Journal*, vol. 38, no. 11, pp. 2231–2237, 2002.

[3] C. A. Harper and E. M. Petrie, *Plastics Materials and Processes: A Concise Encyclopedia*, John Wiley & Sons, Hoboken, NJ, USA, 2003.

[4] J. Scheirs, "Historical overview of styrenic polymers," in *Modern Styrenic Polymers*, J. Scheirs and D. Priddy, Eds., John Wiley & Sons, West Sussex, UK, 2003.

[5] G. Odian, *Principle of Polymerization*, John Wiley & Sons, Hoboken, NJ, USA, 4th edition, 2004.

[6] B. Finnigan, D. Martin, P. Halley, R. Truss, and K. Campbell, "Morphology and properties of thermoplastic polyurethane nanocomposites incorporating hydrophilic layered silicates," *Polymer*, vol. 45, no. 7, pp. 2249–2260, 2004.

[7] P. R. Nair, C. P. R. Nair, and D. J. Francis, "Phosphazene-modified polyurethanes: synthesis, mechanical and thermal characteristics," *European Polymer Journal*, vol. 32, no. 12, pp. 1415–1420, 1996.

[8] T. Hentschel and H. Münstedt, "Kinetics of the molar mass decrease in a polyurethane melt: a rheological study," *Polymer*, vol. 42, no. 7, pp. 3195–3203, 2001.

[9] M. S. Sánchez-Adsuar, "Influence of the composition on the crystallinity and adhesion properties of thermoplastic polyurethane elastomers," *International Journal of Adhesion and Adhesives*, vol. 20, no. 4, pp. 291–298, 2000.

[10] A. Frick and A. Rochman, "Characterization of TPU-elastomers by thermal analysis (DSC)," *Polymer Testing*, vol. 23, no. 4, pp. 413–417, 2004.

[11] M. Van der Schuur, B. Noordover, and R. J. Gaymans, "Polyurethane elastomers with amide chain extenders of uniform length," *Polymer*, vol. 47, no. 4, pp. 1091–1100, 2006.

[12] Q. W. Lu, M. E. Hernandez-Hernandez, and C. W. Macosko, "Explaining the abnormally high flow activation energy of thermoplastic polyurethanes," *Polymer*, vol. 44, no. 11, pp. 3309–3318, 2003.

[13] L. Liu, M. Tian, W. Zhang, L. Zhang, and J. E. Mark, "Crystallization and morphology study of polyhedral oligomeric silsesquioxane (POSS)/polysiloxane elastomer composites prepared by melt blending," *Polymer*, vol. 48, no. 11, pp. 3201–3212, 2007.

[14] S. Bizet, J. Galy, and J. F. Gérard, "Molecular dynamics simulation of organic-inorganic copolymers based on methacryl-POSS and methyl methacrylate," *Polymer*, vol. 47, no. 24, pp. 8219–8227, 2006.

[15] Y. Liu, S. Zheng, and K. Nie, "Epoxy nanocomposites with octa(propylglycidyl ether) polyhedral oligomeric silsesquioxane," *Polymer*, vol. 46, no. 25, pp. 12016–12025, 2005.

[16] A. Strachota, P. Whelan, J. Kriz et al., "Formation of nanostructured epoxy networks containing polyhedral oligomeric silsesquioxane (POSS) blocks," *Polymer*, vol. 48, no. 11, pp. 3041–3058, 2007.

[17] M. Wada and T. Okano, "Localization of Iα and Iβ phases in algal cellulose revealed by acid treatments," *Cellulose*, vol. 8, no. 3, pp. 183–188, 2001.

[18] U. J. Kim, S. H. Eom, and M. Wada, "Thermal decomposition of native cellulose: influence on crystallite size," *Polymer Degradation and Stability*, vol. 95, no. 5, pp. 778–781, 2010.

[19] M. Avrami, "Kinetics of change. I," *Journal of Chemical Physics*, vol. 7, no. 12, pp. 1103–1113, 1939.

[20] M. Avrami, "Kinetics of phase change. II Transformation-time relations for random distribution of nuclei," *Journal of Chemical Physics*, vol. 8, no. 2, pp. 212–224, 1940.

[21] M. Avrami, "Kinetics of phase change. III granulation, phase change, and microstructure," *Journal of Chemical Physics*, vol. 9, no. 2, pp. 177–184, 1941.

[22] P. Meares, *Polymers: Structure and Bulk Properties*, Van Nostrand, New York, NY, USA, 1965.

[23] J. N. Hay, "Application of the modified avrami equations to polymer crystallisation kinetics," *British Polymer Journal*, vol. 3, no. 2, pp. 74–82, 1971.

[24] A. Jeziorny, "Parameters characterizing the kinetics of the non-isothermal crystallization of poly(ethylene terephthalate) determined by d.s.c.," *Polymer*, vol. 19, no. 10, pp. 1142–1144, 1978.

[25] L. Pizzatto, A. Lizot, R. Fiorio et al., "Synthesis and characterization of thermoplastic polyurethane/nanoclay composites," *Materials Science and Engineering C*, vol. 29, no. 2, pp. 474–478, 2009.

[26] A. Strachota, I. Kroutilová, J. Kovárová, and L. Matejka, "Epoxy networks reinforced with polyhedral oligomeric silsesquioxanes (POSS). Thermomechanical properties," *Macromolecules*, vol. 37, no. 25, pp. 9457–9464, 2004.

[27] A. K. Nanda, D. A. Wicks, S. A. Madbouly, and J. U. Otaigbe, "Nanostructured polyurethane/POSS hybrid aqueous dispersions prepared by homogeneous solution polymerization," *Macromolecules*, vol. 39, no. 20, pp. 7037–7043, 2006.

[28] R. Androsh, J. Blackwell, S. N. Chvalun, G. Festel, and C. D. Eisenbach, "X-ray investigation of the structure of polyurethane elastomers based on 1,5-naphthalene diisocyanate," *Acta Polymerica*, vol. 48, pp. 363–368, 1997.

[29] G. Trovati, E. A. Sanches, S. C. Neto, Y. P. Mascarenhas, and G. O. Chierice, "Characterization of polyurethane resins by FTIR, TGA, and XRD," *Journal of Applied Polymer Science*, vol. 115, no. 1, pp. 263–268, 2010.

[30] L. Wang and Y. Wei, "Effect of soft segment length on properties of fluorinated polyurethanes," *Colloids and Surfaces B*, vol. 41, no. 4, pp. 249–255, 2005.

[31] J. Wu, Q. Ge, K. A. Burke, and P. T. Mather, "Crystallization of POSS in a PEG-based multiblock polyurethane: toward a hybrid hydrogel," *Materials Research Society*, vol. 847, pp. EE10.2.1–EE10.2.6, 2005.

[32] J. T. Koberstein and T. P. Russell, "Simultaneous SAXS-DSC study of multiple endothermic behavior in polyether-based polyurethane block copolymers," *Macromolecules*, vol. 19, no. 3, pp. 714–720, 1986.

[33] T. A. Ozawa, "A new method of quantitative differential thermal analysis," *Bulletin of the Chemical Society of Japan*, vol. 39, pp. 2071–2085, 1966.

[34] Y. Zhu, J. Hu, K. Choi, K. Yeung, Q. Meng, and S. Chen, "Crystallization and melting behavior of the crystalline soft segment in a shape-memory polyurethane ionomer," *Journal of Applied Polymer Science*, vol. 107, no. 1, pp. 599–609, 2008.

[35] W. Liu, H. Yang, B. S. Hsiao, R. S. Stein, S. Liu, and B. Huang, "Real-time crystallization and melting study of ethylene-based copolymers by SAXS, WAXD, and DSC techniques," *ACS Symposium Series*, vol. 739, chapter 12, pp. 187–200, 1999.

[36] A. Begenir, S. Michielsen, and B. Pourdeyhimi, "Crystallization behavior of elastomeric block copolymers: thermoplastic polyurethane and polyether-block-amide," *Journal of Applied Polymer Science*, vol. 111, no. 3, pp. 1246–1256, 2009.

[37] H. D. Keith and F. J. Padden, "Spherulitic crystallization from the melt. I. Fractionation and impurity segregation and their influence on crystalline morphology," *Journal of Applied Physics*, vol. 35, no. 4, pp. 1270–1285, 1964.

[38] L. H. Sperling, *Introduction to Physical Polymer Science*, John Wiley & Sons, New York, NY, USA, 2006.

[39] L. Zheng, S. Hong, G. Cardoen, E. Burgaz, S. P. Gido, and E. B. Coughlin, "Polymer nanocomposites through controlled self-assembly of cubic silsesquioxane scaffolds," *Macromolecules*, vol. 37, no. 23, pp. 8606–8611, 2004.

Hindawi Publishing Corporation
Journal of Nanomaterials
Volume 2012, Article ID 810623, 8 pages
doi:10.1155/2012/810623

Research Article

Influence of Compatibilizer and Processing Conditions on Morphology, Mechanical Properties, and Deformation Mechanism of PP/Clay Nanocomposite

B. Akbari[1,2] and R. Bagheri[1]

[1] *Polymeric Materials Research Group, Department of Materials Science and Engineering, Sharif University of Technology, P.O. Box 11155-9466, Tehran 11365, Iran*
[2] *Materials Engineering and Research, SAPCO, P.O. Box 13885-315, Tehran, Iran*

Correspondence should be addressed to R. Bagheri, rezabagh@sharif.edu

Received 15 December 2011; Revised 31 January 2012; Accepted 14 February 2012

Academic Editor: Luiz Antonio Ferreira Coelho

Polypropylene/montmorillonite nanocomposite was prepared by melt intercalation method using a twin-screw extruder with starve feeding system in this paper. The effects of compatibilizer, extruder rotor speed and feeding rate on properties of nanocomposite were investigated. Structure, tensile, and impact properties and deformation mechanism of the compounds were studied. For investigation of structure and deformation mechanisms, X-ray diffraction (XRD) and transmission optical microscopy (TOM) techniques were utilized, respectively. The results illustrate that introduction of the compatibilizer and also variation of the processing conditions affect structure and mechanical properties of nanocomposite.

1. Introduction

Inorganic fillers are extensively used in plastics industry in order to develop some properties such as stiffness, hardness, heat deflection temperature, and shrinkage along with cost decrease. The effects of filler particles on composite properties mainly depend on their shape, size, surface characterization, and extent of dispersion. In general, mechanical properties of polymers which are reinforced with microparticles are lower than those of nanocomposites [1]. In addition, obtaining desired physical properties such as surface roughness and permeability is difficult when microparticles are incorporated [1]. This is why many researches have focused on developing nanocomposites in recent years [2–4]. Among different nanofillers used, layered silicates such as montmorillonite have been considered significantly in recent years [5–12]. Polymers reinforced with montmorillonite reveal improvement of both mechanical and physical properties including elastic modulus, strength, heat distortion temperature, and permeability [5].

Use of layered silicates in polymeric matrices was started early in 90s by introduction of PA/nanoclay [7]. Since then, many polymers have been examined in such composites. Among them, polypropylene has been considered significantly [12]. This is due to the high growth rate of this polymer, especially in autoindustry [12]. It is well known that in such a nonpolar resin, use of a kind of compatibilizer along with high shear stress is required to obtain a reasonable dispersion of clay platelets [13]. Please note that the nonpolar nature of polypropylene may even suppress intercalation of clay in the absence of compatibilizer [14]. In this case, nanocomposite will not form, and improved properties are not obtained. Many efforts have been conducted to improve dispersion of clay in polypropylene using functional oligomers as compatibilizer [14–22]. For this purpose, it is necessary to graft a polar compound such as maleic anhydride to the main chain of the nonpolar polymer. This creates a functional polymer which is miscible in the matrix, while it is compatible with clay as well. The effectiveness of PP-g-MA as compatibilizer in PP/clay system depends on its molecular weight and MA content which determines its functionality [20]. The effect of MA content on dispersion of clay in the matrix has been investigated notably, but the

results are to some extent contradictory [14–16, 18, 20–22]. The high amount of MA usually enhances the diffusion of polypropylene chains between the silicate layers, although it may lead to immiscibility of compatibilizer in the matrix, and thus, resulting in reduction of mechanical properties of the composite [14]. Reichert et al. [18], however, found that at a given clay loading, high MA content, that is, 4.2 wt.%, enhanced mechanical strength further than that of the low MA content, that is, 2.9 wt.%. Nevertheless, the influence of molecular weight of the compatibilizer is less obvious [20]. Most researchers have used low molecular weight PP oligomers for grafting to MA to improve the diffusion of chains into clay galleries [14–16, 18]. On the other hand, Wang et al. [21] illustrated that although low molecular weight (M_w = 9100 g/mol) oligomer resulted in better dispersion, high molecular weight (M_w = 330,000 g/mol) compatibilizer gave rise to better enhancement in mechanical properties. Kim et al. [22] incorporated four PP compatibilizers with different degrees of MA grafting and three PP matrices with low, medium, and high viscosity. They found that the system containing the low viscosity PP and the least MA content compatibilizer resulted in the greatest enhancement of dynamic storage modulus [22]. Therefore, it is claimed that without mentioning the molecular weight of compatibilizer, it is hard to judge the importance of the viscosity of individual components [22].

The role of processing conditions on properties of PP based nanocomposites is the subject of very few researches [20, 23–26]. Up to now, the literature contains no summary conclusions about the optimum processing conditions for obtaining desired properties of polymeric nanocomposites. Some works on the influence of processing conditions on the properties of the nanocomposites have been executed [23–26]. Dennis et al. [23] studied polyamide nanocomposite and showed that the surface chemistry of the clay platelets and the extent of shear stress determine the structure and, thus, the properties of the nanocomposite. Incarnato et al. [24] studied the effect of the extrusion rate on the properties of polyamide 6-based nanocomposites. Wang et al. [20] focused on the influence of the compatibilizer and melt mixing temperature on the dispersion of clay in polypropylene. They found that higher mixing temperature (160°C instead of 150°C) enhances diffusion of molecular chains into galleries but reduces shear viscosity. Therefore, low viscosity does not make enough shear for breaking up the platelets and leads to poor exfoliation morphology [20]. Modesti et al. [25] analyzed the effect of temperature profile and screw speed of extruder on the structure of nanocomposites. Their results showed that the applied shear stress is much more effective on the morphology (the extent of intercalation/exfoliation) than the residence time [25]. In addition, Lertwimolnun and Vergnes [26] characterized the role of mixing temperature, rotor speed, and mixing time in both internal mixer and extruder. They stated that increasing shear stress and mixing time and decreasing compounding temperature improve the extent of exfoliation [26].

In this research, PP-g-MA has been made using the same polymer used as the matrix. Influences of such a compatibilizer and processing conditions including rotor speed and feeder rate on morphology, mechanical properties, and deformation mechanism of polypropylene/clay nanocomposite have been investigated.

2. Experimental Method

2.1. Materials. A kind of isotactic polypropylene with the MFI (at 230°C, 2.16 kg) of 8 gr/10 min by the trade name of PI080 from Imam Khomeini Petrochemical Complex and an organophilic montmorillonite with the CEC of 110–120 meq/100 g by the trade name of NANOLIN DK4 from FCC were used. In order to synthesize compatibilizer, maleic anhydride (MA), and dicumyl peroxide (DCP), as initiator, both from Merck were incorporated.

2.2. Preparation of Nanocomposites. The processing conditions for preparing different nanocomposites made are summarized in Table 1. In order to make nanocomposite without compatibilizer, mixtures of 1.5, 3, and 5 wt.% nanoclay with polypropylene were blended in a corotating twin-screw extruder (L/D = 20) at a rotor speed of 50 and 100 rpm, while the temperatures in the successive zones were set at 140, 170, 180, and 190°C.

For preparing the compatibilizer, MA (2 phr) and DCP (0.1 phr) were dissolved in acetone and physically mixed with PP pellets at room temperature. After evaporation of acetone in air, MA and DCP precipitate on the pellets' surface homogeneously. As mentioned earlier, polypropylene used for making compatibilizer was the same polymer used as the matrix [23].

In the case of compatibilized nanocomposites, again, 1.5, 3, and 5 wt.% clay samples were made. The magnitude of compatibilizer in each case was equal to the clay loading. Temperature regimes in extrusion of compatibilized systems were similar to those of the noncompatibilized ones. Injection molding was utilized to make samples of the formulations made.

2.3. Characterization Techniques. Wide-angle X-ray diffraction (XRD) analyses were conducted using a Bruker Axs generator. An acceleration voltage of 40 kV and a current of 30 mA were applied using Cu-Kα radiation. Tensile tests were performed using a universal testing frame (Hounsfield H10KS) equipped with an extensometer, according to ASTM D638. Notched impact strengths were measured according to ASTM D256 using a 5 J impact hammer from Santam. The dimensions of Charpy samples were $25 \times 12.5 \times 3.5\,\text{mm}^3$. All mechanical tests were performed on average number of 5 specimens. Study of deformation behavior at the notch tip was done on thin samples cut from three-point-bending (3PB) specimens using a transmitted light optical microscope (OLYMPUS DL12). In order to do this experiment, notched Charpy samples were subjected to a certain amount of loading (215 N) in 3PB mode, in which a well-developed damage zone forms at the notch tip of samples. For observation of the deformation mechanism, the samples were cut and polished from both sides to reach the thickness of approximately less than 100 micrometers in the

Table 1: The compounds prepared in this study.

Compound	Processing conditions	
	Rotor speed (rpm)	Feeder speed (rpm)
(1) PP + Clay	50	10
(2) PP + Clay	100	10
(3) PP + PP-g-MA + Clay	50	10
(4) PP + PP-g-MA + Clay	100	10
(5) PP + PP-g-MA + Clay	100	15
(6) PP + PP-g-MA + Clay	150	15

Table 2: XRD results of organoclay and samples made (without compatibilizer).

Sample*	2θ (001)	d Spacing (Å) (001)
Organoclay	2.58	34.23
(1)	2.55	34.61
(2)	2.63	33.56

*The numbers in this column correspond to the compounds introduced in Table 1.

middle of the sample. This approach is further discussed in [27].

3. Results and Discussion

3.1. Characterization of the Structure. The results of XRD for organoclay and PP/5 wt.% clay nanocomposites with regards to different rotor speeds have been shown in Figure 1 and Table 2.

As can be seen in Table 2, incorporation of organoclay into polypropylene at the rotor speed of 50 rpm, that is, Sample (1) in Table 2, results in slight increased d-spacing of (001) planes. Table 2 also illustrates that the increase of rotor speed to 100 rpm, that is, Sample (2), will result in reduction of the d-spacing of the same planes. In order to explain this observation, one should consider the fact that the nanostructure in such a composite depends on both shear stress and the diffusion rate [23]. Please note that it is necessary to apply sufficient shear stress and allocate enough time to the polymer chains in order to be diffused into the galleries. At the rotor speed of 50 rpm, that is, Sample (1) in Table 2, it seems that the time for diffusion of the polymer chains into the galleries is sufficient. Thus, an increase in d-spacing is observed (Table 2). However, the value of d-spacing in Sample (1) is not large enough that might be as a result of the lack of compatibility between the polymer and the organoclay. This subject will be further examined later in this paper.

Sample (2) which corresponds to the rotor speed of 100 rpm illustrates reduction in d-spacing compared to that of Sample (1), that is, rotor speed of 50 rpm. This reduction in d-spacing of PP/clay nanocomposites during no incorporation of any compatibilizer was reported in literature before [14, 18, 20, 21]. The reason for this phenomenon

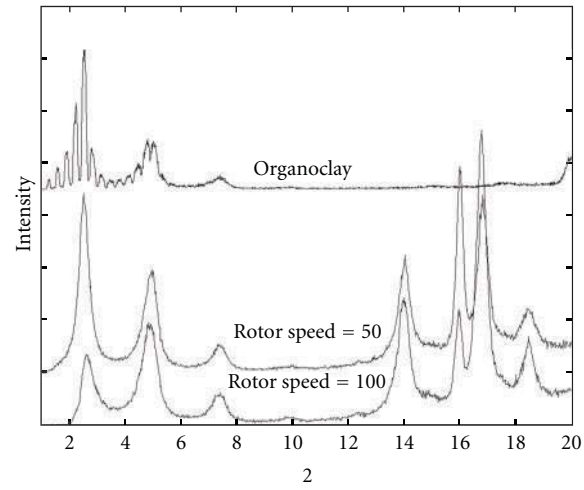

Figure 1: XRD graphs of organoclay and polypropylene based nanocomposites without compatibilizer compounded with Feeder Speed = 10 rpm.

has been attributed to the incompatibility of the polar hydroxyl groups on the surface of the clay platelets and the nonpolar polypropylene chains based on studies done in those researches [14, 18, 20, 21]. It seems that the incompatibility of clay and PP is not the only reason for decreasing the space between the layers. The slight increase of d-spacing in the condition of 50 rpm is an evidence for this claim. It is possible that the polypropylene chains stick to the surface modifier of clay (alkyl ammonium ions in this work), which is compatible with polymer during mixing. If the time for diffusing the polymer chains into layers is sufficient (Rotor Speed = 50 rpm), some of them may penetrate into layers (the d-spacing will increase). However, if there is no sufficient time for diffusing (Rotor Speed = 100 rpm), it seems that not only polymeric molecules are not able to penetrate into layers, but also they may pull out some surface modifier of clay during mixing (decreasing in d-spacing of layers will happen). Of course, it is worth mentioning that the sufficient time for diffusing the polymer chains into layers is different under conditions of with/without compatibilizer. Certainly, this argumentation is only a hypothesis. In other words, this matter is justified by several evidences, reasons, references, and so forth and it has been stated here only as a presumption.

The results of XRD relate to organoclay and PP/clay nanocomposites with compatibilizer in different rotor speeds, and feeder speeds have been shown in Figure 2 and Table 3.

A comparison of Tables 2 and 3 demonstrates the influence of compatibilizer on the structure of PP/clay nanocomposites, that is, increase in d-spacing when compatibilizer is incorporated. Figure 3 has been displayed for easier evaluating of the role of rotor speed played about the structure of compounds. As can be seen in Figure 3, the amounts of 2θ are changed to the right with the increased speed of the rotor of the extruder in the composite with compatibilizer (Sample (3), i.e., rotor speed of 50 rpm, and Sample (4), i.e., rotor

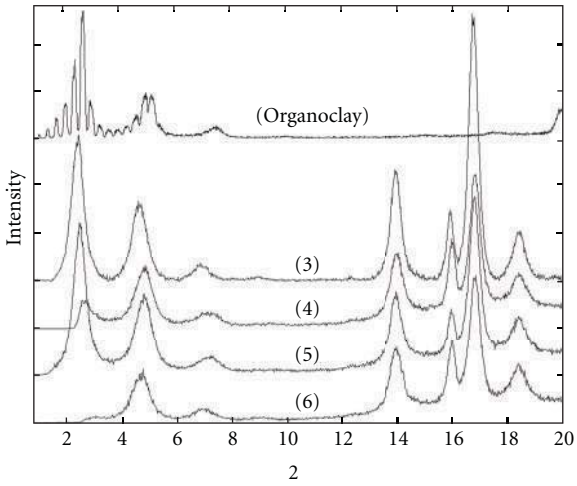

Figure 2: XRD graphs of organoclay and polypropylene based nanocomposites with compatibilizer. Numbers (3)–(6) correspond to the systems introduced in Table 1.

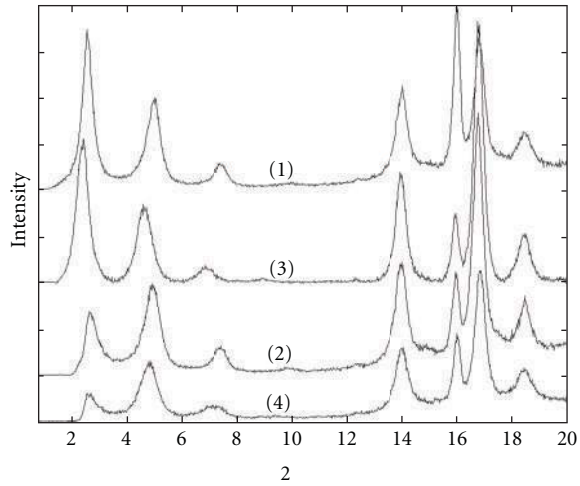

Figure 3: XRD graphs of compounds: (1)–(4).

Table 3: XRD results of organoclay and samples made (with compatibilizer) in different processing conditions as shown in Figure 2.

Sample	2θ (001)	d Spacing (Å) (001)
Organoclay	2.58	34.23
(3)	2.41	36.62
(4)	2.57	34.34
(5)	2.43	36.32
(6)	—	—

speed of 100 rpm) like without compatibilizer (Sample (1), i.e., rotor speed of 50 rpm, and Sample (2), i.e., rotor speed of 100 rpm). The change from 2θ peak to the right means that the intergallery spacing of layers has been decreased as shown in Tables 2 and 3 related to Samples (1) to (4). Also, as seen in Figure 3, the peak intensity at (001) planes has notably decreased under the condition of 100 rpm compared to 50 rpm in both conditions of incorporating compatibilizer (Sample (3), i.e., rotor speed of 50 rpm, and Sample (4), i.e., rotor speed of 100 rpm) and without compatibilizer (Sample (1), i.e., rotor speed of 50 rpm, and Sample (2), i.e., rotor speed of 100 rpm). Because the peak intensity at (001) planes is related to the number of layers in stacks of clay, these results demonstrate that the average number of platelets in stacks has decreased by increasing the shear stress on the system.

In addition, Table 3 illustrates that the space between layers has been increased by incorporating of compatibilizer in both conditions (rotor Speed of 50, i.e., Sample (3) and rotor speed of 100 rpm, i.e., Sample (4)). Of course, because of more residence time, increasing the d-spacing of clay in rotor speed of 50 rpm, that is, Sample (3), is more than 100 rpm, that is, Sample (4).

The effects of rotor speed and feeder speed on the dispersion of nanoclay in a polypropylene matrix have been investigated before by using an internal mixer and an extruder, respectively [26]. These researchers observed that the space between layers did not significantly depend on the shear rate or feeder speed [26]. On the contrary, they showed that the extent of exfoliation increased by the increase of the rotor speed of the internal mixer or with decreasing the feeder speed of the extruder [26]. The authors stated that increasing the feeder speed decreased the residence time. Therefore, it decreased the degree of exfoliation [26]. In the internal mixer, contrary to that of the extruder, the variation of rotor speed did not affect the residence time. Thus, this did not influence the d-spacing [26]. As can be seen in Figure 2, increasing the rotor speed in both conditions, 50 to 100 rpm, that is, Samples (3) and (4), and 100 to 150 rpm, that is, Samples (5) and (6) would result in reducing the peak intensity at (001) planes; that is, it increased the degree of exfoliation. This shows that under the conditions of this experiment, the shear rate is a more important factor regarding the degree of exfoliation than the residence time. Figure 2 and Table 3 reveal the influence of feeder rate on the structure of nanocomposite. As observed, with increasing the feeder rate from 10, that is, Sample (4) to 15, that is, Sample (5) the 2θ of the layers has decreased which is a symptom of increasing the d-spacing of (001) planes. At the same time, increasing the feeder rate has reduced the degree of exfoliation (has increased the peak intensity at (001) planes). Please note that with increasing the feeder rate at constant rotor speed, the intergallery spacing has been increased despite the reduction of the residence time. This means that as well as residence time, the effective L/D ratio has also been affected by the feeder rate in starve feeding [28]. It seems that increasing the feeder rate of extruder will increase the effective L/D ratio. Therefore, the forces, the velocity of conveyed material, and the amount of deformation will be changed [29].

On the other hand, the minimum strain (γ_0), the mean total strain ($\overline{\gamma}$) and the strain distribution function ($F(\gamma)$), and the terms of applied strain to the melt of polymer are proportional to L/H in mixing zone (H is the distance between cylinder and screw in extruder) [30]. It means

Table 4: Mechanical properties of PP/Clay samples in different conditions.

Sample	PP (wt%)	PPgMA (wt%)	Clay (wt%)	Rotor speed (rpm)	Feeder speed (rpm)	Elastic modulus (MPa)	Yield stress (MPa)	Impact strength (KJ/m^2)
	100	—	—	—	—	1588	28.7	2.2
(1)	98.5	—	1.5	50	10	1792	30.1	3.1
(1)	97	—	3	50	10	1891	30.0	3.6
(1)	95	—	5	50	10	1952	29.4	3.6
(2)	98.5	—	1.5	100	10	1711	29.3	2.9
(2)	97	—	3	100	10	1842	29.9	2.9
(2)	95	—	5	100	10	1871	29.2	3.5
(3)	97	1.5	1.5	50	10	1804	30.1	2.5
(3)	94	3	3	50	10	1929	30.2	3.3
(3)	90	5	5	50	10	2032	30.0	3.4
(4)	97	1.5	1.5	100	10	1787	30.2	2.8
(4)	94	3	3	100	10	1822	29.5	3.3
(4)	90	5	5	100	10	1918	28.9	3.3
(5)	90	5	5	100	15	1931	29.8	3.3
(6)	90	5	5	150	15	1961	30.1	3.0

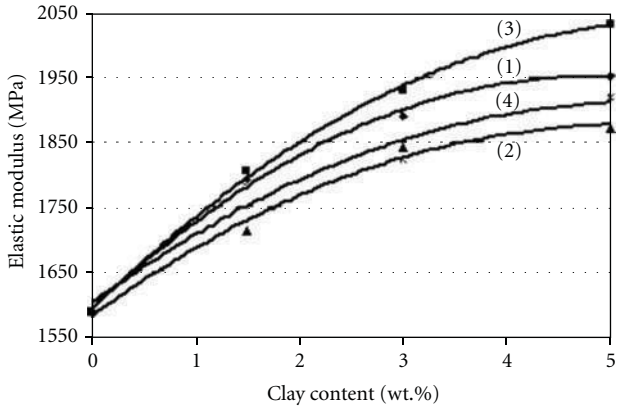

Figure 4: Variation of elastic modulus versus weight percentage of clay in the samples (1)–(4).

that with increasing L/H, the minimum and the mean total strains applied to the melt in the mixing zone increase. According to these explanations, the formation of the structure of nanocomposites in different feeder rates can be clarified (samples (4) and (5) in Figure 2 and Table 3). One may conclude that due to shorter mean residence time of material in the extruder, the peak intensity at (001) planes is enhanced, and due to higher minimum and mean total strains applied to the mixture, the d-spacing of the layers is increased, during the time of application of higher feeder rate, that is, increasing from 10 to 15 rpm.

3.2. Mechanical Properties. The results of the measurements of mechanical properties are illustrated in Table 4.

The effect of the compatibilizer and the rotor speed on the elastic modulus of PP/clay nanocomposites are illustrated in Figure 4.

As can be seen in Figure 4, the elastic modulus increases with decreasing the rotor speed, that is, Sample (1) compared with Sample (2), and the existence of compatibilizer, that is, Sample (4) compared with Sample (2) and Sample (3) compared with Sample (1). These observations can be explained by considering the structure of the samples (d-spacing of (001) layers). In Sample 2 (Figure 4 and Table 2) the amount of d-spacing reveals that molecular chains of PP have not been diffused into the clay galleries. Therefore, the system acts like conventional composites. In the case of using compatibilizer, that is, Sample (4), the d-spacing of layers have slightly increased in comparison with organoclay, and proportionally, the aspect ratio of the reinforcement has been increased. Therefore, it is probable that elastic modulus slightly increases under such a condition. This, together with possible stronger adhesion between clay and polymer due to incorporating compatibilizer can explain the higher modulus of Samples (1) and (3).

Based on these results, one may claim that there are two structural parameters which affect elastic modulus of nanocomposites: the d-spacing of layers (the aspect ratio of layers) and the number of layers in each stack (the aspect ratio of the stacks). Comparing the results of Samples (3) and (4) (Figures 3 and 4 and Table 3) assuming that the d-spacing of layers has a more effective role in modulus of elasticity. It means that Sample (3) has not only more d-spacing of layers, but also it has more number of layers in stacks than Sample (4) (elastic modulus of Sample (3) is more than of Sample (4)). The variations of yield stress and impact strength also depend on these structural parameters. It seems that the d-spacing of layers is more important factor on these properties (compare the result of Figure 3 and Tables 3 and 4). However, in order to understand the relationship between mechanical properties and morphology of samples, it is necessary to investigate the deformation mechanism in different samples. The following section has been allocated to this subject.

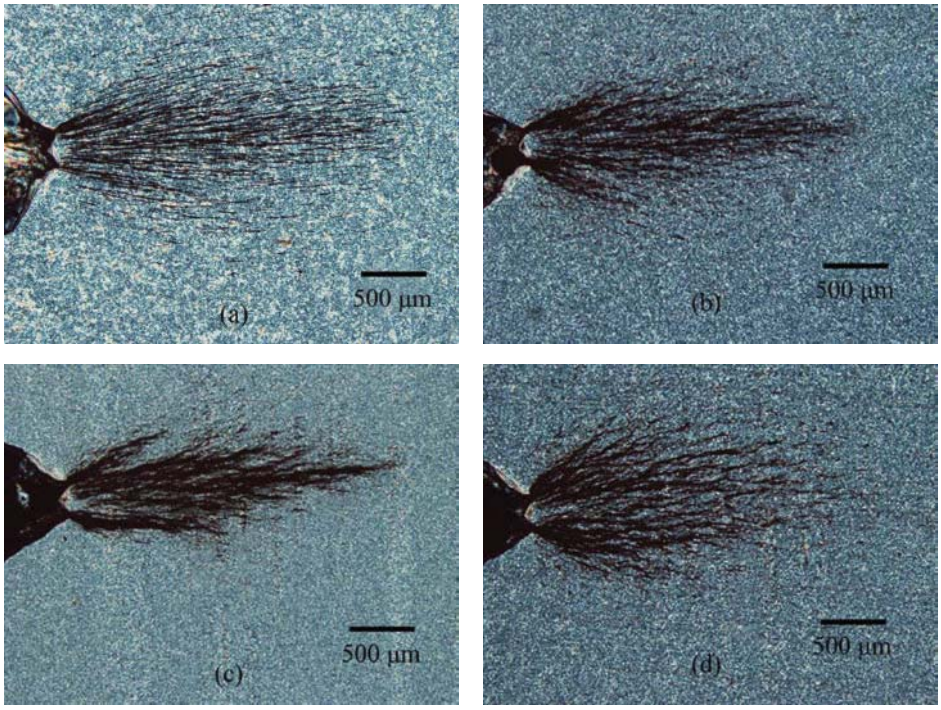

Figure 5: Transmission optical micrographs taken under cross-polarized light showing damage zones at the notch tip of PP/clay without compatibilizer, that is, Sample (2), subjected to $F = 215$ N: (a) neat, (b) 1.5 wt.% clay, (c) 3 wt.% clay, and (d) 5 wt.% clay.

3.3. Deformation Mechanism. The mechanisms of deformation at the notch tip of PP/clay composites without compatibilizer subjected to 3PB loading are illustrated in Figure 5.

These micrographs reveal crazing at the notch tips. Similar observation has been reported by Narisawa and Ishikawa [31] and Zebarjad et al. [32]. Figure 5(a) shows individual crazes formed and grown at the notch tip of polypropylene subjected to 3PB loading condition. Addition of organoclay (Figures 5(b)–5(d)) has intensified crazing at the notch tip so that more massive crazing has been observed in those figures. Intensification of crazing at the notch tip in the absence of compatibilizer was observed in our previous work by focusing on a Co-PP [33]. Despite the similar observations made for two studies, that is, intensification of crazing at the notch tip by incorporation of organoclay, there is a difference between the two studies. While the tensile yield stress was improved by adding organoclay in this study (Table 4), the previous work revealed reduction of yield stress by incorporation of silicate layers [33]. It seems that organoclays without compatibilizer tend to delaminate from the matrix while the tension stress is applied. This phenomenon makes the directions of stresses change from shear to normal by incorporating organoclays. As a result, the yield stress of homo-PP increases. In co-PP, some dilatational shear bands initiate and grow around the rubbery phase in the matrix. It is possible that these dilatational shear bands spread in the matrix when they encounter with organoclays which do not have good adhesion to matrix. As a result of this deformation distribution, the yield stress is reduced in co-PP.

In order to investigate the effect of compatibilizer on deformation mechanism, the notch tip of samples was examined (Figure 6).

As observed in Figure 6, incorporation of compatibilizer has reduced the extent of crazing very significantly. Comparing of XRD results (Tables 2 and 3) reveals that the d-spacing of layers increases by introducing the compatibilizer.

Figure 7 shows the notch tip deformation zones of PP/clay/PP-g-MA nanocomposites compounded with different feeder ratings from those of Figure 6.

As it was described earlier, the sample compounded at the feeder speed of 15 rpm (Figure 7(b)) has larger d-spacing and more numbers of silicate layers per stack in comparison with the other sample (Figure 7(a)). It means that this sample has limited amount of stacks per volume. Because the crazing mechanism tends to initiate and grow by incorporating organoclays (in the form of stacks), the deformation zone (crazing) at its notch tip will be smaller than the other sample under the condition of same loading (the suitable sites for initiation of crazing are less than the other sample).

4. Conclusion

Polypropylene/clay nanocomposites via melt intercalation in an intermeshing corotating twin-extruder using starve feeding system were prepared, and these results were obtained.

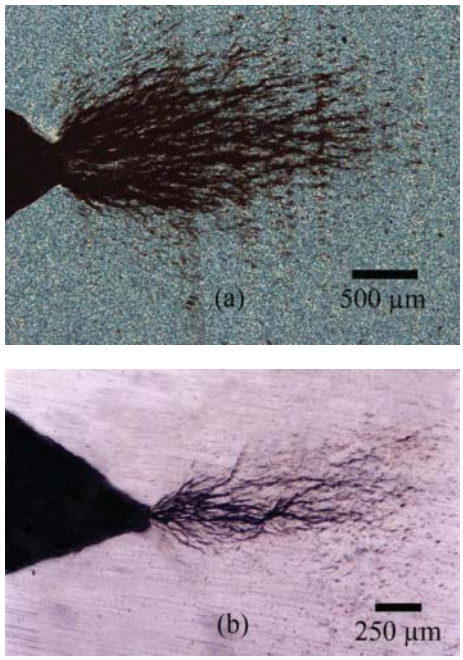

Figure 6: Transmission optical micrographs showing damage zones at the notch tip of (a) Sample (1) and (b) Sample (3) subjected to $F = 215$ N (samples include 5 wt.% organoclay and/or 5 wt.% PP-g-MA).

(i) The space between layers has been increased in existence of compatibilizer in both conditions (Rotor Speed = 50 and 100 rpm). Of course, due to more residence time, increasing the d-spacing of clay in rotor speed of 50 rpm is more than 100 rpm.

(ii) The shear rate is more important factor to extend exfoliation than the residence time in the conditions of this experiment.

(iii) With increasing the feeder speed of the extruder the intergallery space and the degree of exfoliation have increased and decreased, respectively.

(iv) The Young's modulus increases with decreasing the rotor speed and the existence of PP-g-MA as compatibilizer. It seems that the d-spacing of layers plays more effective role than the amount of layers in each stack, in modulus of elasticity.

(v) With adding the organoclay, the crazing mechanism has changed from local to massive in the mode of 3PB loading.

(vi) The deformation zone at the notch tip of samples decreases with increasing the feeder speed.

Acknowledgment

The authors thank Petrochemical Research and Technology Company (NPC-RT) for funding this research.

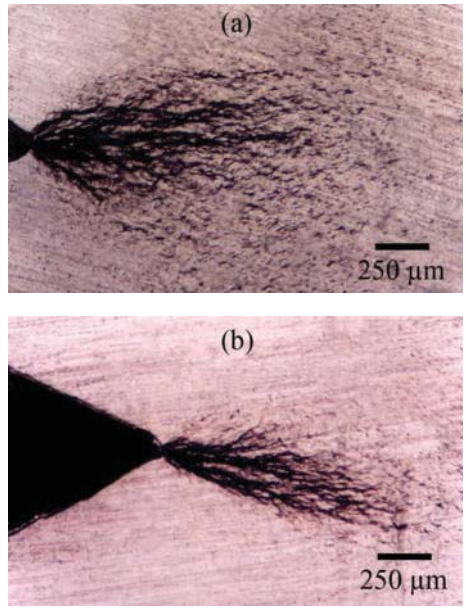

Figure 7: Transmission optical micrographs showing damage zones at the notch tip of PP/5 wt.% clay/5 wt.% PP-g-MA subjected to $F = 215$ N: (a) Sample (4), (b) Sample (5).

References

[1] C.-M. Chan, J. Wu, J.-X. Li, and Y.-K. Cheung, "Polypropylene/calcium carbonate nanocomposites," *Polymer*, vol. 43, no. 10, pp. 2981–2992, 2002.

[2] E. T. Thostenson, C. Li, and T.-W. Chou, "Nanocomposites in context," *Composites Science and Technology*, vol. 65, no. 3-4, pp. 491–516, 2005.

[3] J. Jordan, K. I. Jacob, R. Tannenbaum, M. A. Sharaf, and I. Jasiuk, "Experimental trends in polymer nanocomposites—a review," *Materials Science and Engineering A*, vol. 393, no. 1-2, pp. 1–11, 2005.

[4] Y. Rao and J. M. Pochan, "Mechanics of polymer-clay nanocomposites," *Macromolecules*, vol. 40, no. 2, pp. 290–296, 2007.

[5] S. S. Ray and M. Okamoto, "Polymer/layered silicate nanocomposites: a review from preparation to processing," *Progress in Polymer Science*, vol. 28, no. 11, pp. 1539–1641, 2003.

[6] S.-M. Lai, W.-C. Chen, and X.-S. Zhu, "Melt mixed compatibilized polypropylene/clay nanocomposites: part 1—the effect of compatibilizers on optical transmittance and mechanical properties," *Composites Part A*, vol. 40, no. 6-7, pp. 754–765, 2009.

[7] A. Okada and A. Usuki, "Twenty years of polymer-clay nanocomposites," *Macromolecular Materials and Engineering*, vol. 291, no. 12, pp. 1449–1567, 2006.

[8] L. Szazdi, A. Pozsgay, and B. Pukanszky, "Factors and processes influencing the reinforcing effect of layered silicates in polymer nanocomposites," *European Polymer Journal*, vol. 43, no. 2, pp. 345–359, 2007.

[9] R. Abu-Zurayk, E. Harkin-Jones, T. McNally, G. Menary, P. Martin, and C. Armstrong, "Biaxial deformation behavior and mechanical properties of a polypropylene/clay nanocomposite," *Composites Science and Technology*, vol. 69, no. 10, pp. 1644–1652, 2009.

[10] H. Palza, R. Vergara, M. Yazdani-Pedram, and R. Quijada, "Polypropylene/clay nanocomposites: effect of different clays and compatibilizers on their morphology," *Journal of Applied Polymer Science*, vol. 112, no. 3, pp. 1278–1286, 2009.

[11] L. Xu, H. Nakajima, E. Manias, and R. Krishnamoorti, "Tailored nanocomposites of polypropylene with layered silicates," *Macromolecules*, vol. 42, no. 11, pp. 3795–3803, 2009.

[12] E. Manias, A. Touny, L. Wu, K. Strawhecker, B. Lu, and T. C. Chung, "Polypropylene/montmorillonite nanocomposites. Review of the synthetic routes and materials properties," *Chemistry of Materials*, vol. 13, no. 10, pp. 3516–3523, 2001.

[13] Y. Kurokawa, H. Yasuda, M. Kashiwagi, and A. Oyo, "Structure and properties of a montmorillonite/polypropylene nanocomposite," *Journal of Materials Science Letters*, vol. 16, no. 20, pp. 1670–1672, 1997.

[14] M. Kawasumi, N. Hasegawa, M. Kato, A. Usuki, and A. Okada, "Preparation and mechanical properties of polypropylene-clay hybrids," *Macromolecules*, vol. 30, no. 20, pp. 6333–6338, 1997.

[15] M. Kato, A. Usuki, and A. Okada, "Synthesis of polypropylene oligomer-clay intercalation compounds," *Journal of Applied Polymer Science*, vol. 66, no. 9, pp. 1781–1785, 1997.

[16] N. Hasegawa, M. Kawasumi, M. Kato, A. Usuki, and A. Okada, "Preparation and mechanical properties of polypropylene-clay hybrids using a maleic anhydride-modified polypropylene oligomer," *Journal of Applied Polymer Science*, vol. 67, no. 1, pp. 87–92, 1998.

[17] A. Oya, Y. Kurokawa, and H. Yasuda, "Factors controlling mechanical properties of clay mineral/polypropylene nanocomposites," *Journal of Materials Science*, vol. 35, no. 5, pp. 1045–1050, 2000.

[18] P. Reichert, H. Nitz, S. Klinke, R. Brandsch, R. Thomann, and R. Mülhaupt, "Poly(propylene)/organoclay nanocomposite formation: influence of compatibilizer functionality and organoclay modification," *Macromolecular Materials and Engineering*, vol. 275, no. 1, pp. 8–17, 2000.

[19] H. Ishida, S. Campbell, and J. Blackwell, "General approach to nanocomposite preparation," *Chemistry of Materials*, vol. 12, no. 5, pp. 1260–1267, 2000.

[20] Y. Wang, F.-B. Chen, Y.-C. Li, and K.-C. Wu, "Melt processing of polypropylene/clay nanocomposites modified with maleated polypropylene compatibilizers," *Composites Part B*, vol. 35, no. 2, pp. 111–124, 2004.

[21] H. Wang, C. Zeng, P. Svoboda, and P. James Lee, "Preparation and properties of polypropylene nanocomposites," in *Proceedings of the 59th ANTEC Proceedings*, pp. 2203–2207, Dallas, Tex, USA, 2001.

[22] K.-N. Kim, H.-S Kimm, and J.-W Lee, "Effect of interlayer structure, matrix viscosity and composition of a functionaiized polymer on the phase structure of polypropylene-montmorillonite nanocomposites," *Polymer Engineering & Science*, vol. 41, no. 11, pp. 1963–1969, 2001.

[23] H. R. Dennis, D. L. Hunter, D. Chang et al., "Effect of melt processing conditions on the extent of exfoliation in organoclay-based nanocomposites," *Polymer*, vol. 42, no. 23, pp. 9513–9522, 2001.

[24] L. Incarnato, P. Scarfato, G. M. Russo, L. di Maio, P. Iannelli, and D. Acierno, "Preparation and characterization of new melt compounded copolyamide nanocomposites," *Polymer*, vol. 44, no. 16, pp. 4625–4634, 2003.

[25] M. Modesti, A. Lorenzetti, D. Bon, and S. Besco, "Effect of processing conditions on morphology and mechanical properties of compatibilized polypropylene nanocomposites," *Polymer*, vol. 46, no. 23, pp. 10237–10245, 2005.

[26] W. Lertwimolnun and B. Vergnes, "Influence of compatibilizer and processing conditions on the dispersion of nanoclay in a polypropylene matrix," *Polymer*, vol. 46, no. 10, pp. 3462–3471, 2005.

[27] R. J. Bagheri, "Rubber toughened epoxy: roles of particle cavitation and rubber/particle interface," Ph.D. thesis, Lehigh University, Bethlehem, PA, USA, 1995.

[28] C. Rauwendaal, *SPC: Statistical Process Control in Injection Molding and Extrusion*, Carl Hanser, Munich, Germany, 2000.

[29] Z. Tadmor and C. G. Gogos, *Principles of Polymer Processing*, John Wiley & Sons, 1979.

[30] D. G. Baird and D. I. Collias, *Polymer Processing: Principles and Design*, John Wiley & Sons, 1998.

[31] I. Narisawa and M. Ishikawa, "Crazing in semicrystalline thermoplastics," in *Crazing in Polymers (Advances in Polymer Science, Vols 91/92)*, H. Kausch, Ed., p. 353, Springer, Berlin, Germany, 1990.

[32] S. M. Zebarjad, R. J. Bagheri, A. Lazzeri, and S. Serajzadeh, "Fracture behaviour of isotactic polypropylene under static loading condition," *Materials and Design*, vol. 24, no. 2, pp. 105–109, 2003.

[33] B. Akbari and R. J. Bagheri, "Influence of PP-g-MA on morphology, mechanical properties and deformation mechanism of copolypropylene/clay nanocomposite," *Journal of Applied Polymer Science*, vol. 114, no. 6, pp. 3751–3759, 2009.

Hindawi Publishing Corporation
Journal of Nanomaterials
Volume 2012, Article ID 131672, 6 pages
doi:10.1155/2012/131672

Research Article

Nanostructured ZnO Arrays with Self-ZnO Layer Created Using Simple Electrostatic Layer-by-Layer Assembly

PilHo Huh[1] and Seong-Cheol Kim[2]

[1] *Samsung Electronics Co., Ltd., Solar Energy R&D Center, San #24 Nongseo-Dong, Giheung-Gu, Yongin-City, Gyeonggi-Do 446-711, Republic of Korea*
[2] *Department of Nano, Medical and Polymer Materials, Yeungnam University, 280 Daehak-Ro, Gyeongsan, Gyeongbuk 712-749, Republic of Korea*

Correspondence should be addressed to Seong-Cheol Kim, sckim07@ynu.ac.kr

Received 14 November 2011; Accepted 12 February 2012

Academic Editor: Alejandro Manzano Ramirez

Formation of unique ZnO nanoarrays utilizing photodynamic polymer, surface-relief grating structures, and unique electrostatic layer-by-layer assembly as a simple and economical methodology was demonstrated. Atomic force microscope (AFM), scanning electron microscopy (SEM), and energy-dispersive X-ray (EDAX) analysis were employed to characterize elemental composition and morphology of the resulting ZnO nanostructures with self-ZnO layer. Optical behavior of the final product was studied by UV-vis-NIR absorption and photoluminescence (PL) spectra.

1. Introduction

Since the large exciton binding energy of 60 mV and quantum confinement effects [1] of low-dimensional nanostructures, zinc oxide (ZnO) has become an attractive candidate for potential electronic, optoelectronic, electrochemical, and electromechanical devices, such as ultraviolet (UV) lasers, [2] light-emitting diodes (LED), [3] field emission devices, [4, 5] solar cells, [6] and piezo-nanogenerators [7, 8]. With changes in size and shape, unique electrical, mechanical, chemical, and optical properties may be freshly introduced, which are extensively believed to be the result of surface and quantum confinement effects [1]. To further improve its physical properties, substantial efforts have been devoted to develop various methodologies to create uniform and continuous one- (1D) or two-dimensional (2D) ZnO nanostructures. In an effort to integrate the resulting ZnO arrays into a more ordered fashion to enhance the performance of the nanodevices, a variety of techniques, including nanolithographic techniques (e.g., electron beam lithography, proximal probe patterning, and X-ray patterning) [9] and several chemical methods (e.g., vapor-solid, vapor-liquid-solid, and solution-solid) [10], have been employed. All these methods are not suitable for large fabrication process due to their exorbitant cost and complicated procedure. In contrast, an unconventional method used in this study may be much easier and economically more favorable, considering it can offer a much higher throughput in practice for solar energy conversion, light emission, and other promising areas. Periodic 1D and 2D ZnO nanostructures that were created simultaneously by self-assembly of the ZnO layers were prepared easily using the electrostatic layer-by-layer (ELbL) method by spin-coating, surface-relief grating (SRG) on the deposited photodynamic polymer film, and finally simple heat treatment. The alternating depositions of aqueous zinc acetate solution utilizing ELbL and polyanions assembly gave a good opportunity for facile fabrication of novel 1D and 2D ZnO nanostructures with self ZnO layer within a few hours.

2. Experimental Procedure

The indium doped tin oxide- (ITO-) coated glass and quartz substrates were used after cleaning by ultrasonication with isopropanol. A photodynamic polymer, poly orange 3 (PDO3), was synthesized from the diglycidyl ether of

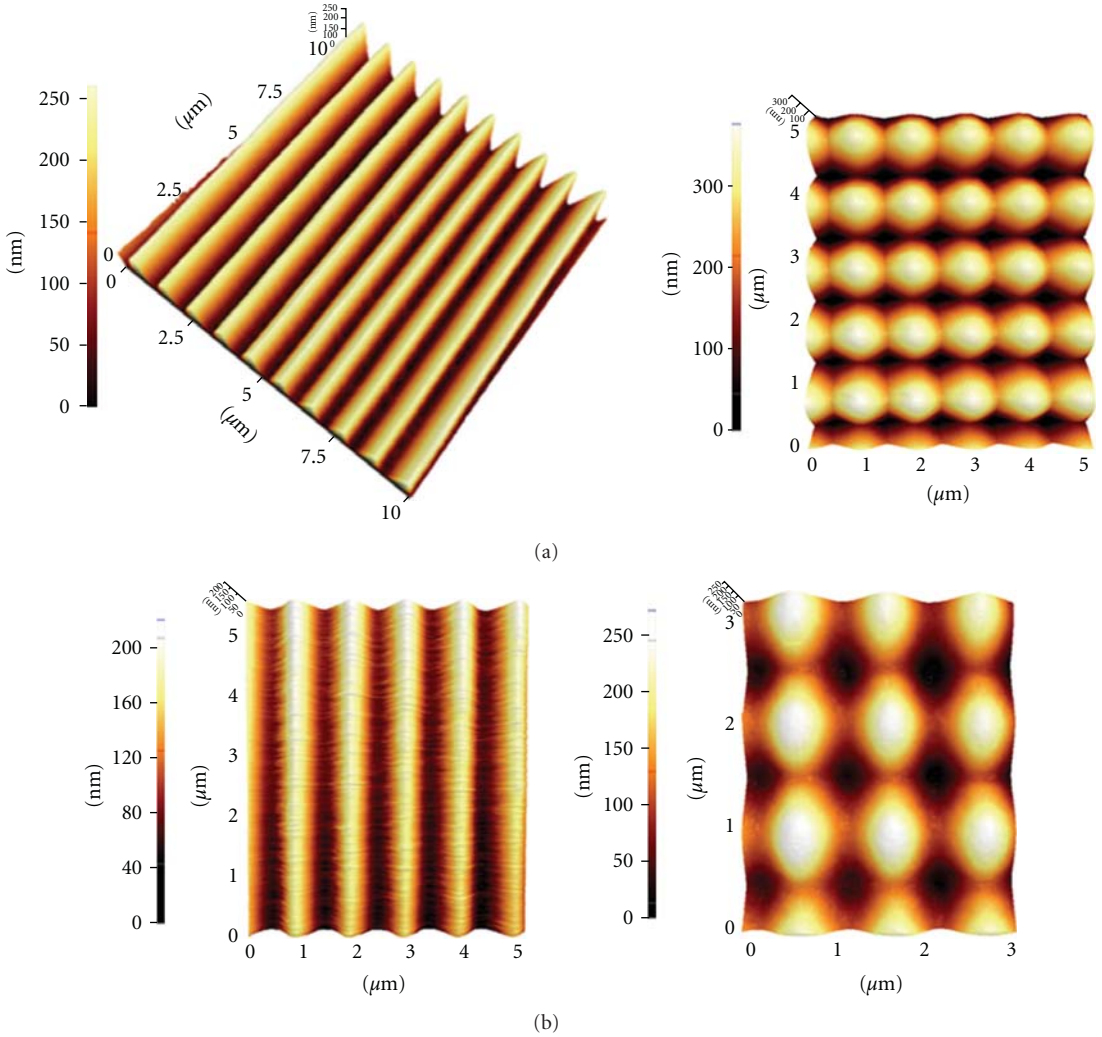

Figure 1: (a) 3D AFM views of submicrostructured 1D and 2D SRGs fabricated by exposing PDO3 to Ar^+ ion laser interference pattern and (b) 3D views of three bilayers of SPS/zinc acetate assembled in depressions on 1D and 2D SRG polymeric templates.

bisphenol A and disperse orange 3 as reported previously [11, 12]. 5 wt% PDO3 was dissolved in 1,4-dioxane and filtered through a 0.45 μm membrane to obtain a film with uniform thickness. The spin-coated PDO3 films on ITO substrates were then dried in a vacuum oven overnight at 60°C. 1D and 2D Surface-Relief Gratings (SRGs) were formed on the PDO3 films using an interference pattern of an argon ion^+ laser beam at 514.5 nm with an intensity of 100 mW/cm^2. 7 wt% of $Zn{\cdot}(CH_3COO)_2{\cdot}2H_2O$ purchased from Aldrich was stirred vigorously in 20 mL of H_2O for 2 hours to obtain the zinc acetate solution. The concentration of the used poly (4-styrene sulfonate) (SPS) solution was 0.1 wt% with pH 1.0 for all subsequent polyanion layers. In the assembly process, the SRG templates were quickly modified as sulfonyl groups by spin-coating the pH 1.0 SPS solution. 7 wt% zinc acetate solution was subsequently spin-coated on the SPS surface-modified SRGs. This completed one cycle. A deposition of one-bilayer assembly of the SPS/zinc acetate was progressed in short time without additional drying and rising steps. Thereafter, the process was repeated by alternating the deposition of pH 1.0 SPS solution and 7 wt% zinc acetate solution until the desired amount of zinc acetate was deposited in the assembly. Three bilayer assembly of the deposited SPS/zinc acetate was heat-treated at 500°C for 2 hours to burn off the polymeric template and to create well-defined ZnO nanostructures with self-ZnO layer. Scheme 1 illustrates the stepwise procedure used to prepare the nanostructured ZnO arrays with self-layer.

The samples were characterized by atomic force microscopy (AFM), scanning electron microscope (SEM), and an energy-dispersive X-ray (EDAX) analysis to study their morphologies and elemental compositions. The UV-vis-NIR spectrum was recorded at a scan rate of 240 nm/min. Photoluminescence (PL) spectrum was measured at the exciting wavelength of 345 nm.

3. Results/Discussion

Figure 1(a) shows 3D views of (a) 1D and 2D SRGs formed on the photodynamic polymer films. 1D and 2D SRGs were

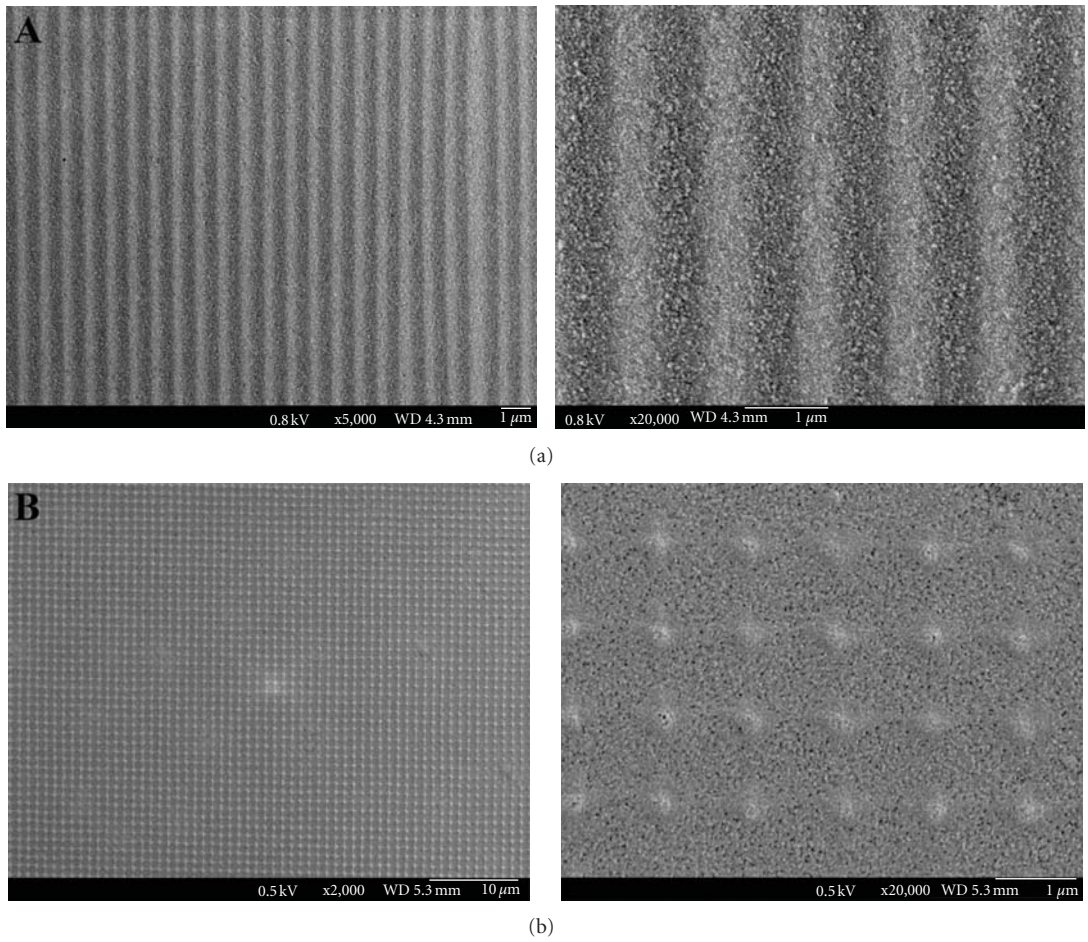

Figure 2: SEM views of nanostructured 1D (a) and 2D (b) ZnO arrays created on self-ZnO layer by simple electrostatic Layer-by-Layer spin-coating technique and pyrolyzing a three-bilayer assembly of SPS/zinc acetate on the individual 1D and 2D SRG templates.

used as polymeric templates to generate well-ordered ZnO nanostructures. The sinusoidally modulated gratings were used to fabricate a periodic array of 1D ZnO lines, while the egg-crate-like SRG structures were used to fabricate periodic arrays of 2D ZnO dots as shown in Figure 1(a). AFM height profiles of both SRG patterns showed an average modulation amplitude of about 210 and 200 nm, respectively. The periodicities of both gratings are approximately 1 μm. AFM images in Figure 1(b) show 3D views of an individual three-bilayer assembly of SPS/zinc acetate on both SRGs prepared using sequential ELbL by a spin-coating. The thickness of SPS/zinc acetate assembly can be controlled easily by adjusting rpm of spin-coater. Figure 1(b) indicated that the average thickness of SPS/zinc acetates ELbL on 1D SRG for a three-bilayer assembly was decreased by 10% to about 120 nm and that for 2D arrays was also reduced nearly by 40% to about 150 nm, respectively. Each cycle of a SPS/zinc acetate deposition by ELbL spin-coating was successively progressed for a three-bilayer assembly without additional washing and drying. Finally, a three-bilayer assembly of SPS/zinc acetate was dried at room temperature for an hour. Dried assembly was then heated for 2 hours through several steps (room temperature → 100°C → 300°C → 500°C) to remove the SRG polymeric template and to crystallize Zinc oxide.

Figure 2 summarizes typical SEM images of nanostructured 1D (a) and 2D (b) ZnO arrays created on ZnO self-layer on the ITO substrate. Well-ordered 1D and 2D ZnO arrays were formed as results of the sintering at 500°C for 2 hours in air condition as shown in Figure 2. The line and dot arrays created from collection of ZnO nanoparticles on self-layer show two distinctive shapes such as long sand ridges (a) and sand dunes (b) contrasted with various patterns fabricated by numerous techniques [13–17]. They also exhibit good uniformity and continuity within nanostructured patterns after sintering, although used SRG substrate is a microstructured polymeric template. Unique ZnO sand ridges and dunes created on self-ZnO layers may result from the difference of isoelectrical points between SPS polyelectrolyte and zinc acetate layer stacked alternatively. It is quite intriguing to note that zinc acetate layer was stacked selectively and quickly into grooves or hollows without buffer layer, SPS. However, when the buffer layer is present on top of hydrophobic SRG, ZnO-self layer appeared after the sintering process possibly due to adsorption of zinc acetate on the slope. The deposited SPS (or zinc acetate) to the SRG (or

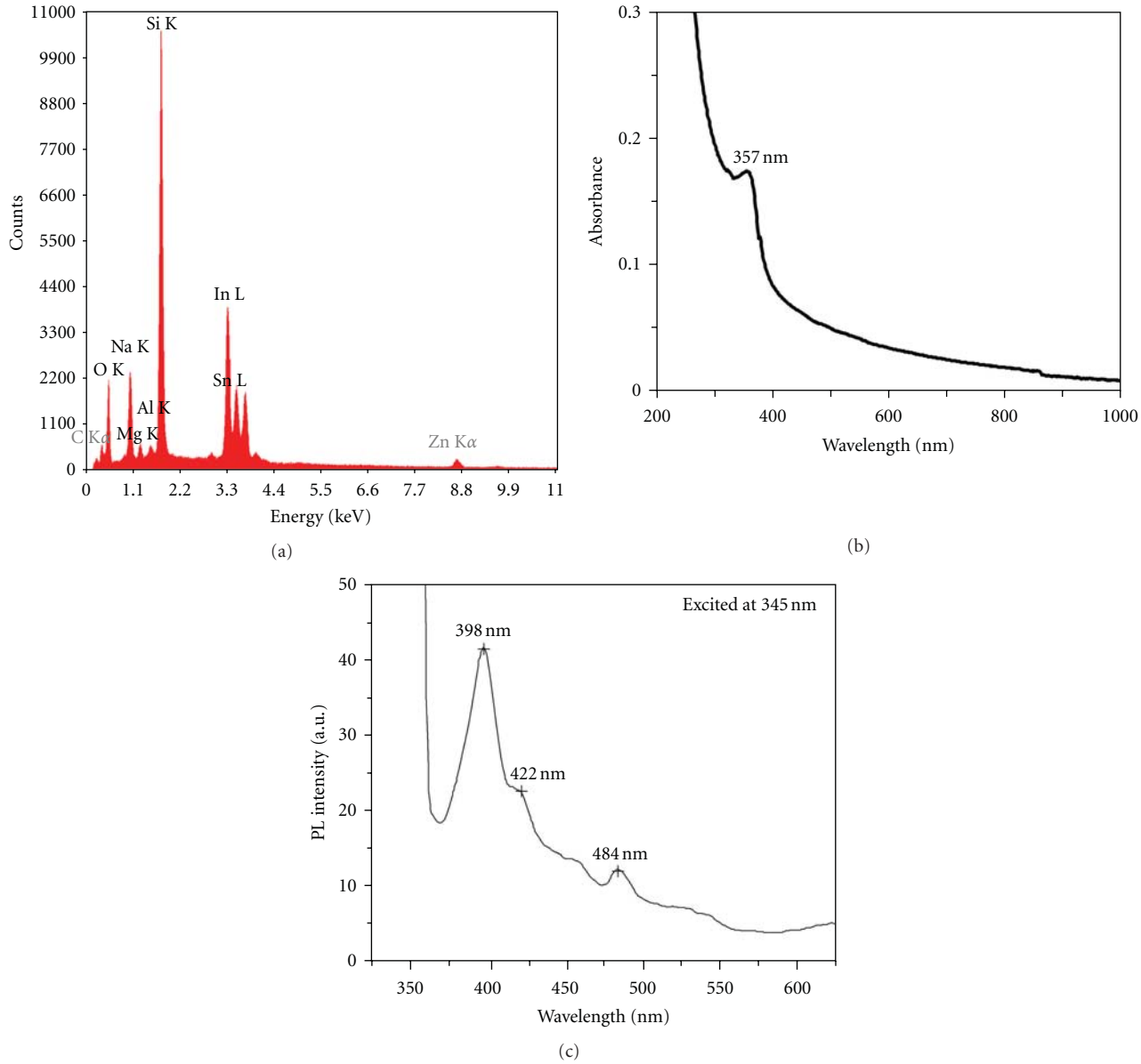

Figure 3: (a) The EDAX spectrum of the 2D ZnO nanostructures shown in Figure 2 for element analysis, (b) UV-vis-NIR and (c) photoluminescence (PL) spectra of nanostructured 2D ZnO arrays with self ZnO layer created on a quartz substrate; Exciting wavelength for PL is 345 nm.

SPS) may provide more adhesive strength for complexation (or charge interaction) with zinc acetate (or SPS) layer. The resulting ZnO nanostructures have innumerable porous structures over large area, which can provide a potential advantage for solar cell and sensor applications.

Elemental composition and crystalline structure of ZnO nanostructures well-patterned on self-layer were determined by energy-dispersive X-ray (EDAX) analysis and X-ray diffraction (XRD). The EDAX spectrum of the ZnO nanopatterns with self-layer in Figure 3(a) clearly shows the Zn Kα X-ray line at 8.65 keV and O Kα X-ray line at 0.52 keV. A very weak C Kα (0.282 keV) line compared with that of the non-heat-treated sample is obtained from EDAX spectrum. The crystallinity of the ZnO nanostructures was confirmed by X-ray diffraction (XRD). In the small sample quantity, three XRD patterns observed at around $2\theta = 31.80°$, $34.60°$, and $36.12°$ correspond well to the diffractions from the (100), (002), and (101) planes, respectively [18, 19]. The results from EDAX and XRD indicated that the produced patterns are composed of crystallized ZnO nanoparticles and that no significant traces of the SRG polymeric template remained after the sintering process. Other peaks revealed that the existence of Na, Mg, Si, Sn, and Al come from ITO substrate. UV-vis-NIR spectrum in Figure 3(b) shows the abrupt absorption band or edge characteristic of nanostructured ZnO arrays with self-ZnO layer centered at around 357 nm, which is in good corresponding with our previously work [17].

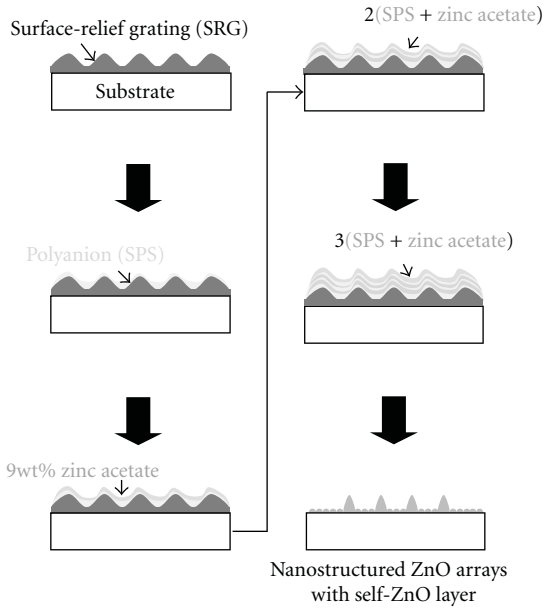

Scheme 1: Schematic procedure for creating nanostructured ZnO arrays with self-ZnO layer using electrostatic Layer-by-Layer Technique by spin-coating.

The photoluminescence (PL) spectrum of ZnO nanostructures after sintering at 500°C is shown in Figure 3(c). The three emission peaks at 398, 422, and 484 nm in wavelength were obtained from PL spectrum when excited at wavelength of 345 nm. The emission band occurred at around 398 nm can be assigned to the near band-edge transition, which is, namely, the recombination of free excitons through an exciton-exciton collision process, of wide band gap ZnO nanoparticles composed of the nanostructured ZnO arrays [20], while the two emission bands observed at around 422 and 484 nm result from the radial recombination of a photogenerated hole with an electron that belongs to a singly ionized oxygen vacancy [21] and the defect-induced emission from ZnO [22–24].

4. Conclusion

A simple, cost- and time-effective approach to create periodic nanostructured ZnO arrays onto self-layer over large areas has been described. The unconventional method was carried out using periodic microstructured polymeric templates, modified ELbL spin-coating technique, and heat-treatment. ZnO nanoarrays with self-layer are expected to have a wide range of applications such as sensors, energy storages, and solar cells. For instance, various fluorescence dyes may be incorporated in the functionalized ZnO surface, and ZnO nanoarrays with self-layer may be also used as a laser pumping due to its attractive optical property. This methodology can be readily applicable for creating nanopatterns with self-layer in other metal oxides, metals, or novel organic materials using common lithographic fabrication methods.

Acknowledgment

The authors acknowledge the financial support provided by Yeungnam University in the form of research grants in 2009.

References

[1] D. Bimberg, M. Grundmann, and N. Ledentsov, *Quantum Dot Heterostructures*, WILEY-VCH, Chichester, UK, 1998.

[2] M. H. Huang, S. Mao, H. Feick et al., "Room-temperature ultraviolet nanowire nanolasers," *Science*, vol. 292, no. 5523, pp. 1897–1899, 2001.

[3] X. W. Sun, J. Z. Huang, J. X. Wang, and Z. Xu, "A zno nanorod inorganic/organic heterostructure light-emitting diode emitting at 342 nm," *Nano Letters*, vol. 8, no. 4, pp. 1219–1223, 2008.

[4] X. Bai, E. G. Wang, P. Gao, and Z. L. Wang, "Measuring the work function at a nanobelt tip and at a nanoparticle surface," *Nano Letters*, vol. 3, no. 8, pp. 1147–1150, 2003.

[5] X. Wang, J. Zhou, C. Lao, J. Song, N. Xu, and Z. L. Wang, "In situ field emission of density-controlled ZnO nanowire arrays," *Advanced Materials*, vol. 19, no. 12, pp. 1627–1631, 2007.

[6] M. Law, L. E. Greene, J. C. Johnson, R. Saykally, and P. Yang, "Nanowire dye-sensitized solar cells," *Nature Materials*, vol. 4, no. 6, pp. 455–459, 2005.

[7] Z. L. Wang and J. Song, "Piezoelectric nanogenerators based on zinc oxide nanowire arrays," *Science*, vol. 312, no. 5771, pp. 243–246, 2006.

[8] X. Wang, J. Song, J. Liu, and L. W. Zhong, "Direct-current nanogenerator driven by ultrasonic waves," *Science*, vol. 316, no. 5821, pp. 102–105, 2007.

[9] R. D. Piner, J. Zhu, F. Xu, S. Hong, and C. A. Mirkin, "'Dip-pen' nanolithography," *Science*, vol. 283, no. 5402, pp. 661–663, 1999.

[10] X. Wang, C. J. Summers, and Z. L. Wang, "Large-scale hexagonal-patterned growth of aligned ZnO nanorods for nano-optoelectronics and nanosensor arrays," *Nano Letters*, vol. 4, no. 3, pp. 423–426, 2004.

[11] X. Wang, J. Kumar, S. K. Tripathy, L. Li, J. I. Chen, and S. Marturunkakul, "Epoxy-based nonlinear optical polymers from post azo coupling reaction," *Macromolecules*, vol. 30, no. 2, pp. 219–225, 1997.

[12] S. S. Kim, C. Chun, J. C. Hong, and D. Y. Kim, "Well-ordered TiO2 nanostructures fabricated using surface relief gratings on polymer films," *Journal of Materials Chemistry*, vol. 16, no. 4, pp. 370–375, 2006.

[13] S. K. Donthu, Z. Pan, G. S. Shekhawat, V. P. Dravid, B. Balakrisnan, and S. Tripathy, "Near-field scanning optical microscopy of ZnO nanopatterns fabricated by micromolding in capillaries," *Journal of Applied Physics*, vol. 98, no. 2, Article ID 024304, pp. 1–5, 2005.

[14] M. H. Huang, Y. Wu, H. Feick, N. Tran, E. Weber, and P. Yang, "Catalytic growth of zinc oxide nanowires by vapor transport," *Advanced Materials*, vol. 13, no. 2, pp. 113–116, 2001.

[15] Y. Dai, Y. Zhang, Q. K. Li, and C. W. Nan, "Synthesis and optical properties of tetrapod-like zinc oxide nanorods," *Chemical Physics Letters*, vol. 358, no. 1-2, pp. 83–86, 2002.

[16] J. Q. Hu and Y. Bando, "Growth and optical properties of single-crystal tubular ZnO whiskers," *Applied Physics Letters*, vol. 82, no. 9, pp. 1401–1403, 2003.

[17] P. Huh, F. Yan, A. Li et al., "Simple fabrication of zinc oxide nanostructures," *Journal of Materials Chemistry*, vol. 18, no. 6, pp. 637–639, 2008.

[18] G. Srinivasan and J. Kumar, "Optical and structural characterisation of zinc oxide thin films prepared by sol-gel process," *Crystal Research and Technology*, vol. 41, no. 9, pp. 893–896, 2006.

[19] A. Mitra and R. K. Thareja, "Photoluminescence and ultraviolet laser emission from nanocrystalline ZnO thin films," *Journal of Applied Physics*, vol. 89, no. 4, pp. 2025–2028, 2001.

[20] Y. C. Kong, D. P. Yu, B. Zhang, W. Fang, and S. Q. Feng, "Ultraviolet-emitting ZnO nanowires synthesized by a physical vapor deposition approach," *Applied Physics Letters*, vol. 78, no. 4, pp. 407–409, 2001.

[21] K. Vanheusden, W. L. Warren, C. H. Seager, D. R. Tallant, J. A. Voigt, and B. E. Gnade, "Mechanisms behind green photoluminescence in ZnO phosphor powders," *Journal of Applied Physics*, vol. 79, no. 10, pp. 7983–7990, 1996.

[22] T. Aoki, Y. Hatanaka, and D. C. Look, "ZnO diode fabricated by excimer-laser doping," *Applied Physics Letters*, vol. 76, no. 22, pp. 3257–3258, 2000.

[23] S. B. Zhang, S. H. Wei, and A. Zunger, "Intrinsic n-type versus p-type doping asymmetry and the defect physics of ZnO," *Physical Review B*, vol. 63, no. 7, Article ID 075205, 7 pages, 2001.

[24] S. Choopun, R. D. Vispute, W. Noch et al., "Oxygen pressure-tuned epitaxy and optoelectronic properties of laser-deposited ZnO films on sapphire," *Applied Physics Letters*, vol. 75, no. 25, pp. 3947–3949, 1999.